

AMANDA GEROTTO

**Carbonate system and elementary geochemistry:** Paleoceanographic and paleoclimatic implications in the South China Sea along the Late Quaternary

São Paulo

2022

AMANDA GEROTTO

**Carbonate system and elementary geochemistry:** Paleooceanographic and paleoclimatic implications in the South China Sea along the Late Quaternary

A thesis submitted to the Instituto Oceanográfico of the Universidade de São Paulo in partial fulfillment for the degree of Doctor of Science, Oceanography, with emphasis in Chemical Oceanography.

Advisor: Prof. Dr. Rubens Cesar Lopes  
Figueira

Co-advisor: Profa. Dra Renata Hanae Nagai

São Paulo

2022

GEROTTO, Amanda. **Carbonate system and elementary geochemistry:** Paleooceanographic and paleoclimatic implications in the South China Sea along the Late Quaternary. Doctoral dissertation presented as a requirement for the degree of Doctor of Science, Oceanography program, concentration area of Chemical Oceanography.

Evaluated on: \_\_/\_\_/\_\_\_\_

Committee in charge

Prof. Dr. \_\_\_\_\_ Institution\_\_\_\_\_

Chair

Signature\_\_\_\_\_

Prof. Dr. \_\_\_\_\_ Institution\_\_\_\_\_

Grade\_\_\_\_\_ Signature\_\_\_\_\_

Prof. Dr. \_\_\_\_\_ Institution\_\_\_\_\_

Grade\_\_\_\_\_ Signature\_\_\_\_\_

Prof. Dr. \_\_\_\_\_ Institution\_\_\_\_\_

Grade\_\_\_\_\_ Signature\_\_\_\_\_

Dedicated to the memory of my father  
Waldemar Gerotto and our memories on the  
way to USP since I was 7 years old.

## ACKNOWLEDGEMENTS

This journey was made thanks to the love of my family, especially my mother Maria Selma, my sister Aline and my aunt Rita. I admire you all and have you as inspiration for life. I am grateful to my father Waldemar Gerotto, who always encouraged me to enter the University of São Paulo but passed away at the beginning of this journey.

Prof. Dr. Rubens Cesar Lopes Figueira thank you for your guidance, example, and support throughout the doctorate. Prof. Dr. Renata Hanae Nagai for all the help, teaching, guidance, and academic inspiration. To my external co-advisor Iván Hernández-Almeida, thank you for the teaching and availability. I am thankful to my advisors for all the talks, for providing valuable feedback on my work, and for encouraging and inspiring me to become a scientist. I extend this thanks to the whole ETH Climate Geology group, especially Dr. Heather Stoll and Dr. Hongrui Zhang.

Thanks to colleagues at LaQImar and LabPaleo<sup>2</sup>, for the conversations that kept us connected and motivated. Marcela, Nancy, Ítalo, and Felipe, thank you for always being willing to have a good conversation and a cup of coffee.

Thanks to my flatmates from Zürich, Daria and Noemi, for welcome me in another country during the sandwich Ph.D. To Juan and all his crew who stayed with me at a delicate moment on my return to Brazil.

I attended singing classes at USP from 7 to 9 years old. Although I have followed other paths, my doctorate was also accompanied by a reconnection with music that was fundamental in my academic journey. I am thankful for all the friends that music has given me, especially in the last few years. Gabi for been by my side from playing sax and trumpet in São Paulo to a hike in Switzerland. Aline and Helô for the studies at Praça do Relógio, Irwin for the music and talks, and to everyone who was with me awakening my creative and scientific side at the same time in some way.

Funding was provided by Coordenação de Aperfeiçoamento de Pessoal de Nível Superior – Brasil (CAPES) - Finance Code 001 and CAPES-PRINT – Programa Institucional de Internacionalização - Process: 88887.571907/2020-00. This research used samples and data provided by the International Ocean Discovery Program (IODP), with support from IODP/CAPES-Brasil (Notice 38/2014) and FAPESP (Proc. n°2015/11832-2).

"Nothing in life is to be feared, it is only to be understood. Now is the time to understand more, so that we may fear less."  
Marie Curie (1867- 1934)

## RESUMO

GEROTTO, Amanda. **Sistema carbonato e geoquímica elementar: Implicações paleoceanográficas e paleoclimáticas no Mar Sul da China ao longo do Quaternário Superior.** 2022. 104 f. Tese (Doutorado) – Instituto Oceanográfico, Universidade de São Paulo, São Paulo, 2022.

Compreender as mudanças na química dos carbonatos dos oceanos é fundamental para elucidar o papel dos oceanos no ciclo global do carbono e no controle climático da Terra de acordo com sua grande capacidade de armazenamento de dióxido de carbono (CO<sub>2</sub>). O Mar Sul da China (*South China Sea* - SCS) é uma bacia tropical de grande interesse para a compreensão da evolução do sistema carbonato. Esta bacia marginal está sob influência da Monção do Leste Asiático (*East Asian Monsoon* - EAM) que tem um profundo impacto nas interações entre a atmosfera, continente e oceano. Neste contexto, o presente trabalho teve como objetivo avaliar as mudanças no sistema de carbono do SCS considerando os ciclos carbonáticos que atuaram na bacia controlando os processos de dissolução e diluição ao longo do Quaternário. Para isso, aplicamos uma abordagem *multiproxy* em amostras sedimentares marinhas de testemunhos recuperados nas sub-bacias leste, nordeste e norte do SCS - Holes IODP U1431D (4240 m de profundidade), U1432C (3829 m), e ODP 1146 (2092 m) - e em sedimentos superficiais coletados ao longo da bacia (R/V Sonne, SO-95) em profundidades entre 629-3809 m. Foram avaliados (i) os índices de abundância, fragmentação e dissolução de foraminíferos planctônicos e carbono orgânico total nos últimos 600 ka; (ii) o aporte terrígeno através da determinação de elementos maiores e traços nos sedimentos e variações na radiação natural gama; e (iii) realizada a calibração de atributos morfológicos de cocólitos em resposta a um experimento de dissolução em laboratório e à parâmetros ambientais oceânicos, gerando um novo *proxy* que foi aplicado na reconstrução de padrões de dissolução nos últimos 210 kyr. Os resultados mostraram que os registros localizados abaixo da lisoclina moderna e compensação de carbonatos estavam sob forte dissolução. Um aumento pontual na abundância de foraminíferos planctônicos foi relacionado à produtividade primária e à dinâmica da EAM, com a ocorrência de turbiditos influenciando na preservação de CaCO<sub>3</sub>. Apesar da baixa preservação de carbonato inerente à profundidade destes registros, houve maior diluição de sedimentos biogênicos pelo aporte terrígeno devido à contribuição mais significativa de sedimentos

potencialmente provenientes de Luzon em resposta à EAM de verão fortalecida. O experimento de dissolução e a avaliação dos sedimentos superficiais mostraram que as mudanças na morfologia dos cocólitos, obtidas pelo fator  $k_s$ , são controladas principalmente por mudanças na saturação de carbonato, e podem ser usadas como proxy para rastrear mudanças nos limites de saturação de carbonatos. Quando aplicado como proxy de dissolução, o fator  $k_s$  registrou mudanças possivelmente relacionadas a variações na profundidade da lisoclina nos últimos 210 kyr consistentes com mudanças na circulação de águas profundas entre o Pacífico e o SCS. Os resultados desta tese demonstram que os efeitos da dissolução pós-soterramento têm principal influência na composição das assembleias de micro e nanofósseis e na preservação de carbonato em sedimentos SCS e que o fator  $k_s$  dos cocólitos é um proxy confiável para rastrear mudanças na química do carbonato.

Palavras-chave: Mar Sul da China. Foraminíferos planctônicos. Aporte terrígeno. Cocólitos. Preservação do carbonato.



## ABSTRACT

GEROTTO, Amanda. **Carbonate system and elementary geochemistry: Paleooceanographic and paleoclimatic implications in the South China Sea along the Late Quaternary.** 2022. 104 f. Doctoral Dissertation – Oceanographic Institute of the University of São Paulo, São Paulo, 2022.

Understanding past ocean carbonate chemistry changes is critical to elucidate the role of the oceans in the global carbon cycle and Earth's climate control according to its large carbon dioxide (CO<sub>2</sub>) storage capacity. The South China Sea (SCS) is a tropical basin of great interest for understanding the evolution of the carbonate system. This marginal basin is under the influence of the East Asian Monsoon (EAM) which has a profound impact on the interactions between the atmosphere, land, and oceans. In this context, the present work aims to evaluate changes in SCS carbon system considering the carbonate cycles that acted in the basin along with the Quaternary controlling dissolution and dilution processes. For this, we applied using a multiproxy approach in marine sedimentary samples from cores recovered in the eastern, northeast, and northern sub-basins of the SCS - Hole IODP U1431D (4240 m depth), Hole U1432C (3829 m), and ODP 1146 (2092 m) - and in surface sediments collected along the basin (R/V Sonne, SO-95) at depths between 629-3809 m. We evaluated (i) the abundance, fragmentation, and dissolution indexes of planktonic foraminifera and total organic carbon in the last 600 ka; (ii) terrigenous input by the determination of major and trace elements in sediments and variations in natural gamma radiation; and (iii) performed the calibration of morphological attributes of coccoliths in response to a laboratory dissolution experiment and oceanic environmental parameters, generating a new proxy that was applied in the reconstruction of dissolution patterns in the last 210 kyr. The results showed that the records located below the modern lysocline and carbonate compensation were under strong dissolution. A punctual increase in planktonic foraminifera abundance was related to primary productivity and EAM dynamics, with the occurrence of turbidites influencing CaCO<sub>3</sub> preservation. Despite the low carbonate preservation inherent to the depth of these records, the dilution of biogenic sediments by the terrigenous input was recorded due to the more significant terrigenous contribution of sediments potentially sourced from Luzon in response to the strengthened summer EAM. The dissolution experiment and the evaluation of surface sediments showed that changes in coccolith morphology, obtained by the ks factor, are mainly controlled by changes in carbonate saturation, and can be

used as a proxy to track changes in carbonate saturation limits. When applied as dissolution proxy the  $k_s$  factor recorded changes possibly related to variations in lysocline depth over the last 210 kyr consistent with changes in deepwater circulation between the Pacific and the SCS. The results of this thesis demonstrate that post-burial dissolution has a major influence on the composition of micro and nannofossils assemblages and in the carbonate preservation at SCS sediments and that the coccolith  $k_s$  factor is a reliable proxy for tracking changes in carbonate chemistry.

**Keywords:** South China Sea. Planktonic foraminifera. Terrigenous supply. Coccoliths. Carbonate preservation.

## LIST OF FIGURES

- Figure 1.1 -. Map of the South China Sea showing (a) the Kuroshio Current (KC) and intrusion (purple dashed line) into the basin, bathymetry and the locations of Hole U1431D (this study) and the cores S049-14KL, S049-8KL, V36-3, V36-6 (Wang et al., 1995), 17957-2 (Li et al., 2001), 17962 (Xu et al., 2005), 17924 , ODP 1144 (Wang et al., 2016), ODP 1143 (Liu et al., 2008), MD97-2142 (Chen et al., 2003), MD05-2901, MD05-2904 (Su et al., 2013) and Hole U1433 (Zhou et al., 2019) cited and presented in the discussion; and the (b) calcium carbonate (CaCO<sub>3</sub> %) distribution in surface sediments (From Zhang et al., 2015). The figures were plotted with ODV software (Schlitzer, 2019).  
.....27
- Figure 1.2. Hole U1431D (a) vertical and linearized activity profile of excess <sup>230</sup>Th (in Bq kg<sup>-1</sup>) and (b) the age model based on the <sup>230</sup>Thx (ka) obtained.....32
- Figure 1.3. Hole U1431D a) planktonic foraminifer (PF) total abundance; b) total organic carbon (TOC); c) fragmentation (FI%) and d) foraminiferal dissolution (FDX) indexes values. During the period between 460 and 370 ka, there was no sedimentary recovery. Gray bars indicate glacial periods (Lisiecki; Raymo, 2005). .....34
- Figure 1.4. Planktonic foraminifera (PF) abundance per gram sediment from a) Hole U1431D (4240 m water depth, this study), b) Core SO49-14KL (3624 m water depth, Wang et al., 1995) and c) Core SO49-8KL (1040 m water depth, Wang; Wang, 1990) ; and total organic carbon (TOC) content in weight (%) from d) Hole U1431D (4240 m water depth, this study) and e) MD97-2142 (1557 m water depth; Chen et al., 2003). .....37
- Figure 1.5. Fragmentation index (FI%) from a) Hole U1431D (4240 m water depth, this study), b) Core 17957-2 (2195 m water depth, Li et al., 2001) and c) Core 17962 (1968 m water depth, Xu et al., 2005); and foraminiferal dissolution index (FDX) from d) Hole U1431D (this study), e) Core V36-3 (2809 m water depth, Wang et al., 1995) and f) Core V36-6 (1579 m water depth, Wang et al., 1995). .....39
- Figure 1.6. a) Planktonic foraminiferal total abundance and b) total organic carbon from Hole U1431D (this study) compared to paleoproductivity records based on *Florisphaera profunda*% from the c) Southern SCS (ODP 1143; Liu et al.,

2008), d) Northern SCS (MD05-2904; Su et al., 2013), e) Western SCS (MD05-2901; Su et al., 2013) and based on *Gephyrocapsa oceanica* from the f) Western SCS (MD05-2901; Li et al., 2015, supplementary material) and g) Stacked speleothem  $\delta^{18}\text{O}$  from Chinese Caves reflecting both summer (low  $\delta^{18}\text{O}$ ) and winter (high  $\delta^{18}\text{O}$ ) monsoon signals (Cheng et al., 2009). The FP% scales were reversed for comparison with primary productivity since it presents a negative relationship. ....42

Figure 2.1. The South China Sea and Hole U1432C (black dot) and ODP 1146 (unfilled dot) retrieval sites location. The arrows depict schematic Kuroshio Current intrusion (purple), modern SCS surface winter (blue), and summer (red) circulation (based on Liu et al., 2016). ....48

Figure 2.2. Hole U1432C (a) linearized and adjusted activity of excess  $^{230}\text{Th}$  ( $^{230}\text{Th}_{\text{xs}}$ , Bq  $\text{g}^{-1}$ ), and (b) age model based on  $^{230}\text{Th}_{\text{xs}}$  (ka) obtained. ....51

Figure 2.3. Proxies for terrestrial input (a, b, c), marine carbonate contribution (d, e), and chemical weathering intensity (f, g, h, i) were obtained from Hole U1432C and records from northeastern SCS sub-basin and China continental loess. (a) Natural gamma radiation values in counts  $\text{s}^{-1}$ , (b) Ti/Ca elemental ratio and (c) scores of principal component 1 (this study); (d) Planktonic foraminifera (PF) abundance from Hole U1432C (Nagai; Gerotto, 2019) and (e) scores of principal component 2 (this study); (f) Al/K elemental ratio and (g) scores of principal component 3 (this study); (h) ODP 1146 smectite/(illite+chlorite) ratio (Liu et al., 2003) and (i) Chinese Fed/Fet loess record (Guo et al., 2008). ....56

Figure 3.1. Map of the South China Sea and location of core-top samples (unfilled dots) and ODP1146 (red dot) used in the present study (A). Vertical profiles along N-S ( $5^\circ$  to  $22^\circ$  N) transect of (B) temperature, (C) salinity, (D) nitrate and (E) phosphate obtained from World Ocean Atlas 2001 (WOA01, Conkright et al., 2002), (F) total alkalinity (TALK) and (G) total dissolved inorganic  $\text{CO}_2$  from Goyet et al. (2000), (H) pH and (I)  $\Omega_{\text{Ca}}$  calculated at  $\text{CO}_2\text{SYS}$  (Pierrot et al., 2012) from previous extracted data (Goyet et al., 2000). ....66

Figure 3.2. Coccolith mean  $k_s$  variation in the dissolution experiment. (A) Box plots of coccoliths mean  $k_s$  under different volume of Calgon solution added and (B) histograms showing mean  $k_s$  frequency in each subsample. ....71

Figure 3.3. Coccolith preservation in subsamples treated with different volumes of Calgon solution. (A) Scatter plot of mean ks and $\sigma/\text{mean ks}$ and (B) linear correlation between mean ks and mean length. ....	71
Figure 3.4. Arithmetic means of the biological variables evaluated on the surface samples. The core-top sampling stations are distributed along the x axis according to the depth.....	72
Figure 3.5. Coccolith preservation in surface sediments (A) Scatter plot between mean ks and $\sigma/\text{mean ks}$ and (B) linear correlation between mean ks and mean length. ....	73
Figure 3.6. Redundancy analysis (RDA) ordinations for environmental variables and morphological measurements and calcite estimation of coccoliths. Sample depths are indicated by different colors. Squares correspond to samples from northern SCS, diamonds from central part, and triangles from southern SCS. ....	74
Figure 3.7. Linear correlation between $\Omega_{\text{Ca}}$ at bottom depths and mean ks from surface samples. ....	75
Figure 3.8. Downcore record of coccolith mean ks compared to carbonate system parameters and other proxies. (A) Coccolith mean ks obtained from ODP 1146 (2090 m water depth, this study); (B) Coccolith calcification index and weight from Noelaerhabdaceae ( $> 2 \mu\text{m}$ ) obtained from MD05-2904 (2066 m water depth, Su et al., 2020); (C) $\delta^{13}\text{C}$ from benthic foraminifera recorded at MD05-2904 (Wan et al., 2020); (D) B/Ca record from northern (MD05-2904, 2066 m water depth) and southern SCS (MD05-2896, 1657 m water depth); (E) Planktonic foraminifera fragmentation (%) from northern SCS (17957-2, 2195 m water depth, Li et al., 2001); and (F) Atmospheric $\text{CO}_2$ record (Lüthi et al., 2008). ....	81

## LIST OF TABLES

Table 1.1 - Planktonic foraminiferal species found in Hole U1431D and assigned a dissolution resistance group number ranked from the least to the most resistant group (Berger, 1975). .....	30
Table 1.2 - Hole U1431D Unit I lithology (Modified from Li et al., 2015a) and PF total abundance from core sections 3H to 1H. Low (L) = 10-32 specimens / at least 30% of samples; Common (C) = 32-100 specimens / at least 30% of samples; Frequent (F) = > 100 specimens / at least 30% of samples; Abundant (A) = > 300 specimens / at least 30% of samples. (*) Sections where samples with no-foraminifera are recorded. ....	31
Table 1.3. Biostratigraphy and paleomagnetic events of Hole U1431D (FAD = First appearance datum; LAD = Last appearance datum).....	32
Table 1.4. The location and data type of SCS marine records discussed here. ....	34
Table 2.1. Biomagnetostratigraphic events recorded in the U1432C core (Li et al., 2015c) were used to construct the final polynomial. T = top/last appearance datum; B= base/first appearance datum, and age-based on $^{230}\text{Th}_{\text{xs}}$ (ka).....	50
Table 2.2. Correlation matrix (Pearson coefficient) of the composition of the elements of Hole U1432C. Values in bold correspond to significant correlations. ....	52
Table 2.3. Variance and loadings of factors 1, 2, and 3 from the principal component analysis (correlation matrix) for the Hole U1432C element composition data. The scores above 0.3 are represented in bold. ....	52
Table 3.1. Station, coordinate data and water depth of core-top samples used in this study. ....	68
Table 3.2. Correlation matrix (p value and Pearson correlation) between biological and environmental variables.....	74

## LIST OF ABBREVIATIONS

ALK	Alkalinity
APC	Advanced Piston Corer
CCD	Carbonate Compensation Depth
CDW	Circumpolar Deep Water
DIC	Dissolved Inorganic Carbon
DWC	Deepwater Current
EAM	East Asian Monsoon
EASM	East Asian Summer Monsoon
EAWM	East Asian Winter Monsoon
FDX	Dissolution Index
FI%	Fragmentation Index
IODP	International Ocean Discovery Program
ITCZ	Intertropical Convergence Zone
KC	Kuroshio Current
MBDI	Mid-Brunhes Dissolution Interval
MBE	Mid-Brunhes Event
MIS	Marine Isotope Stages
NADW	North Atlantic Deep Water
NGR	Natural Gamma Radiation
NGRL	Natural Gamma Radiation Logger
NPDW	North Pacific Deep Water
PAR	Photosynthetic Active Radiation
PCA	Principal Component Analysis
pCO <sub>2</sub>	CO <sub>2</sub> Partial Pressure
PF	Planktonic Foraminifera
PP	Primary Productivity
RDA	Redundancy Analysis
SCS	South China Sea
SR	Sedimentation Rates
SST	Sea Surface Temperature
TALK	Total Alkalinity
TCO <sub>2</sub>	Total Carbon Dioxide
TOC	Total Organic Carbon

## TABLE OF CONTENTS

<b>1. INTRODUCTION</b> .....	18
<b>2. OBJECTIVES</b> .....	20
2.1 Main objective .....	20
2.2 Specific objectives .....	21
<b>CHAPTER I. Carbonate-rich sequences in the deep sea of the eastern South China Sea subbasin (IODP Hole U1431D) during the last 600 kyr</b> .....	22
<b>Abstract</b> .....	22
<b>1. Introduction</b> .....	23
<b>2. Regional setting</b> .....	25
<b>3. Material and methods</b> .....	27
3.1 Chronology .....	27
3.2 Total organic carbon .....	29
3.3 Planktonic foraminiferal analysis .....	29
3.3.1 Proxies for carbonate dissolution.....	29
<b>4. Results</b> .....	30
4.1 Core description and chronology.....	30
4.2 Total organic carbon.....	33
4.3 Planktonic foraminiferal assemblages .....	33
<b>5. Discussion</b> .....	34
5.1. Controlling factors of planktonic foraminifera abundances in deep-sea SCS sediments .....	35
5.2. Limitations of using planktonic foraminiferal dissolution indexes .....	38
5.3. Increased primary productivity or turbidity sequences? What controlled planktonic foraminifera preservation during MIS 8 and 7 in the SCS .....	40
<b>6. Conclusions</b> .....	43
<b>Acknowledgments</b> .....	43
<b>CHAPTER II. A deep-sea record of late Quaternary terrigenous input to the northeastern South China Sea (IODP Hole U1432C)</b> .....	44
<b>Abstract</b> .....	44
<b>1. Introduction</b> .....	45
<b>2. Study area</b> .....	46
<b>3. Data and methods</b> .....	47



3.1 Core and chronology.....	48
3.2 Natural Gamma Radiation (NGR).....	49
3.3 Major and trace elements composition .....	49
3.4 Data analysis.....	50
<b>4. Results</b> .....	50
4.1 Core description and chronology .....	50
4.2 Natural Gamma Radiation (NGR).....	51
4.3 Composition and distribution of major and trace elements.....	51
<b>5. Discussion</b> .....	53
5.1 Late Quaternary terrigenous input to the northeast SCS: controlling factors .....	54
5.2 SCS NE sub-basin potential sediment sources .....	57
5.3 What controlled late Quaternary biogenic particle preservation at the northeast SCS deep-sea? .....	58
<b>6. Conclusion</b> .....	60
<b>Acknowledgments</b> .....	61

**CHAPTER III. Dissolution effects on coccoliths morphology and its implications for paleoceanographic studies - a case study from the South China Sea .....**

<b>Abstract</b> .....	62
<b>1. Introduction</b> .....	62
<b>2. Oceanographic settings</b> .....	65
<b>3. Material and methods</b> .....	67
3.1 Dissolution experiment.....	67
3.2 Surface sample analyses .....	68
3.3 Statistical analysis.....	70
<b>4. Results</b> .....	70
4.1 Effects on coccoliths morphology in the dissolution experiment.....	70
4.2 Biological and environmental effects on surface samples calcite variation. ....	71
<b>5. Discussion</b> .....	75
5.1 Coccolith morphology under controlled dissolution conditions.....	75
5.2 Effects of dissolution on the morphology of coccoliths in surface sediments .....	77

5.3 Cocoliths morphological attributes as dissolution proxy: implications for SCS paleoceanography .....	78
<b>6. Conclusions</b> .....	82
<b>Acknowledgments</b> .....	82
<b>3. CONCLUSIONS</b> .....	83
<b>REFERENCES</b> .....	84
<b>APPENDICES</b> .....	100

## 1. INTRODUCTION

As a greenhouse gas, carbon dioxide (CO<sub>2</sub>) atmospheric concentration is one of the major drivers of Earth's climate changes (Lüthi et al., 2008; Yu et al., 2014). Due to its large CO<sub>2</sub> storage capacity, the ocean plays a critical role in climate regulation and in the global carbon cycle (Ridgwell; Zeebe, 2005; Yu et al., 2014; Sulpis et al., 2018). In the contemporary scenario of increasing anthropogenic CO<sub>2</sub> emissions (Hönisch et al., 2012; USGCRP, 2017), it is essential to understand how changes in oceanic physical and biogeochemical parameters control CO<sub>2</sub> fluxes. The elucidation of the role of the ocean in the global carbon cycle balance, may be achieved by looking into Earth's natural variability through the Quaternary Period (last 2.58 million years).

Air-sea CO<sub>2</sub> fluxes depend on CO<sub>2</sub> partial pressure (pCO<sub>2</sub>) and are regulated by sea surface hydrographic (i. e., temperature, salinity); dissolved inorganic carbon (DIC), that is, the concentrations of CO<sub>2</sub> (aq), bicarbonate (HCO<sub>3</sub><sup>-</sup>), and carbonate ions (CO<sub>3</sub><sup>2-</sup>); and alkalinity (ALK) conditions (Takahashi et al., 2002; Ridgwell; Zeebe, 2005; Yu et al., 2014). DIC and ALK are mainly controlled by biological activity such as calcification, respiration, and carbonate dissolution (Takahashi et al., 2002; Ridgwell; Zeebe, 2005; Zeebe, 2012; Sulpis et al., 2018). CaCO<sub>3</sub> biological production results in the consumption of seawater DIC and ALK removal (Sexton; Barker, 2012; Yu et al., 2014). While CaCO<sub>3</sub> dissolution, will result in ALK and DIC release to the ocean (Sexton; Barker, 2012). The [CO<sub>3</sub><sup>2-</sup>] has profound implications for this balance, as it determines seawater carbonate saturation and therefore CaCO<sub>3</sub> preservation and dissolution at the sea floor (Yu et al., 2014).

Calcareous micro and nanofossils, such as planktonic foraminifera and coccolithophorids, are abundant in marine sediments and widely applied in reconstructions that aim to understand the role of the oceans in the balance of the carbonate cycle. These organisms are responsible for about 32-80% of the carbonate flux, influencing the export of organic and inorganic carbon to the ocean floor (Young; Ziveri, 2000; Schiebel, 2002, Rost; Riebesell, 2004). Understanding the export of carbonate from ocean surface to deep waters promoted by the flux of calcifying marine organisms is considered key to biogeochemical cycles since their production and preservation are closely related to changes in the carbonate system (Beaufort et al., 2011; Bolton et al., 2016; González-Lemos et al., 2018).

The South China Sea (SCS, 0-25.5°N, 98.5-122.5°E) is one of the largest Pacific marginal basins and is of great interest for understanding the evolution of the biogeochemical cycles (Dai et al., 2013; Wan; Jian, 2014). This marginal basin is under the influence of the seasonal reversal of the East Asian Monsoon System (EAM) winds, one of the largest modern monsoon systems (McClymont et al., 2013; Yu; Chen, 2013). The EAM drives atmospheric and oceanographic processes at the SCS, which highlights the region as a central point for the understanding of atmosphere, land, and oceans dynamics, such as the carbon flow and the continental rainfall and drought by the riverine inputs (Dai et al, 2013; Wan; Jian, 2014).

During glacial and interglacial cycles of the Quaternary, CaCO<sub>3</sub> contents of SCS sediments are regulated by the effects of carbonate dilution by the terrigenous input ("Atlantic-type" cycle), and by dissolution ("Pacific-type" cycle) (Wang et al., 1986; Wang Et Al., 2005; Sexton; Barker, 2012). Above the lysocline<sup>1</sup>, SCS sedimentary CaCO<sub>3</sub> content reflect the "Atlantic type" cycle, reflecting higher (smaller) presence during the interglacial (glacial) periods and a shallower (deeper) Carbonate Compensation Depth<sup>2</sup> (CCD) (Wang et al., 2005; Sexton; Barker, 2012). While below the lysocline, the SCS carbonate records show variations associated with the "Pacific type" cycle, with higher (smaller) preservation during glacial (interglacial) periods corresponding to a deeper (shallower) CCD position (Wang et al., 1986; Archer et al., 1996; Sexton; Barker, 2012). Given the complexity of the carbonate system, which involves physiological and ecological factors during calcifying organisms' life cycle, post-depositional changes, and regional hydrographic effects; the factors that drive SCS carbonate records preservation are still debated (Jin et al., 2019; Su et al., 2020; Balestrieri et al., 2021). The hypothesis of this study is that the evolution of carbonate saturation limits along the Quaternary influenced the composition and morphology of fossil assemblages of foraminifera and coccolithophorids at different depths of the SCS. This hypothesis considers the evaluation of carbonate preservation in sediments collected above and below the lysocline under the influence of different carbonate cycles in the SCS, driven by the processes of dilution (terrigenous input) and dissolution, respectively.

<sup>1</sup>Lysocline is the depth in the ocean to which CaCO<sub>3</sub> dissolution becomes prominent (Berger, 1968).

<sup>2</sup>Carbonate Compensation Depth is the depth that limits the presence of CaCO<sub>3</sub> due to rapidly increased dissolution (Berger, 1968).

In this sense, the main objective of this work is to evaluate SCS carbonate chemistry evolution along the Quaternary by applying a multiproxy approach to a set of sedimentary records retrieved at different depths of this marginal basin. In chapter, “*Carbonate-rich sequences in the deep sea of the eastern South China Sea subbasin (IODP Hole U1431D) during the last 600 kyr*” the relationship between paleoceanographic changes and  $\text{CaCO}_3$  production and dissolution limits (lysocline and CCD depths) in the last 600 kyr, based on planktonic foraminifera abundances and fragmentation and dissolution indices, and total organic carbon (TOC) from a core collected below the modern CCD (IODP Hole U1431D, 15°22'N, 117°00'E, 4240 m water depth). In chapter 2, “*A deep-sea record of late Quaternary terrigenous input to the northeastern South China Sea (IODP Hole U1432C)*”, aims to evaluate the influence of terrigenous input and the EAM on the dilution of biogenic particles in deep SCS sediments from northeast sub-basin, through sediments major and trace elements contents and natural gamma radiation. Finally, chapter 3 “*Coccoliths morphological attributes from surface sediments and Late Quaternary carbonate chemistry variations in SCS*”, a new proxy was calibrated from the morphological attributes of coccoliths of the Noelaerhabdaceae family evaluated in an acidification experiment and on surface samples collected on the R/V Sonne (SO-95) expedition along with the SCS at different depths and their responses to different environmental variables from a redundancy analysis (RDA). Based on the results of this calibration, the ks shape factor of the coccoliths was applied as a proxy for dissolution changes in the last 210 kyr in a sedimentary record from northern SCS (ODP 1146, 19°27' N, 116°16' E, 2092 m of water depth).

This thesis provides novel information on the evolution of the SCS Quaternary carbonate chemistry changes above and below the lysocline, highlighting the role of deep-water circulation and post-burial processes in the carbonate record preservation. These results provide a better understanding on the application of micro and nannofossils as proxies for environmental changes and seawater carbonate parameters in the past.

## **2. OBJECTIVES**

### **2.1 Main objective**

The present work aims to investigate changes in SCS carbonate chemistry based on the  $\text{CaCO}_3$  record preservation, dissolution, and dilution over Quaternary glacial-

interglacial cycles through a multiproxy approach. The results obtained are presented in three chapters as manuscripts corresponding to the specific objectives described below.

## 2.2 Specific objectives

(a) To evaluate the  $\text{CaCO}_3$  preservation in the last 600 kyr in sediments collected below the lysocline and CCD limits.

(b) To evaluate terrigenous input and its role in the dilution of biogenic sediments in the last 230 kyr in deep-sea sediments of the SCS northeast sub-basin.

(c) To provide a new proxy for  $\text{CaCO}_3$  dissolution based on the morphological attributes of coccoliths and evaluate its application in understanding SCS carbonate chemistry evolution along the Quaternary.

## CHAPTER I

### **Carbonate-rich sequences in the deep sea of the eastern South China Sea subbasin (IODP Hole U1431D) during the last 600 kyr**

Manuscript published in May 2020, in the *Marine Micropaleontology*. This manuscript is co-authored by Rubens Cesar Lopes Figueira, Paulo Alves de Lima Ferreira, Annette Hahn, Iván Hernandez-Almeida, and Renata Hanae Nagai

DOI: 10.1016/j.marmicro.2020.101879

#### **Abstract**

Here, we examined changes in carbonate preservation in a deep-sea record (Hole U1431D, 4240 m water depth) retrieved from the South China Sea (SCS) during the International Ocean Discovery Program (IODP) Expedition 349. To evaluate these changes, we applied a micropaleontological and geochemical multiproxy approach including, planktonic foraminifera (PF) total abundance, fragmentation (FI%) and dissolution (FDX) indexes, and total organic carbon (TOC). The results of this study showed that during the last 600 kyr, Hole U1431D site has been under the effect of carbonate dissolution associated with the deepening of the lysocline and the Calcite Compensation Depth. Nonetheless, during MIS 8 and MIS 7, there was a significant increase in PF total abundance and TOC content. The low PF total abundance found in some intervals resulted in an underestimation of the FI% and FDX indexes. Although high PF total abundance events occur at Hole U1431D turbidite sequences, these are also interpreted in the context of higher primary productivity (PP) in the central SCS. High TOC contents from MIS 10 to MIS 6 were associated with the effects of enhanced PP during the Mid-Brunhes Dissolution Interval as well as the dynamics of the East Asian Monsoon (EAM). During MIS 8 and 7, increased abundances of PF and TOC contents may have been related to enhanced PP promoted by the seasonal EAM. Our data suggest that enhanced PP associated with the occurrence of turbidite currents at the East SCS subbasin allowed the preservation of PF at Hole U1431D.

**Keywords:** IODP Hole U1431D; Late Quaternary; Planktonic foraminifera; Total organic carbon; Turbidite; East Asian Monsoon.

## 1. Introduction

The role of the deep ocean in the carbon cycle has been widely explored due to their large capacity to store carbon dioxide ( $\text{CO}_2$ ), which is approximately 50 times larger than the capacity of the atmosphere (Falkowski et al., 2000; Wang et al., 2003; Wang et al., 2016; Sun et al., 2017; Kerr et al., 2017; Ma et al., 2018). As  $\text{CO}_2$  flows through the ocean-atmosphere interface, it influences the chemical balance of water by affecting the dissolved inorganic carbon (DIC) and alkalinity (ALK) (Ridgwell; Zeebe, 2005). This flow implies that concentration changes in  $\text{CO}_{2(\text{aq})}$ , bicarbonate ( $\text{HCO}_3^-$ ) and carbonate ions ( $\text{CO}_3^{2-}$ ) play a key role in atmospheric  $\text{CO}_2$  regulation (Ridgwell; Zeebe, 2005; Wang et al., 2016). Calcium carbonate ( $\text{CaCO}_3$ ) production and preservation in marine sediments have a great influence on this balance (Ridgwell; Zeebe, 2005; Wang et al., 2016). The supply of  $\text{CaCO}_3$  to deep-sea sediments comes from biological production in a process that results in the consumption of seawater DIC and ALK removal from deep water (Sexton; Barker, 2012; Yu et al., 2014). As  $\text{CaCO}_3$  dissolves, the ALK returns to the ocean (Sexton; Barker, 2012).

Planktonic foraminifera (PF) are one of the major contributors to the calcite flux in global surface sediments, contributing to approximately 32–80% of the total deep-marine calcite budget (Schiebel, 2002). The seasonality of the PF shell flux is reported to be strongly related to primary productivity (PP) cycles, according to ecological preferences of species (Kucera, 2007; Jonkers; Kucera, 2015; Salmon et al., 2015). Nevertheless, for deep waters (below 2000 m), the role of PP has been discussed as a secondary factor controlling the  $\text{CaCO}_3$  flux when compared to carbonate dissolution effects (Bordiga et al., 2013; Sun et al., 2017).

The  $\text{CaCO}_3$  content of modern marine sediments assemblage presents a vertical gradient of dissolution that increases according to depth in response to seawater carbonate saturation (Berger, 1970). The lysocline is defined as the depth up to which  $\text{CaCO}_3$  is subjected to prominent (visually) dissolution effects, while the Calcite Compensation Depth (CCD) limits the presence of  $\text{CaCO}_3$  (Berger, 1968). According to Berger (1968), the depth of the lysocline determines the limit between well (up to lysocline) and poorly preserved PF in response to dissolution effects. Below this depth, the PF content in sediments is residual or, if present, poorly preserved (Berger, 1968). Meanwhile, sedimentation below the CCD can result in completely absent of  $\text{CaCO}_3$  (Ridgwell; Zeebe, 2005; Sexton; Barker, 2012). Thus, the PF total abundance in deep-sea sediments



constitutes a good proxy to infer past lysocline and CCD positions, that must be evaluated for each region, as this abundance can be affected by other environmental processes, such as dilution or productivity (Wang et al., 1986; 1995; Wei et al., 1998; Schiebel et al., 2002; Morey et al., 2005; Wang et al., 2016; Ma et al., 2018). Therefore, although palaeoceanographic reconstructions based on PF are indicated as proxies to assess carbonate preservation and dissolution effects, it is recommended that these reconstructions apply a multiproxy approach.

The evolution of calcium carbonate dissolution in the Quaternary South China Sea (SCS) has been explored in recent decades due to the great potential of this method to provide geological data for the comprehension of palaeoceanographic changes (Wang et al., 1995; Li et al., 2001; Xu et al., 2005; Huang et al., 2015 and references in; Wang et al., 2014; Wang et al., 2016; Luo et al., 2018). This semi-enclosed basin is characterized by high sedimentation rates (*i.e.*, 2.5-10 cm/ka) and good carbonate preservation (Wang et al., 1995; Wang et al., 2014). The variations recorded in the SCS for the Late Quaternary depict a complex scenario of calcium carbonate dissolution in the intermediate and deep water that is mainly associated with water chemistry and biological productivity (Wang et al., 1995; Li et al., 2001; Xu et al., 2005; Huang et al., 2015 and references in; Wang et al., 2016; Luo et al., 2018). As a semi-enclosed marginal basin, the SCS deep-water chemical characteristics are dominated by the conditions in adjacent open oceans, such as the effects of CCD variations in western Pacific deep waters (Miao; Thunell, 1994; Wang et al., 1995; Chen et al., 2001; Broecker, 2008; Sexton; Baker, 2012).

The periodic fluctuation of the CCD during the Quaternary characterizes the pattern of carbonate dissolution in deep-sea sediments. Calcium carbonate records from the Atlantic and Pacific reflect changes in the position of the CCD as well as opposing trends in dissolution patterns during the Quaternary (Wang et al., 1986, Sexton; Barker, 2012). A shallower CCD characterizes the Atlantic-type during glacial periods strengthening the dissolution effects and resulting in lesser carbonate content; the opposite is observed during interglacial with a deeper CCD (Wang et al., 1986). While the Pacific-type corresponds to a deeper (shallower) CCD position during glacial (interglacial) stages, reflecting an increase (decrease) in the carbonate content (Wang et al., 1986; Sexton; Baker, 2012). These shifts in the CCD position are mainly associated with the seawater DIC and ALK contents and the age of the water mass present in the

basin (Wang et al., 1986; Sexton; Barker, 2012; Kawahata et al., 2019). For example, the Circumpolar Deep Water (CDW) is older and, therefore high performed nutrient concentrations that youngest North Atlantic Deep Water (NADW), which means more corrosiveness water bathing Pacific than the Atlantic Ocean (Kawahata et al., 2019). However, strengthening of CDW ventilation in the Southern Pacific lead to better  $\text{CaCO}_3$  preservation during Quaternary glacial cycles, while well-ventilated NADW and hence, better carbonate preservation, prevailing during interglacial in the Atlantic (Kawahata et al., 2019).

In the SCS, both carbonate cycles are reported, as the high terrigenous supply diluted the carbonate content above the modern lysocline during glacial stages (shallower CCD), it reflects the Atlantic-type (Wang et al., 1995; Chen et al., 2011). On the other hand, below the modern lysocline, dissolution effects predominate over dilution effects with decreased carbonate content during interglacial stages reflecting the Pacific-type (Wang et al., 1995; Chen et al., 2011). Although both types of carbonate cycles being observed at SCS, the CCD dynamic is expected to reflect the Pacific pattern due to the large influence of its carbonate chemistry in this marginal basin (Dai et al., 2013). Nonetheless, Luo et al. (2018) suggested a possible independent dynamic in the control of carbonate dissolution in the SCS. In this case, regardless of depth, variations in the  $\text{CaCO}_3$  content during the transition between the Last Glacial Maximum and Holocene were associated with changes in the rate of dilution by noncarbonate sediments and not with variations in the CCD position observed in the western Pacific during the same period.

Here, we present a new planktonic foraminiferal record from Hole U1431D retrieved from the East SCS sub-basin deep sea during International Ocean Discovery Program (IODP) Expedition 349. Changes in carbonate preservation and dissolution were investigated based on PF total abundance, total organic carbon (TOC), the foraminiferal fragmentation index (FI%) and the foraminiferal dissolution index (FDX). We evaluated these indexes considering their application in a deep-sea record and their variations in response to palaeoceanographic changes in the SCS during the last 600 kyr.

## **2. Regional setting**

The SCS is a semi-enclosed basin with an average depth of 1200 m and a maximum depth of 5500 m (Figure 1.1). The basin is characterized by its rhomboidal

shape with a NE-SW oriented axis (Wang; Li, 2009; He; Wu, 2013). The modern SCS lysocline is located at approximately 3000 m and the CCD is located between 3500 and 3800 m (Thunell et al., 1992; Wang et al., 1995; Regenberg et al., 2014). During the last glacial period, these depths were even greater, with the CCD at least 400 m deeper than present (Thunell et al., 1992).

The oceanographic patterns (*i.e.*, sea surface temperature, surface currents, and PP conditions) of the SCS respond to seasonal East Asian Monsoon (EAM) dynamics and the water exchange with the Pacific Ocean (Wang; Li., 2009; Liu et al., 2010; He; Wu, 2013; Su et al., 2013). The SCS deep waters originate in the Pacific and penetrate the marginal basin through the Luzon Strait by the Kuroshio Current (KC) (Miao; Thunell, 1994; Chen et al., 2001). Due to its short residence time (30-50 years) the amount of particulate matter decomposition in the water column is not sufficient to produce large physico-chemical changes in pH and dissolved CO<sub>2</sub> concentrations. Thus, the deep-water chemical properties in the SCS are similar to those in the Western Pacific (Miao; Thunell, 1994; Chen et al., 2001). Intense deep-water ventilation, and warm deep (>2 °C) and surface (>28 °C) waters, favor SCS surface sediments CaCO<sub>3</sub> preservation, which present CaCO<sub>3</sub> contents above 10% at depths ~3500 m, close to the position of the modern CCD (Figure 1.1b) (Wang, 1999; Wang et al., 2014; Wang; Li, 2009; Zhang et al., 2015).

The seasonal KC inflow into the northern SCS is favored by the strong East Asian Winter Monsoon (EAWM) winds (Xue et al., 2004; Liu et al., 2013). This Western Pacific boundary current transports heat from low to mid-latitudes (Qiu, 2001) and forms an anticyclonic current loop at the northeastern SCS, impacting the oceanic circulation (Xue et al., 2004; Liu et al., 2013). The KC branches in the SCS also affect the west and east SCS, producing cyclonic eddies (Xue et al., 2004; Liu et al., 2013). As the KC inflows into the SCS, its nutrient-enriched subsurface waters are brought to the surface via upwelling driven by different processes, such as wind-driven upwelling, vertical mixing or cyclonic eddies (Guo et al., 2012; Chen et al., 2003, 2017).

In general, the modern SCS has low PP, except for in wind-driven upwelling areas in the western and eastern subbasins that are caused by East Asian Summer Monsoon (EASM) and EAWM winds, respectively (Liu; Chai, 2009). However, in the northern and southern subbasins, relatively high PP occurs during winter in response to increased vertical mixing promoted by the strengthened EAWM NE winds (Tian et al., 2005; He et al., 2013; Su et al., 2013; Su et al., 2015).

### 3. Materials and methods

Hole U1431D (15°22'N, 117°00'E, 4240 m water depth, 617 m of sediment recovery) was retrieved from the SCS East subbasin (Figure 1.1a) during the IODP Expedition 349 on board the R/V *JOIDES Resolution*. For this study, subsamples (N=99) of approximately 10 cm<sup>3</sup> were sampled in 20 cm intervals from the first 20 mbsf (sections 3H to 1H from Unit I, Li et al., 2015a) of the sedimentary column, except for between sections 3H1W and 2H5W, where there was no sedimentary recovery (Li et al., 2015a).

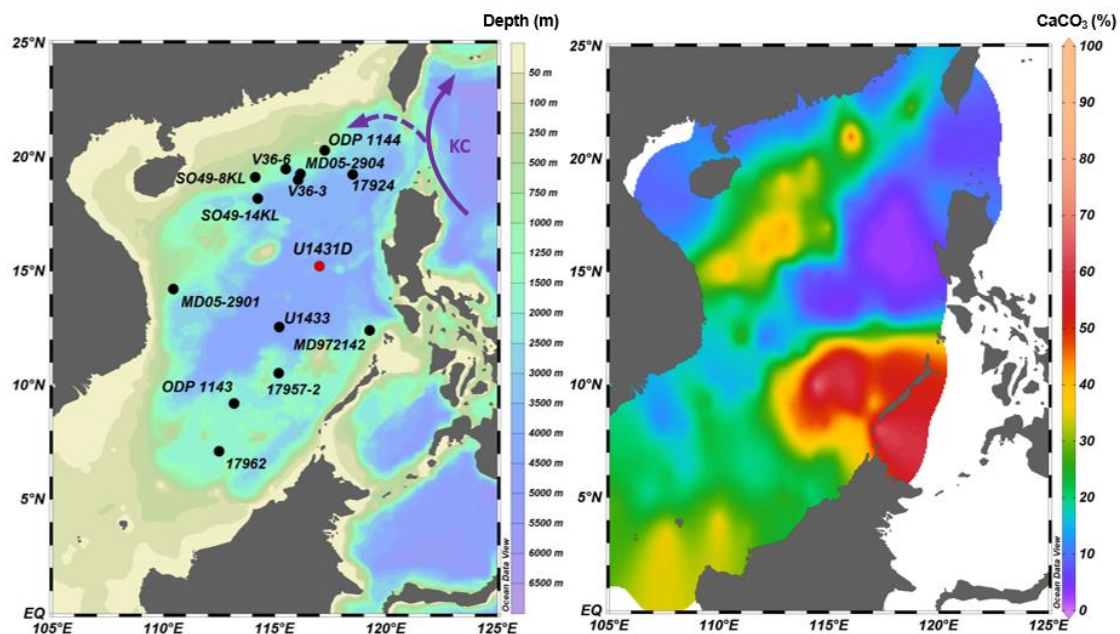


Figure 1.1 Map of the South China Sea showing (a) the Kuroshio Current (KC) and intrusion (purple dashed line) into the basin, bathymetry and the locations of Hole U1431D (this study) and the cores S049-14KL, S049-8KL, V36-3, V36-6 (Wang et al., 1995), 17957-2 (Li et al., 2001), 17962 (Xu et al., 2005), 17924, ODP 1144 (Wang et al., 2016), ODP 1143 (Liu et al., 2008), MD97-2142 (Chen et al., 2003), MD05-2901, MD05-2904 (Su et al., 2013) and Hole U1433 (Zhou et al., 2019) cited and presented in the discussion; and the (b) calcium carbonate (CaCO<sub>3</sub> %) distribution in surface sediments (From Zhang et al., 2015). The figures were plotted with ODV software (Schlitzer, 2019).

#### 3.1 Chronology

The chronology of the first 21 m of Hole U1431D was estimated using an excess <sup>230</sup>Th method described by Ferreira et al. (2015). <sup>230</sup>Th (half-life = 75.380 yr) is suitable to assess mean sedimentation rates and core chronology for samples up to 700 ka old (Ferreira et al., 2015), especially in areas rich in Th, which originates from the fluvial discharges from several nearby river basins, and with high sedimentation rates. The

technique is based on the fact that newly deposited sediments contain an excess of  $^{230}\text{Th}$  ( $^{230}\text{Th}_x$ ), whose activity is not supported by its parent  $^{234}\text{U}$ , which is also present in deposited sediments. Thus, this unsupported  $^{230}\text{Th}$  (taken as the difference between total  $^{230}\text{Th}$  and  $^{234}\text{U}$ ) varies over time, beginning at the moment of sediment deposition.

The activities of the radionuclides of interest ( $^{230}\text{Th}$  and  $^{234}\text{U}$ ) were determined in 16 samples distributed along the first 21 m Hole U1431D at the Laboratory of Inorganic Marine Chemistry (LaQIMar) of the Oceanographic Institute (IOUSP). The analysis was carried out in a high-resolution gamma spectrometer (EG&G ORTEC, model 25190P) following all analytical procedures described by Ferreira et al. (2015). The analytical quality control was evaluated with the determination of these nuclides in certified reference materials (IAEA326, and IAEA327) ( $n = 4$ ), and this determination showed satisfactory precision and accuracy, as neither the mean deviations nor errors exceeded 10%.

Excess  $^{230}\text{Th}$  values were used to estimate mean sedimentation rates ( $v$ ) (Equation 1) and to establish an age-depth model (Equation 2). This obtained chronology was then compared with an age-depth model derived from bio and magnetostratigraphic data reported by Li et al. (2015a), which were based on radiolarians, calcareous nannofossils and PF occurrences, and on the placement of the Bruhes/Matuyama boundary (780 kyr, GSSP - Global Boundary Stratotype Section and Point - for the starting point of the Middle Pleistocene).

$$V = (\lambda \cdot D)/a \text{ (Eq. 1)}$$

$$I = z/v \text{ (Eq. 2)}$$

In which,  $v$  is the mean sedimentation rate (in  $\text{cm kyr}^{-1}$ );  $\lambda = ^{230}\text{Th}$  decay constant ( $= 9.20 \cdot 10^{-6} \text{ yr}^{-1}$ );  $D$  = sediment core length (in cm);  $a$  = angular coefficient of the regression between  $\ln(^{230}\text{Th}_{xs})$  and  $z$ ;  $z$  = depth of the given core section (in cm);  $I$  = age of deposition of a given core section (year).

The existing age model for Hole U1431D is based only on two biostratigraphic events for the first 21 m (Table 1.2, Li et al., 2015a), whereas the age model based on the excess  $^{230}\text{Th}$ , relies on 16 samples within the same core section. Deviations between both models are expected since the shipboard data does not contemplate the whole scenario of changes in sedimentation rates, which are better observed with the excess  $^{230}\text{Th}$  variation.

### 3.2 Total organic carbon

For total organic carbon (TOC) content, 50 samples were analyzed. The Fourier Transform Infrared Spectroscopy (FTIRS) analyses of the samples was performed in diffuse reflectance mode, with the aid of a VERTEX 70 FTIRS spectrometer (BrukerOptik GmbH, Germany) equipped with a diffuse reflectance accessory ("Praying Mantis" Harrick Inc., USA). Sample pretreatment, IR spectroscopy measurement conditions and processing procedures applied to the raw spectra are described by Rosén et al. (2010). TOC content values (% in weight) were inferred using an internal calibration based on 23 samples measured using an elemental analyzer for carbon content (AG Hinrichs MARUM).

### 3.3 Planktonic foraminiferal analysis

For this study, each sample of the first 21 m from Hole U1431D was weighed (~10 g), shaken in a table for 2 hours for sediment disaggregation, washed with water in a 63 µm mesh sieve, and then oven-dried at 40°C.

Samples were dry sieved in a 150 µm mesh sieve, and at least 300 specimens per sample were picked and identified under a stereomicroscope. Tests were identified following the taxonomy of Parker (1962), Bé (1967) and Hemleben et al. (1989). Planktonic foraminifera tests were quantified to estimate total abundance (tests/g of dry sediment). Samples with no PF (N=21) were removed to calculate the following carbonate dissolution proxies.

#### 3.3.1 Proxies for carbonate dissolution

The percentage of PF fragments (FI%) (Le; Shackleton, 1992) and the FDX (Berger, 1968; 1975) were used as dissolution proxies in this study.

The FI% responds to dissolution effects, as it affects the strength of foraminiferal walls, making them more susceptible to breaking into fragments (Berger, 1970; Malmgren, 1983; Le; Shackleton, 1992). In intermediate and deep waters, FI% increases with water depth, with values above 20% expected for depths greater than 3500 m, indicating high carbonate dissolution near to the CCD (Le; Shackleton, 1992). Thus, a high (low) FI% indicates stronger (weaker) dissolution effects (Le; Shackleton, 1992). This index considers that one complete foraminiferal specimen may break into 8 fragments (Le; Shackleton, 1992) and was calculated according to the following formula:

$$FI\% = 100 \times (\text{number of fragments}/8) / [(\text{number of fragments}/8) + \text{number of complete species}] \text{ (Eq. 3)}$$

To calculate the FDX (Equation 4; Berger, 1968), the PF species were assigned to dissolution resistance groups following Berger (1975) (Table 1.1). Higher (lower) values of the FDX are expected to reflect stronger (weaker) dissolution effects over the PF shells because dissolution-resistant species are more able to resist corrosive environments than less resistant species (Berger, 1975; Wang et al., 2016). However, FDX values must be applied and interpreted with caution, since the proportions of foraminifera species are also influenced by paleoclimate and foraminiferal paleoecology (Martínez, 1994).

$$FDX = \Sigma(\rho_i R_i) / \Sigma \rho_i \text{ (Eq. 4)}$$

$\rho_i$  = percentage of species  $i$ ;  $R_i$  = dissolution group number of species  $i$

Table 1.1. Planktonic foraminiferal species found in Hole U1431D and assigned a dissolution resistance group number ranked from the least to the most resistant group (Berger, 1975).


Low resistance	Group number	High resistance	Group number
<i>Globigerina rubescens</i>	2	<i>Globorotalia crassaformis</i>	5
<i>Globigerinella bulloides</i>	2	<i>Globorotalia scitula</i>	5
<i>Globigerinoides ruber</i> <i>white</i>	2	<i>Globorotalia hirsuta</i>	6
<i>Globoturborotalita tennela</i>	2	<i>Globoconella inflata</i>	7
<i>Candeina nitida</i>	3	<i>Globorotalia truncatulinoides</i>	7
<i>Globigerina falconensis</i>	3	<i>Neogloboquadrina dutertrei</i>	7
<i>Globigerinella siphonifera</i>	3	<i>Neogloboquadrina incompta</i>	7
<i>Globigerinoides</i> <i>conglobatus</i>	3	<i>Neogloboquadrina spp</i>	7
<i>Trilobatus sacculifer</i>	3	<i>Tenuitella iota</i>	7
<i>Orbulina universa</i>	3	<i>Globorotalia menardii</i>	8
<i>Globigerinita glutinata</i>	4	<i>Globorotalia tumida</i>	9
<i>Globigerinella calida</i>	4	<i>Neogloboquadrina</i> <i>pachyderma</i>	9
		<i>Pulleniatina obliquiloculata</i>	9
		<i>Sphaerodina dehiscentis</i>	9
		<i>Turborotalita quinqueloba</i>	9

## 4. Results


### 4.1 Core description and chronology


The upper 21 m of Hole U1431D, analyzed here, belongs to the Unit I (0-101.6 mbsf) described by Li et al. (2015a) as composed by dark greenish gray clays and silty clays with minor clayey silt. Foraminifer ooze and nannofossil-rich clay found in Unit I were interpreted as turbidite sequences (Li et al., 2015a), with high abundances of PF at core sections 3H7 to 3H6 and 2H4 to 2H2 (Table 1.2).


Table 1.2. Hole U1431D Unit I lithology (Modified from Li et al., 2015a) and PF total abundance from core sections 3H to 1H. Low (L) = 10-32 specimens / at least 30% of samples; Common (C) = 32-100 specimens / at least 30% of samples; Frequent (F) = > 100 specimens / at least 30% of samples; Abundant (A) = > 300 specimens / at least 30% of samples. (\*) Sections where samples with no-foraminifera are recorded.

Hole U1431D			
Top Depth CSF-B (m)	Core section	Abundance	Lithology
0.59	1H-1*	L	
1.49	1H-2*	L	
2.48	1H-3	C	
3.21	2H-1*	C	
4.7	2H-2*	A	
6.2	2H-3	A	
7.7	2H-4*	A	
9.2	2H-5*	C	
12.88	3H-1*	F	
14.28	3H-2	F	
15.82	3H-3*	F	
17.36	3H-4	F	
18.76	3H-5*	F	
20.4	3H-6*	A	
21.41	3H-7	A	

Unit I (0-101.16 mbsf)  
Dark greenish gray clay and silty clay with minor clayey silt

 Clay/Claystone

 Silt/Siltstone

 Carbonate

Low (L) = 10-32 specimens/at least 30% of samples  
 Common (C) = 32-100 specimens/at least 30% of samples  
 Frequent (F) = >100 specimens/at least 30% of samples  
 Abundant (A) = >300 specimens/at least 30% of samples  
 \*Sections where samples with no-foraminifera are recorded



According to the  $^{230}\text{Th}$  chronology, the uppermost 21 m of Hole U1431D comprises sediments from the middle Pleistocene (up to MIS 14) to the present, with mean sedimentation rates of  $11.13 \pm 0.83 \text{ cm kyr}^{-1}$  between 20 and 13 mbsf and of  $2.86 \pm 0.21 \text{ cm kyr}^{-1}$  for the upper 13 mbsf of the (Figure 1.2 and Supplementary Material 1.1 – Appendix A). Deviations between 4% and 14% were observed between the excess  $^{230}\text{Th}$  age-depth model and Li et al. (2015a) biostratigraphy and magnetostratigraphy based age model (Table 1.3 and Supplementary Material 1.2 – Appendix B).

Table 1.3. Biostratigraphy and paleomagnetic events of Hole U1431D (FAD = First appearance datum; LAD = Last appearance datum).

Depth (mbsf)	Age (ka)		Event
	Value	Adjustment	
0	0	0	0
3,16	210	167	FAD <i>Emiliana huxleyi</i>
12,15	420	452	FAD <i>Collosphaera tuberosa</i>
32,08	610	583	LAD <i>Gephyrocapsa</i> spp.
46,00	780	815	Brunhes/Matuyama paleomagnetic boundary
50,90	1040	1021	FAD <i>Gephyrocapsa</i> spp.

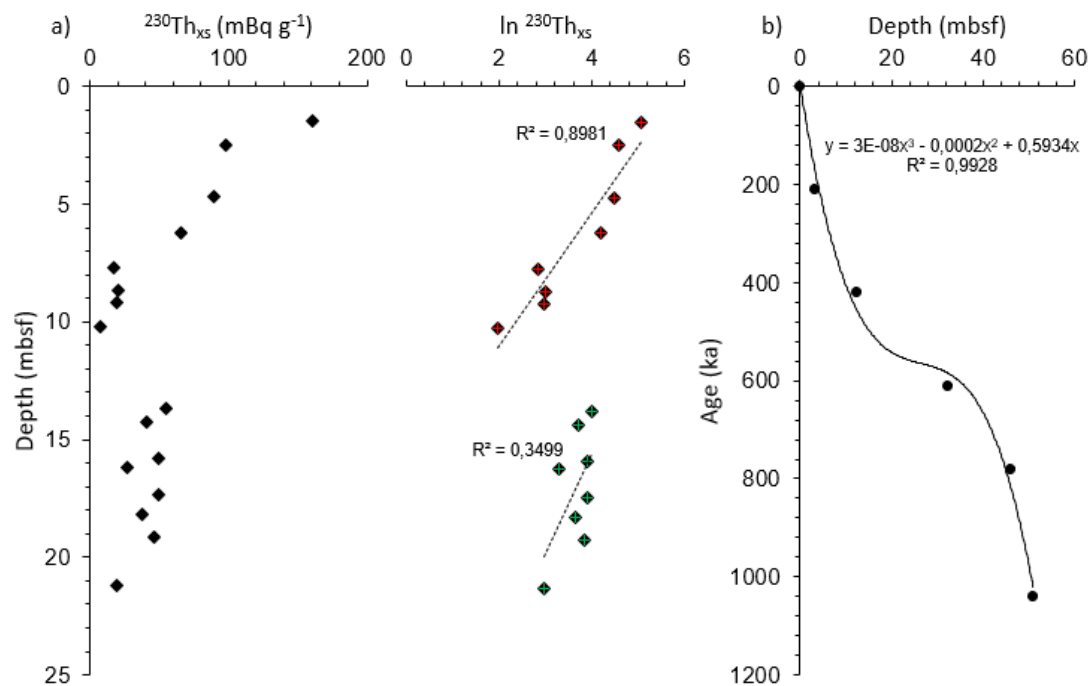


Figure 1.2. Hole U1431D (a) vertical and linearized activity profile of excess  $^{230}\text{Th}$  (in Bq kg $^{-1}$ ) and (b) the age model based on the  $^{230}\text{Th}$  (ka) obtained.

#### 4.2 Total organic carbon

The TOC contents range from 0.03 to 0.45% in weight, with no visible glacial/interglacial pattern (Figure 1.3b). MIS 14 and 12 sediments present high TOC values (~ 0.4%), with the highest value recorded at MIS 9 (0.45%). From MIS 9 towards MIS 6, relatively high values (>0.15%) with several oscillations are observed. After MIS 6, TOC values present a gradually decreasing trend towards the present.

#### 4.3 Planktonic foraminiferal assemblages

In general, Hole U1431D samples have low PF total abundance that varies from 0 to 296 tests/g dry sediment (Figure 1.3a). A low PF total abundance, varying from 0 to 63 tests/g dry sediment, is observed from MIS 14 to MIS 12, except for one sample during MIS 14 (21.02 mbsf), which has 170 tests/g dry sediment. MIS 10 and MIS 9 have low PF abundances varying from 0 to 32 tests/g dry sediment. Increased values are observed during MIS 8 and MIS 7 (from 16 to 296 tests/g dry sediment). The transition between MIS 7 and MIS 6 (Figure 1.3a) is marked by a decrease in PF total abundance, and there is an increase in PF total abundance during MIS 5, with values ranging from 0 to 105 tests/g dry sediment. After MIS 5, towards the present, low PF total abundance values are recorded, with 0 to 10 tests/g dry sediment.

In general, FI% values observed along the first 21 m of Hole U1431D present a mean value of 4%, varying between 0 and 28% (Figure 1.3c). From MIS 14 to MIS 12, the FI% varies from 0 to 18%, except for in one sample during MIS 14 (3H5 W 86/88), which has FI% values close to 28%. Lower FI% values between 0.3 and 13% are observed during MIS 8, MIS 7 and MIS 6, and there is an increasing trend in these index values after MIS 5 to MIS 1.

The FDX presents values between 2.0 and 6.5 throughout the first 21 m of Hole U1431D (Figure 1.3d). Between MIS 14 and MIS 12, the FDX values vary from 2.8 to 6.5, and the FDX values are between 3.2 and 5.9, during MIS 8 and MIS 7. During MIS 6 the FDX values are lower, ranging between 2.6 and 4.6, and between 2.0 and 6.5 from MIS 5 to MIS 1.

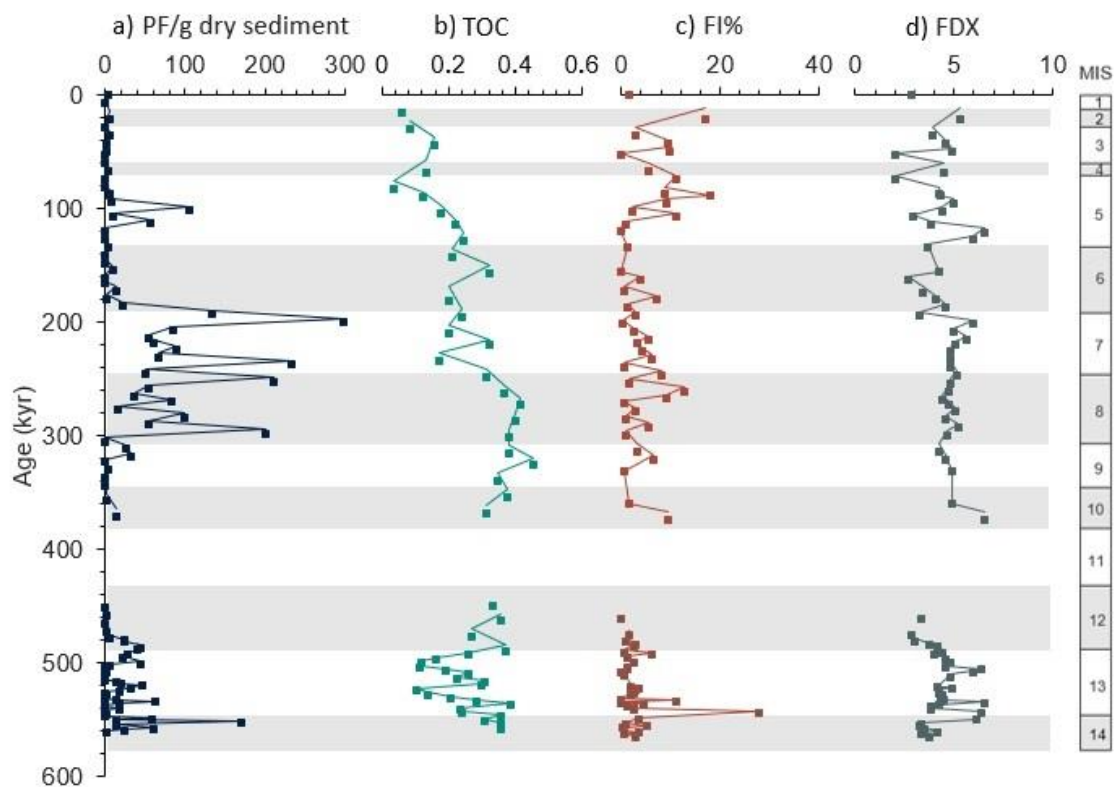


Figure 1.3. Hole U1431D a) planktonic foraminifer (PF) total abundance; b) total organic carbon (TOC); c) fragmentation (FI%) and d) foraminiferal dissolution (FDX) indexes values. During the period between 460 and 370 ka, there was no sedimentary recovery. Gray bars indicate glacial periods (Lisiecki; Raymo, 2005).

## 5. Discussion

The low general PF total abundance found in Hole U1431D (Figure 1.3a) indicates that our record has been under partial dissolution effects during the last 600 kyr. An exception occurs during MIS 8 and 7, where increased PF abundances indicate possible changes in the depth of the lysocline and CCD, PP, or turbidite influence. From these perspectives, we discuss the studied indexes compared to other published SCS records (Figure 1.1, Table 1.4).

Table 1.4. The location and data type of SCS marine records discussed here.

Core ID	Location (Lat., Long.)	Water depth (m)	Proxy	References
Hole U1431D	15°22'N, 117°00'E	4240	PF total abundance, TOC, FI%, FDX	This study
Core S049- 14KL	18°18'N, 114°24'E	3624	PF total abundance	Wang et al., 1995

Core S049-8KL	19°11'N, 114°12'E	1040	PF total abundance	Wang and Wang, 1990
MD97-2142	12°41'N, 119°27'E	1557	TOC	Chen et al., 2003
Core 17957-2	10°53'N, 115°18'E	2795	FI%	Li et al., 2001
Core 17962	7°11'N, 112°5'E	1968	FI%	Xu et al., 2005
ODP 1144	20°3'N, 117°25'E	2037	FDX	Wang et al., 2016
Core 17924	19°24'N, 118°50'E	3440	FDX	Wang et al., 2016
Core V36-3	19°01'N, 116°06'E	2809	FDX	Wang et al., 1995
Core V36-6	19°47'N, 115°49'E	1579	FDX	Wang et al., 1995
ODP 1143	9°21'N, 113°17'E	2772	<i>Florisphaera profunda%</i>	Liu et al., 2008
MD05-2901	14°22'N, 110°44'E	1454	<i>Florisphaera profunda%</i> and <i>Gephyrocapsa oceanica%</i>	Su et al., 2013; Li et al., 2015
MD05-2904	19°27'N, 116°15'E	2066	<i>Florisphaera profunda%</i>	Su et al., 2013
Hole U1433	115°2'E, 12°55'N	4372	PF scanning micrograph	Zhou et al., 2019

### 5.1 Controlling factors of planktonic foraminifera abundances in deep-sea SCS sediments

Modern SCS sediments present a bathymetric gradient in PF total abundance, with higher (lower) values observed at shallower (deeper) parts of the basin (Pflaumann; Jian, 1999), following the vertical gradient of the carbonate saturation limits (Berger, 1970). Pflaumann and Jian (1999) reported PF total abundance to be between 206 and 756 tests/cm<sup>3</sup> in sediments at intermediate water depths (370 – 2000 m water depth, above the lysocline), between 2 to 417 tests/cm<sup>3</sup> in water depths from 2000 m to 3000 m (limit of the lysocline), and between 29 to 40 tests/cm<sup>3</sup> below 3000 m (below the lysocline). In this sense, PF abundances close to 0 are expected in depths close/under the position of the lysocline. Our record, retrieved at a water depth of 4240 m from the eastern SCS subbasin, has PF total abundance values from 0 to 296 tests/g dry sediment (Figure 1.3a).

All MIS stages recorded in the first 21 m of Hole U1431D presented PF, even if characterized by low abundances. Similarly, samples with no foraminifera (N=21) were also recorded throughout the studied section of Hole U1431D, except for MIS 8, with only one barren sample during the MIS 9/8 transition, and for MIS 7. Thus, considering

the vertical dissolution gradient where the presence (absence) of PF is associated with a core site position above (below) the CCD, our data suggest that during MIS 8 and 7, the core site was above the CCD at all times.

Glacial and interglacial patterns in PF total abundance have been reported for the SCS, and attributed mainly to CCD position fluctuations, following Atlantic or Pacific-type cycles at depths both above or below the lysocline, respectively. At the northern SCS, a below the lysocline site (Core S049-14KL) recorded higher PF abundances during MIS 4, early MIS 3, and MIS 2, due to a deeper CCD position associated with changes in Pacific deep-waters (Figure 1.4b, Wang et al., 1995). Higher PF abundances recorded above the lysocline (Core S049-8KL) during glacial stages MIS 6 and 2 (Figure 1.4c, Wang; Wang, 1990) are well correlated with increased PP, shown by the proportion of high and low productivity benthic foraminifera species as well as by carbon isotopes of *T. sacculifer* (Wang, 1994). Nevertheless, in our data, no glacial/interglacial PF total abundance pattern is observed.

In the SCS, between MIS 12 and 8, regardless of glacial/interglacial cycles, high carbonate production and accumulation showed by the coccolithophore record has been attributed to the Mid-Brunhes Dissolution Interval (MBDI) (Liu et al., 2008; Wang; Tian, 2014; Figure 1.5d). During the MBDI (between MIS 14 and 7), PP driven carbonate accumulation is observed globally, regardless of the glacial/interglacial cycles. The carbonate accumulated in some basins possibly triggered a  $\text{CaCO}_3$  dissolution event to balance the global carbonate cycle (Farrell; Prell, 1989; Weedon; Hall, 2002; Baumann; Freitag, 2004; Barker et al., 2006; Sun et al., 2017; Saavedro-Pellitero et al., 2019). According to Liu et al. (2008), at the SCS, PP changes that occurred during the MBDI were related to nutricline depth fluctuations, which during glacial/interglacial cycles are controlled by the EAM dynamics. The southeastern SCS (MD97-2142) also records the MBDI, through a long-term TOC increase associated with PP increase (Figure 1.5e, Chen et al., 2003; Shiau et al., 2008). At this site, due to its proximity to river discharges from the continent, the dilution effects driven by the continental sediment input during sea-level changes prevail over the TOC record, also imprinting a glacial-interglacial pattern (Chen et al., 2003; Shiau et al., 2008).

The PF abundances observed between MIS 14 and 7 at Hole U1431D, probably reflect the MBDI increased carbonate accumulation event (Figure 1.5). Additionally, the relatively higher TOC values recorded during MIS 10, 9, 8, and 7 could also be related to

the increased carbonate production during this event as, according to the ballast hypothesis, increased  $\text{CaCO}_3$  flux result in higher organic carbon flux to the deep-sea floor (Barker et al., 2006). Thus, the similar TOC and PF total abundance patterns observed at Hole U1431D suggest a link between PP and PF shell flux to the seafloor at this portion of the SCS, specifically during MIS 8 and 7.

It is important to highlight that previous studies have shown that substantial carbonate dissolution occurs in the deep central SCS basin, leaving carbonate-poor surface sediments (Zhang et al., 2015; Luo et al., 2018). Therefore, at the deep western and northern SCS subbasins, the enrichment of PF in deep-sea records has been attributed to be a result of turbidity deposits (Suess, 2005; Li et al., 2015b; Li et al., 2017b; Wu et al., 2019; Zhou et al., 2019), bringing carbonate particles previously deposited at shallower depths to below the CCD depths. However, our records' PF total abundance values are in accordance to PF abundances in core tops correspondent to modern deep-sea sediment, except for MIS 8 and 7, which suggests that at these intervals the PF abundance record could have been a result of turbidite deposition, rather than changes in carbonate preservation.

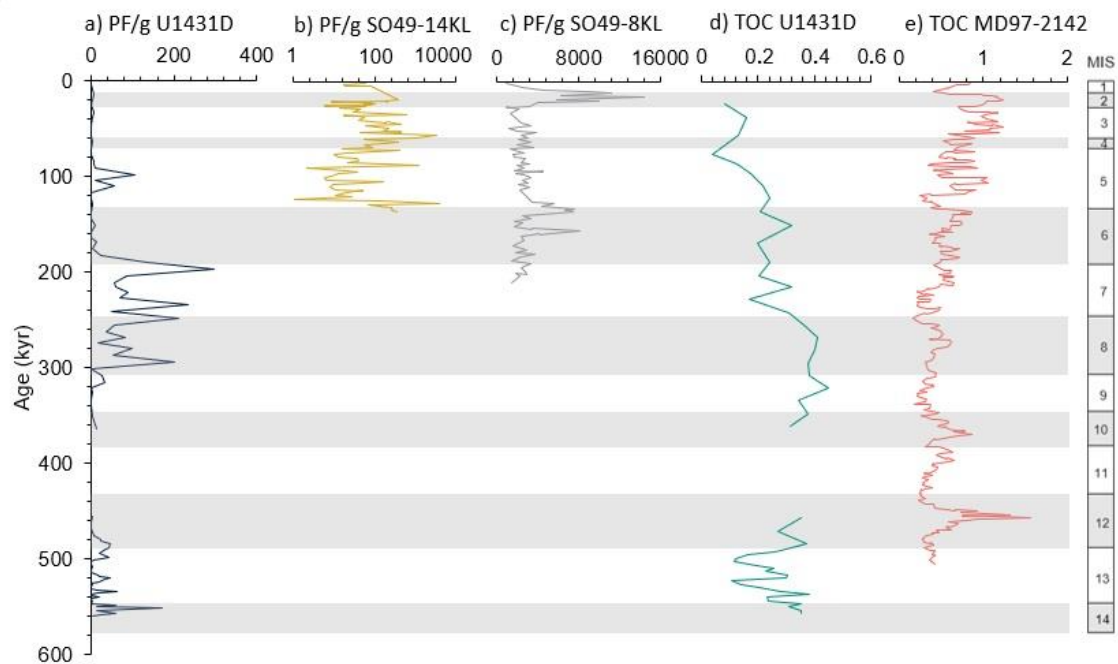


Figure 1.4. Planktonic foraminifera (PF) abundance per gram sediment from a) Hole U1431D (4240 m water depth, this study), b) Core SO49-14KL (3624 m water depth, Wang et al., 1995) and c) Core SO49-8KL (1040 m water depth, Wang; Wang, 1990) ; and total organic carbon (TOC) content in weight (%) from d) Hole U1431D (4240 m water depth, this study) and e) MD97-2142 (1557 m water depth; Chen et al., 2003).

## 5.2 Limitations of using planktonic foraminiferal dissolution indexes

FI% is a commonly used dissolution proxy in Quaternary SCS records (Li et al., 2001; Xu et al., 2005; Wang et al., 2016). FI% values found in cores retrieved at above the lysocline (1900-3000 m) water depths follow a clear glacial-interglacial variability despite these cores retrieval depths, with higher dissolution occurring during warmer intervals (Li et al., 2001; Xu et al., 2005; Wang et al., 2016). In the last 600 kyr, for instance, FI% records from the southern SCS (Core 17957-2, FI% values between approximately 2 – 9 %) reflect a “Pacific-type” cycle, even above the lysocline, with dissolution events observed during interglacial to glacial stages transitions as a result of a long-term cyclicity associated to changes in deep-water circulation (Figure 1.5b, Li et al., 2001). For Core 17962, the highest FI% values (between 20 – 40 %) are recorded during interglacial stages (Figure 1.5c, Xu et al., 2005). In this record, the strongest dissolution effects occurred during specific periods of surface water exchange between the SCS and the warm and productive waters of the Indian Ocean, resulting in a reduction in *P. obliquiloculata*, the most dissolution resistant species recorded in the core (Xu et al., 2005). This species is favored by glacial environmental conditions (Xu et al., 2005), which may have resulted in high FI% values, even at depths above the lysocline. Considering that Hole U1431D retrieval depth is currently below the modern CCD, our FI% record must be interpreted with caution. Two main factors may have contributed to underestimated FI% values in this study: (i) the low abundance (<300 specimens/sample) of complete PF tests; and (ii) test/fragment dissolution, as even at periods when core site was above the CCD position, it would still be below the lysocline. In this sense, our FI% values are probably underestimated rather than reflecting changes in PF preservation.

Caution should also be taken when interpreting FDX values as carbonate dissolution proxies, especially for below the modern CCD records, such as Hole U1431D. At the SCS, surface sediments FDX values vary as a function of depth (Ding et al., 2006; Fernando et al., 2007). For example, at the eastern and western SCS, surface sediments FDX values increase from 3.2 to 5.5 with increasing water depths (from 91 m to 3010 m, Fernando et al., 2007). During the Quaternary, higher FDX values (FDX = 7) from records retrieved in the SCS, at above (ODP Site 1144) and below (Core 17924) of modern lysocline, are registered during MIS 3 when both records stayed at a below lysocline position (Wang et al., 2016). While at the northern SCS subbasin, records from above the modern lysocline (Core V36-3 and Core V36-6, Figure 1.5e,f) present FDX

values between 4.5 and 6.5 since MIS 5 (Wang et al., 1995). Although FDX values found at the upper 21 m of Hole U1431D are in accordance with those recorded for depths below the lysocline during the last 600 kyr, substantial carbonate dissolution (high FDX values) is recorded from MIS 10 to MIS 6, when PF abundance increased. On the other hand, lower FDX values (better carbonate preservation) are recorded from MIS 6 to present, when the PF abundances are low. These FDX patterns suggest that it is recording cycles of low carbonate preservation (high FDX) and non-preservation (low FDX). The non-standardized number of species in each sample may have affected the proportion of the ranked species, remaining only the most resistant species for the FDX calculus. Additionally, low PF abundances might also represent a crucial caveat for the application of these indexes. For instance, MIS 8 and 7 have relatively high PF abundances associated with relatively high FI% and FDX values. Whereas MIS 6 presents the lowest FI% and FDX values, suggesting a scenario of lower dissolution, but also very low PF abundances. This opposite pattern between the dissolution indexes and PF abundances can be observed throughout our record (Figure 1.5). Thus, even if FI% and FDX are reliable PF-based dissolution indexes, they are not recommended to assess changes in carbonate dissolution at Hole U1431D, as at this site depth, the number of complete carbonated specimens, as well as the number of fragments, are drastically affected by dissolution, compromising the interpretation of the indexes.

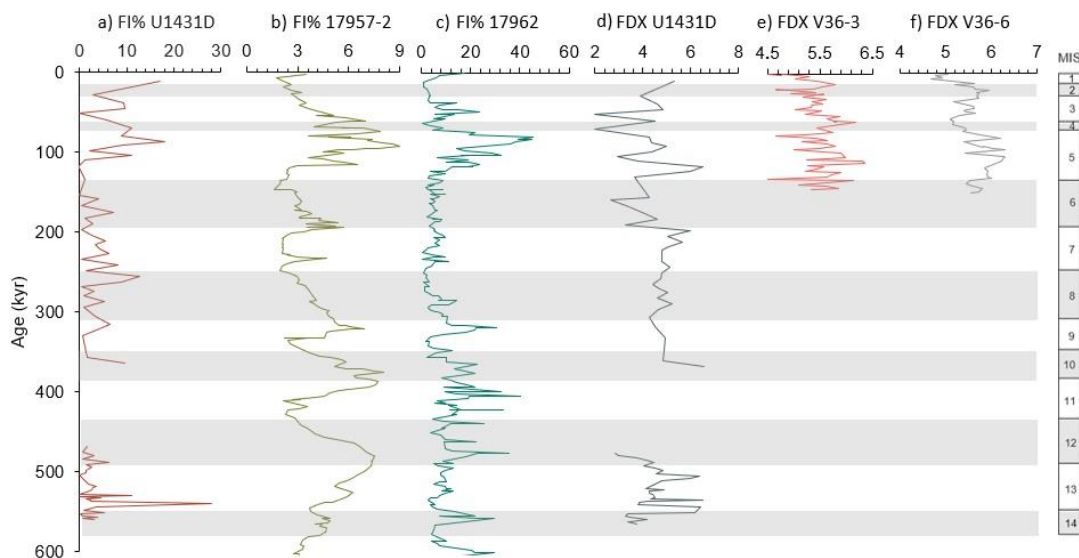


Figure 1.5. Fragmentation index (FI%) from a) Hole U1431D (4240 m water depth, this study), b) Core 17957-2 (2195 m water depth, Li et al., 2001) and c) Core 17962 (1968 m water depth, Xu et al., 2005); and foraminiferal dissolution index (FDX) from d) Hole



U1431D (this study), e) Core V36-3 (2809 m water depth, Wang et al., 1995) and f) Core V36-6 (1579 m water depth, Wang et al., 1995).

### 5.3 Increased primary productivity or turbidity sequences? What controlled planktonic foraminifera preservation during MIS 8 and 7 in the SCS

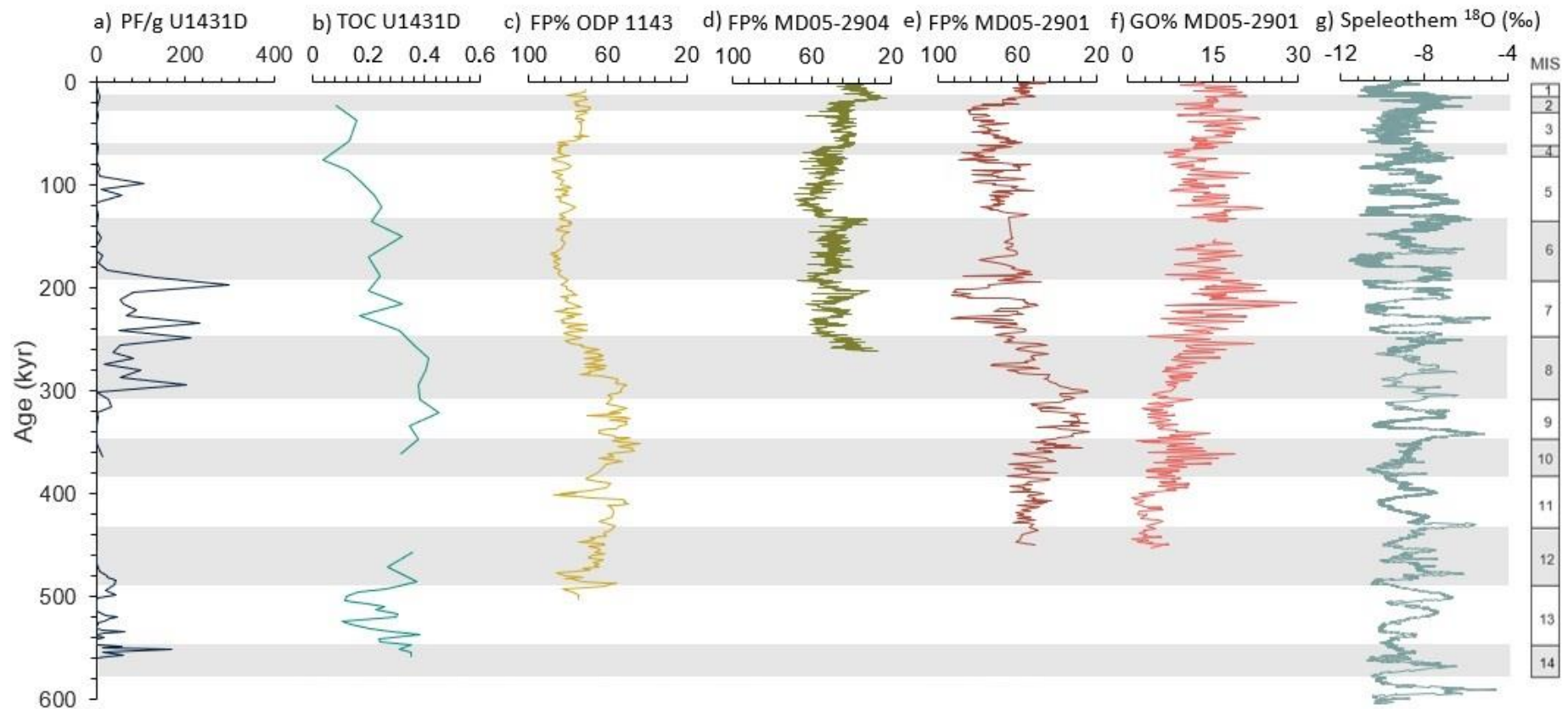
In general, during the last 600 kyr, the values obtained for PF abundance in the upper 21 m of Hole U1431D (Figure 1.3a) indicate the carbonate dissolution expected for depths below or close to the lysocline. However, despite the below modern CCD position of this record, relatively high PF abundance is observed during MIS 8 and 7. Since PF abundance in deep-sea sediments is associated with the effects of dissolution and PP (Kucera, 2007; Bordiga et al., 2013; Li et al., 2017a, 2017b), the high PF abundances observed during MIS 8 and MIS 7 may also be potentially associated with the increase in PP. Additionally, the presence of foraminifera-rich turbidite sequences could also explain the high PF abundances observed in these stages.

In general, the modern SCS has low mean annual PP, which is increased during monsoon season, when winds pump nutrients to the photic zone (Chen, 2005; Liu; Chai, 2009; Li et al., 2013). The EAM seasonal dynamics (EAWM and EASM) impact surface circulation of each of the SCS subbasins differently (Liu et al., 2002; Hess; Khunt, 2005; Su et al.; 2013; Shi et al., 2014). In the northern and southern subbasins, relatively high PP occurs during winter in response to the stronger vertical mixing promoted by EAWM NE winds (Tian et al., 2005; He et al., 2013; Su et al., 2013; Su et al., 2015), while the EASM winds promote upwelling especially in the western SCS subbasin (Liu; Chai, 2009). Hence, glacial stages have been characterized to be more productive than interglacial stages, since the EAWM is more intense than the EASM (Chen, 2005; Liu; Chai, 2009; Li et al., 2013, 2015).

When compared with paleoproductivity records from the SCS (Figure 1.6), our PF abundance and TOC values are in accordance with the slightly enhanced PP during MIS 8 and MIS 7 shown by a clear decrease in *Florisphaera profunda* abundances at records from the southern, northern and western SCS subbasins at sites ODP 1143 (Liu et al., 2008), MD05-2904 (Su et al., 2013) and MD05-2901 (Su et al., 2013), respectively (Figure 1.6c, d, e). Enhanced PP during MIS 8 is associated with stronger EAWM winds promoting upper water mixing, thus supplying nutrients to the surface waters (Su et al., 2013; Zhang et al., 2016; Figure 1.6). In contrast, during MIS 7, high abundance of *Gephyrocapsa oceanica* and an abrupt decrease in *F. profunda* observed at the western

SCS subbasin (core MD05-2901, Su et al., 2013) would be a result of upwelling occurrence induced by the southerly EASM winds (Su et al., 2013; Li et al., 2015; Figure 1.6f, g). The strengthening of the EASM over the last ~400 kyr is recorded in Chinese cave speleothems, evidenced by more negative  $\delta^{18}\text{O}$  values (Cheng et al., 2009; Figure 6g). Additionally, Shiao et al. (2008) suggest that since the end of the MBDI (~330 kyr), PP in the SCS (Figure 1.4e) responded positively to strengthened EAM dynamics. Thus, during MIS 8 and 7, higher PF total abundance and TOC values in Hole U1431D may have been a result of increased PP promoted by monsoonal driven hydrodynamic changes in the eastern SCS subbasin.

The presence of PF in a below the modern CCD site, at the southern subbasin of SCS (Hole U1433, Zhou et al., 2019), was associated with carbonate transport promoted by turbidite current as a consequence of the subduction processes at the Manila Trench during the late Miocene. The shipboard description of sections U1431D-3H to U1431D-2H (MIS 14 to 5) characterizes it as a turbidite sequence possibly related to the occurrence of earthquakes generated by the subduction zone of the Luzon Arc or triggered by volcanism (Li et al., 2015a). Hence, the role of these gravity flows in the preservation of the PF in our 600 kyr-record should be considered. The presence of mixed resistant and non-resistant planktonic foraminiferal species along the record typical of a rapid burial (Lagoe, 1986) corroborate to this. These rapid gravity flows are commonly characterized by high sedimentation rates (SR), such as those observed in Section U1431D-3H (SR= 11,11 cm/kyr), resulting in an abundant PF fauna in the interval that corresponds to MIS 14 to 12 (Table 1.2). The abundant fauna observed at Sections U1431D-2H-4W to U1431D-2H-2W, comprising MIS 8 and 7, however, corresponds to lower SR (=2,86 cm/kyr). Hence, although turbidite deposits may have influenced PF abundances and carbonate preservation at Hole U1431D, they were not the main drivers of the high PF abundances during MIS 8 and 7.



1

2 Figure 1.6. a) Planktonic foraminiferal total abundance and b) total organic carbon from Hole U1431D (this study) compared to paleoproductivity  
 3 records based on *Florisphaera profunda*% from the c) Southern SCS (ODP 1143; Liu et al., 2008), d) Northern SCS (MD05-2904; Su et al., 2013),  
 4 e) Western SCS (MD05-2901; Su et al., 2013) and based on *Gephyrocapsa oceanica*% from the f) Western SCS (MD05-2901; Li et al., 2015,  
 5 supplementary material) and g) Stacked speleothem  $\delta^{18}\text{O}$  from Chinese Caves reflecting both summer (low  $\delta^{18}\text{O}$ ) and winter (high  $\delta^{18}\text{O}$ ) monsoon  
 6 signals (Cheng et al., 2009). The FP% scales were reversed for comparison with primary productivity since it presents a negative relationship.  
 7

## **6. Conclusions**

The low PF abundance from the upper 21 m of Hole U1431D (4240 m water depth) suggests that our record has been under strong carbonate dissolution associated with its position below/close to the lysocline during the last 600 kyr. Overall, PF abundance and TOC contents fluctuations were associated with enhanced PP, mainly driven by the EAM dynamics during the MBDI event. The FI% and FDX indexes, commonly used as dissolution indexes, did not record changes in carbonate dissolution at this below the modern CCD position site. The presence of turbidity deposits may have influenced the PF record of Hole U1431D but was not the main factor controlling MIS 8 and 7 carbonate preservation. However, further studies tracing the source of these turbidity sequences in eastern SCS subbasin are necessary to constrain better these deposits dynamics and role in the preservation of deep SCS carbonates.

## **Acknowledgements**

This research used samples and data provided by the International Ocean Discovery Program (IODP). The science party members, crew, and technicians aboard the R/V JOIDES Resolution are acknowledged for their work during IODP Expedition 349. Funding was provided by IODP/CAPES-Brasil (Edital 38/2014), Fundação de Amparo à Pesquisa do Estado de São Paulo (FAPESP; Proc. n°.2015/11832-2) and Coordenação de Aperfeiçoamento de Pessoal de Nível Superior – Brasil (CAPES) - Finance Code 001. This research was also supported financially by Swiss National Science Foundation Advanced Postdoc Mobility grant (P300P2\_164634) to IHA.

## CHAPTER II

### A deep-sea record of late Quaternary terrigenous input to the northeastern South China Sea (IODP Hole U1432C)

Manuscript in preparation for submission to the *Palaeogeography, Palaeoclimatology, Palaeoecology*. This manuscript is co-authored by Rubens Cesar Lopes Figueira, Paulo Alves de Lima Ferreira, Felipe Rodrigues and Renata Hanae Nagai

#### Abstract

Here we investigate the last 230 kyr terrigenous input changes to the northeast South China Sea (SCS) deep-sea based on physical and geochemical properties of sedimentary record Hole U1432C (3829 m water depth) retrieved by the International Ocean Discovery Program (IODP) Expedition 349. Natural gamma radiation (NGR), Ti/Ca, and Al/K data suggest higher terrigenous supply during the interglacials MIS 7 and 5 in response to intense chemical weathering, mainly during MIS 5, and relatively lower terrigenous contribution from MIS 4 to the Present. The principal component analysis (PCA) for major and trace elements, resulted in three components that together explained 78.53% of the data variation. The PCA separated terrigenous elements associated with leaching and chemical weathering processes, such as Al, Ba, Cr, Cu, Fe, K, Ni, Ti, V, and Zn (PC1); from biogenic origin elements such as Ca and Sr (PC2); and terrigenous source elements associated with intense chemical weathering, such as Al, Mg and Sc (PC3). Hole1432C major and trace elements sediments composition suggests increased terrigenous input during the interglacials MIS 7 and 5, higher during MIS 5, and less contribution from MIS 4 to the Present. In contrast, the biogenic marine elements presented a low and constant supply from MIS 7 to 5, lower contribution during MIS 5, and an increase from MIS 4 to the Present. Our data suggest that the terrigenous supply drives the marine biogenic contribution at this site according to dilution. The more significant contribution of terrigenous input during MIS 7 and 5 was associated with different weathering intensities under the influence of the strengthened East Asian Summer Monsoon (EASM) and with different weathering conditions according to the sediment source.

**Keywords:** Paleoclimate; East Asian Monsoon; terrigenous supply; major and trace elements.

## 1. Introduction

The South China Sea (SCS) is a tropical marginal basin influenced by the East Asian Monsoon System (EAM), one of the largest modern monsoon systems. The EAM significantly influences SCS surface and deep-water oceanographic patterns (i.e., hydrographic and hydrodynamic conditions, primary productivity, water column structure, and the composition and distribution of sediments) (Kienast, 2001; Oppo; Sun, 2005; Li et al., 2010; Liu et al., 2010). Modern EAM seasonal reversal occurs due to the Intertropical Convergence Zone (ITCZ) migration associated with the reversal of the warming capacity between the continent and ocean (Cheng et al., 2012). The resulting rainfall regime directly interferes with agricultural production in the most populous region of the planet that depends on subsistence agriculture, with an annual average rainfall of 280 mm (Cheng et al., 2012; Meng et al., 2021).

SCS sediments offer potential paleoclimate records of continent-ocean interactions and EAM intensity changes over time since it controls continental rainfall and drought regimes, resulting in weathering and erosion that determine terrigenous input to this basin (Liu et al., 2016). Furthermore, the SCS is under the influence of fluvial sedimentary contribution from some of the largest rivers in the world (Liu et al., 2016), highlighting the role of the marine records from the SCS for understanding the impacts on the continent and the ocean of such a complex climate system as EAM that operates globally. A diverse set of proxies may be applied to assess past terrigenous input. Natural gamma radiation (NGR) is widely used as a proxy for clay content and terrigenous vs. marine sediment input (Betzler et al., 2014; Vleeschouwer et al., 2017; Zhang et al., 2019). High NGR values correspond to clay-rich sediments while lower values indicate coarser or carbonate-rich material (Li et al., 2015c; Vleeschouwer et al., 2017; Zhang et al., 2019). In the northern SCS, Zhang et al. (2019) found NGR oscillations over the Quaternary, particularly after the Mid-Brunhes Event (MBE), related to pulses of coarser-grained sediments deposited (eroded) during glacial (interglacial) periods due to weaker (strengthened) East Asian Summer Monsoon (EASM). This highlights NGR as a good proxy for paleoclimatic reconstruction in SCS.

Source rock weathering and sediment transport processes can also be investigated through geochemical proxies such as major and trace elements (Boulay et al., 2005; Wei et al., 2006; Liu et al., 2009; Hoang et al., 2010; Liu et al., 2016). Bulk sediment elemental ratios have been applied in previous studies to unravel terrigenous input changes in the

SCS (Li et al., 2016; Liu et al., 2017). In the southern SCS sub-basin, Li et al. (2016), applied Ti/Ca ratios and reported increase in terrigenous contribution between 31 and 10 ka B.P. These authors attributed terrigenous input increase to enhanced EASM driven precipitation. Changes in the EASM is also attributed to chemical weathering intensity of terrigenous sediments that reached the northern SCS sub-basin since early Miocene (Wei et al., 2006). Besides erosion and weathering intensity, the geological characteristics of the source rock, and the transport agent of the detrital sediments also influence terrigenous supply to the SCS (Wei et al., 2006; Liu et al., 2016; Chen et al., 2017).

In the past few decades, the source-to-sink system in the SCS has been widely explored by the geochemical and mineralogical characterization of marine sediments from this marginal basin (Wei et al., 2006; Liu et al., 2016; Chen et al., 2017; Hu et al., 2021). However, the potential of deep SCS sediments in recording the depositional evolution has been poorly explored in contrast to the sediments from shallow waters deposited under the influence of sea-level low stands (Zhao et al., 2011; Jiwarungrueangkul et al., 2019; Xu et al., 2021). Considering the significant continental sedimentary contribution to the northern sub-basin of SCS (Liu et al., 2013b; Liu et al., 2016; Liu et al., 2017), this study aims to investigate the evolution of terrigenous input and the influence of EAM on the availability and flow of sediments, and its role in the dilution of marine biogenic carbonate in the last 230 kyr from elemental composition and NGR signal in a deep sedimentary record (Hole U1432C, 3839 m water depth) collected aboard the R/V Joides Resolution during IODP Expedition 349.

## 2. Study Area

The SCS is a semi-closed marginal basin located between Asia and the Pacific Ocean, with an area of 3.5 million km<sup>2</sup>, mainly characterized by its rhomboidal shape with a NE-SW oriented axis. The basin has a maximum depth of 5,500 m and an average depth of 1,140 m (Figure 2.1; Wang et al., 2014) and connects to the open ocean through north and south shallow channels. The deepest passage, the Luzon Strait (~2400 m depth) connects the SCS to the Pacific waters by the intrusion of the Kuroshio Current (Qu et al., 2006; Liu et al., 2011; Wang et al., 2014).

The modern SCS receives terrigenous sediments from some of the largest rivers in the world: the Pearl River and Red River, which flow into the northern portion of the basin. The southern portion of the SCS receives significant input of suspended sediment

(>450 x10<sup>6</sup> t/year) from Sumatra and Borneo, while in the north, the main contributors are Taiwan (176 x10<sup>6</sup> t/year) and southern China (102 x10<sup>6</sup> t/year) (Liu et al., 2016). Additionally, the Mekong River and the Luzon volcanic arc supply sediments to the SCS. Altogether, the SCS receives approximately 1600 Mt of sediments from the adjacent continents every year, distributed by surface and deep ocean circulation patterns (Liu et al., 2013b; Liu et al., 2016; Liu et al., 2017).

The SCS hydrodynamic regime is directly associated with the seasonal EAM changes, the Kuroshio Current (KC), and the Deepwater Current (DWC), especially in its northeastern portion (Liu et al., 2011; Liu et al., 2008; Zhou et al., 2017). A broad, cyclonic gyre characterizes surface hydrodynamics in winter, while during summer, a weak cyclonic gyre in the north and a strong anticyclonic gyre in the south are present (Liu et al., 2010). Deepwater dynamics are triggered by the entry of the DWC through the Luzon Strait, flowing in the northern part of the basin (Liu et al., 2013a) and influenced by the SCS boundary current and deep-range mesoscale eddies (Liu et al., 2016; Zhou et al., 2017).

### **3. Data and methods**

The sediments analyzed here were retrieved from the northeast sub-basin of the SCS during the IODP Expedition 349 onboard the R/V JOIDES Resolution with the aid of an advanced piston corer (APC). Approximately 10 cm<sup>3</sup> samples were collected at a sampling resolution of 20 cm over the uppermost sections 3H to 1H (between 23.23 mbsf and 0.62 mbsf) of Hole U1432C (18°21'N, 116°23'E, 3829 m water depth, 88.74 m sedimentary recovery).



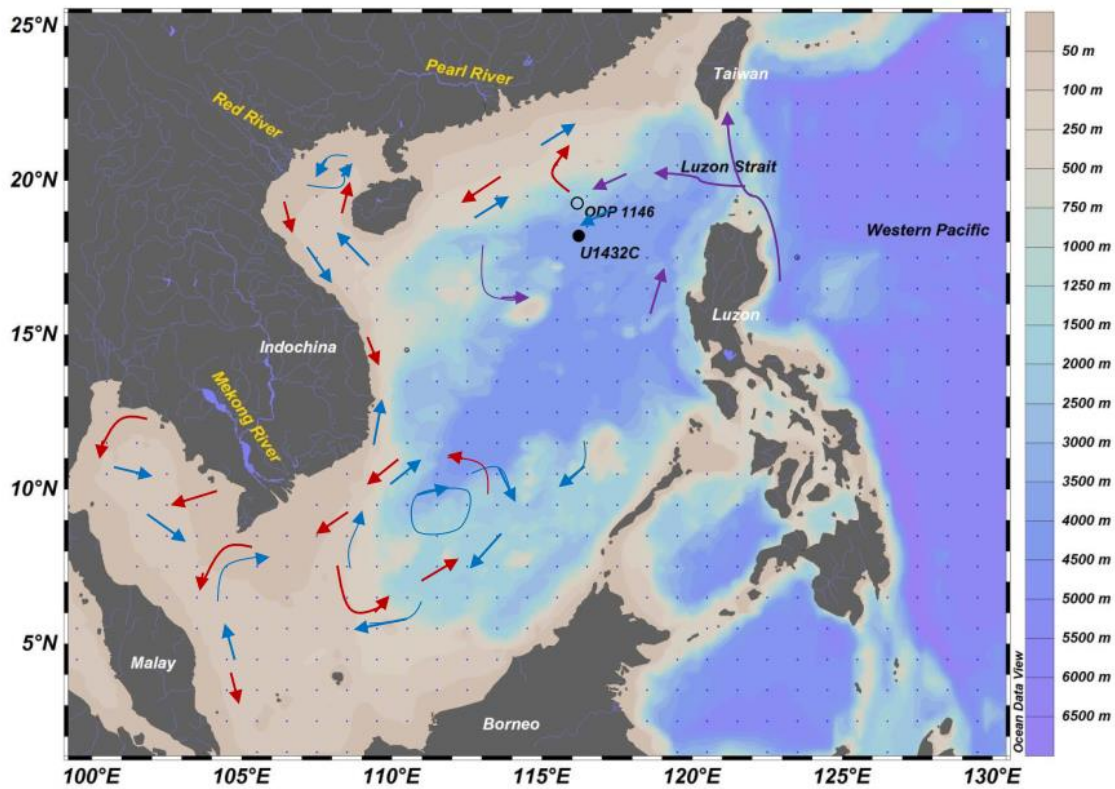


Figure 2.1. The South China Sea and Hole U1432C (black dot) and ODP 1146 (unfilled dot) retrieval sites location. The arrows depict schematic Kuroshio Current intrusion (purple), modern SCS surface winter (blue), and summer (red) circulation (based on Liu et al., 2016).

### 3.1 Core chronology

Chronology of the first 23 m of Hole U1432C was obtained using an excess  $^{230}\text{Th}$  method described by Ferreira et al. (2015). Excess  $^{230}\text{Th}$  ( $^{230}\text{Th}_{\text{xs}}$ ) values were used to estimate mean sedimentation rates ( $v$ ) (Eq. 1) and to establish an age-depth model (Eq. 2). The determination of  $^{230}\text{Th}$  and  $^{234}\text{U}$  activities was determined in 29 samples distributed along the first 23 m of Hole U1432C with a high-resolution gamma spectrometer (EG&G ORTEC, model 25190P), following analytical procedures described by Figueira (2000) and Ferreira (2014).

$$V = (\lambda \cdot D) / a \text{ (Eq. 1)}$$

$$I = z/v \text{ (Eq. 2)}$$

Equation 1 represents the sedimentation rate ( $v$ ) estimation in  $\text{cm kyr}^{-1}$ , considering  $^{230}\text{Th}$  ( $\lambda$ ) the constant decay, the core length in centimeters ( $D$ ), and the slope of the regression between  $\ln(^{230}\text{Th}_{\text{xs}})$  and the depth in centimeters ( $z$ ). The age of each

section is calculated in years (I) and determined according to equation 2, considering the section depth (z) and the sedimentation rate (v).

The chronology obtained from the  $^{230}\text{Th}_{\text{xs}}$  was compared to relative dates of biostratigraphy and magnetostratigraphy, obtained during Expedition 349 (Li et al., 2015c), for the polynomial adjustment of the data and refinement of the age model.

### 3.2 Natural Gamma Radiation (NGR)

We use NGR values obtained onboard on the whole-round core section using the Natural Gamma Radiation Logger (NGRL) published by Li et al. (2015). The NGRL measures the natural emission from the decay of  $^{238}\text{U}$ ,  $^{232}\text{Th}$ ,  $^{40}\text{K}$ , and their daughters, allowing to estimate the abundance of each of these isotopes according to their specific spectrum of emitted energy (Li et al., 2015c). The spectra were obtained from counting 5 minutes in each position, comprising 214 measurements between sections 3H-1H.

### 3.3 Major and trace elements composition

Trace and major elements in sediments were determined using microwave-assisted acid digestion, according USEPA method 3051A and SW-846 6010C (USEPA, 2007), at the Laboratory of Marine Inorganic Chemistry (LaQIMar-IO USP). Approximately 0.1 g of sediment from each sample was weighed and placed in Teflon® digester units. Then, 10 mL of concentrated nitric acid ( $\text{HNO}_3$ ) was added, and the units were placed in the microwave oven for 40 minutes. After 40 minutes, 3 mL of hydrofluoric acid (HF) was added, and the samples were placed in the microwave oven again for 40 minutes. Then 1.5 mL of hydrogen peroxide ( $\text{H}_2\text{O}_2$ ) samples were added, and the units were taken to the last cycle (40 minutes) in the microwave. After this process, samples were transferred from the digestion units to Teflon® beakers, using 5%  $\text{HNO}_3$ , and beakers were placed on a heating plate ( $150^\circ\text{C}$ ) until the sample volume was reduced to approximately 0.05 ml. The samples were diluted with 10 mL of 5%  $\text{HNO}_3$  and placed back on the hot plate upon reaching the reduced volume. At the end of the second evaporation, the beaker contents were filtered and transferred to 15 mL Falcon® tubes and made up with 5%  $\text{HNO}_3$ . Element quantification was performed using Inductively Coupled Plasma Optical Emission Spectrometry (ICP-OES, Varian brand, model 710-ES). Method validation was obtained by reading Certified Reference Material, SS2 (EnviroMAT Contaminated Soil, Supplementary Material 2.1 – Appendix C).

### 3.4 Data analysis

We evaluated the relative terrigenous influence and chemical weathering intensity at source rock location using the ratios Ti/Ca, and Al/K, respectively (Nesbitt; Wilson, 1992; Wei et al., 2003, 2006).

A correlation matrix and Principal Component Analysis (PCA) was performed in the PAST 3.25 software (Hammer et al., 2001) to identify the correlations and potential sources of major and trace elements of Hole U1432C sediments. The scores obtained from the PCA were plotted over time to characterize the composition of the sediments in response to paleoclimatic and paleoceanographic changes.

## 4. Results

### 4.1 Core description and chronology

Sediments from sections 3H-1H belong to Unit I (0 – 109.93 mbsf) of Hole U1432C are dominated by dark greenish gray clay and thin silt layers associated with distal turbidite deposits (Li et al., 2015c). According to the  $^{230}\text{Th}_{\text{xs}}$  chronology, Hole U1432C sediments comprise Pleistocene sediments between 230 ka (from MIS 7) to the Present. The  $^{230}\text{Th}_{\text{xs}}$  together with the  $\ln$  adjustment from the polynomial equation and biomagnetostratigraphic data (Table 2.1, Li et al., 2015c) provides sedimentation rates of  $10.52 \pm 0.34 \text{ cm kyr}^{-1}$  (Figure 2.2, Supplementary material 2.2 – Appendix D), showing no variation over the 3H-1H sections of the Hole U1432C.

Table 2.1. Biomagnetostratigraphic events recorded in the U1432C core (Li et al., 2015c) were used to construct the final polynomial. T = top/last appearance datum; B = base/first appearance datum, and age-based on  $^{230}\text{Th}_{\text{xs}}$  (ka).

Method	Event	Depth (m)	Age (ka)		
			Polynomial	$^{30}\text{Th}_{\text{xs}}$	Difference (%)
Planktonic foraminifera	T <i>Globigerinoides ruber</i> (pink)	14.10	120	134	10
	B <i>G. ruber</i> (pink)	46.01	400	437	8
Nanofossils	B <i>Emiliana huxleyi</i>	36.41	290	346	16
Paleomagnetism	Dated ash layer	32.00	230	304	24

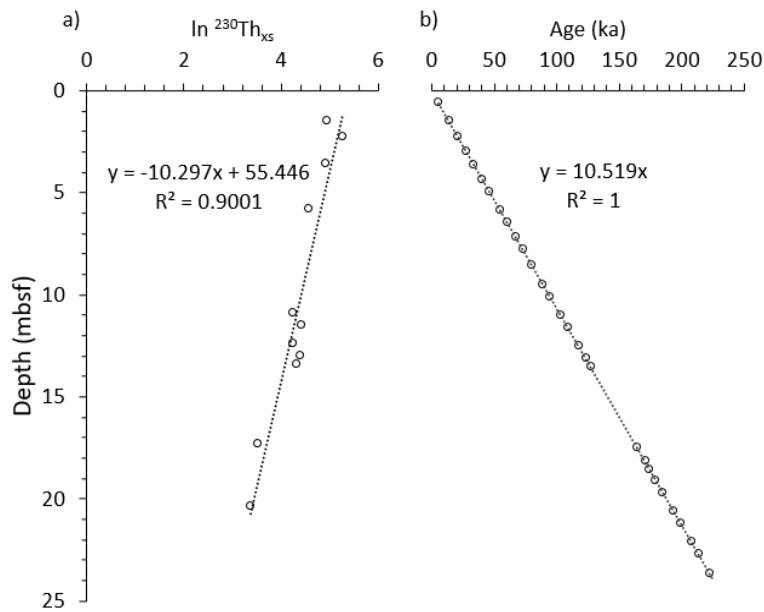


Figure 2.2. Hole U1432C (a) linearized and adjusted activity of excess  $^{230}\text{Th}$  ( $^{230}\text{Th}_{\text{xs}}$ ,  $\text{Bq g}^{-1}$ ), and (b) age model based on  $^{230}\text{Th}_{\text{xs}}$  (ka) obtained.

#### 4.2 Natural gamma radiation (NGR)

The NGR values ranged between 21 and 50  $\text{counts}\cdot\text{s}^{-1}$  (Figure 2.3a) with highest values during interglacial MIS 7 (40 and 50  $\text{counts}\cdot\text{s}^{-1}$ ) and MIS 5 (23 and 44  $\text{counts}\cdot\text{s}^{-1}$ ), and lower values at the beginning of MIS 6 (30 and 20  $\text{counts}\cdot\text{s}^{-1}$ ) and from MIS 4 to the Present, with around 20  $\text{counts}\cdot\text{s}^{-1}$ .

#### 4.3 Composition and distribution of major and trace elements

Hole U1432C sediments' elemental composition is dominated by Al, Fe, K, Mg, Ba, Ti, and Mn). Elements such as Cr, Cu, Ni, Sc, V, and Zn were also quantified in lower concentrations (Supplementary Material 2.3 – Appendix E). The correlation matrix shows a high correlation between the elements Al and Sc, Ba and Cu, Ca and Sr, Cr and Ti, Fe and K, and K and V within Hole U1432C (Table 2.2). Ti/Ca ratio presented values between 0.04 and 0.47, with higher values observed during MIS 5 and glacial-interglacial transitions (Figure 2.3b). The elemental ratio Al/K varied between 1.26 and 3.23, with lower Al/K values recorded during MIS 7, averaging 2.31, and higher values from MIS 5 towards the Present, with an average of 2.61 (Figure 2.3f).

Table 2.2. Correlation matrix (Pearson coefficient) of the composition of the elements of Hole U1432C. Values in bold correspond to significant correlations.

	Al	Ba	Ca	Cr	Cu	Fe	K	Mg	Mn	Ni	Sc	Sr	Ti	V
Ba	0.69													
Ca	0.10	0.35												
Cr	0.42	0.35	-0.25											
Cu	0.45	<b>0.83</b>	0.43	0.26										
Fe	0.53	0.53	-0.10	0.79	0.41									
K	0.71	0.58	-0.12	<b>0.85</b>	0.40	<b>0.91</b>								
Mg	0.25	0.02	0.17	-0.02	-0.08	0.01	0.10							
Mn	0.26	0.40	-0.06	0.33	0.32	0.60	0.41	0.05						
Ni	0.52	0.80	0.38	0.23	0.77	0.46	0.41	-0.19	0.50					
Sc	<b>0.91</b>	0.63	0.07	0.25	0.36	0.31	0.52	0.29	0.12	0.43				
Sr	0.38	0.70	<b>0.87</b>	-0.11	0.62	0.04	0.09	0.16	0.08	0.59	0.38			
Ti	0.44	0.20	-0.29	<b>0.87</b>	0.04	0.77	<b>0.84</b>	0.03	0.30	0.16	0.23	-0.20		
V	0.56	0.65	-0.03	<b>0.86</b>	0.63	0.81	<b>0.87</b>	-0.06	0.36	0.56	0.42	0.18	0.72	
Zn	0.32	0.66	0.39	0.29	0.66	0.47	0.43	-0.18	0.32	0.65	0.22	0.54	0.15	0.51

The PCA revealed that three factors (PC1, PC2, and PC3) explain 78.35% of the variance from our data (Table 2.3). PC1 is positively correlated ( $r > 0.7$ ) to all analyzed elements, with higher Al, Ba, Cr, Cu, Fe, K, Ni, Ti, V, and Zn values. PC2 shows a strong positive correlation with Ca and Sr elements, while PC3 displays a strong and positive correlation with Al, Mg, and Sc. PC3, composed of Al, Mg, and Sc, with Al and Sc strongly correlated ( $r = 0.91$ ). Along the core distribution, the PC1 scores shows prevailing negative values during interglacial periods (MIS 7, 5, and 3) and positive values at the beginning of MIS 6 and during MIS 4 and 2 (Figure 2.3c). PC2 scores show negative values between MIS 7 and 5, with lower values recorded throughout MIS 5 and positive values from MIS 4 to the Present (Figure 2.3e). On the other hand, PC3 scores vary between positive and negative values through MIS 7, 6, and 5, with low but mostly positive values after MIS 4 (Figure 2.3g).

Table 2.3. Variance and loadings of factors 1, 2, and 3 from the principal component analysis (correlation matrix) for the Hole U1432C element composition data. The scores above 0.3 are represented in bold.

	Principal Component Extraction (Correlation)		
	1	2	3
Eigenvalue	6.88	3.25	1.62
% variance	45.84	21.68	10.83

Al	<b>0.30</b>	0.01	<b>0.41</b>
Ba	<b>0.33</b>	0.21	0.01
Ca	0.07	<b>0.45</b>	0.02
Cr	0.27	-0.33	-0.06
Cu	0.28	0.26	-0.18
Fe	<b>0.32</b>	-0.23	-0.11
K	<b>0.33</b>	-0.23	0.09
Mg	0.02	0.02	<b>0.60</b>
Mn	0.20	-0.06	-0.19
Ni	0.29	0.23	-0.19
Sc	0.24	0.07	<b>0.50</b>
Sr	0.17	<b>0.45</b>	0.08
Ti	0.23	-0.38	0.03
V	<b>0.34</b>	-0.15	-0.10
Zn	0.26	0.19	-0.29

## 5. Discussion

Continental rocks and marine biogenic activity are the primary sources of marine sediments particles. The site location and depth of Hole U1432C retrieval favor terrigenous sediments deposition and preservation in the geological record. The elemental composition of Hole U1432C suggests a predominantly terrigenous origin (i.e., Al, Fe, K, Mg, Ba, Ti, and Mn), with a small biogenic contribution of the sediments that reached the northeast SCS sub-basin over the last 230 kyr. The NGR signal, elemental ratios, and PCA results highlight the importance of continentally derived sediments to Hole U1432C retrieval site and its close relationship to weathering conditions over the continent with increased terrigenous contribution during MIS 5. PC1 and PC3 were correlated to elements composing continental sourced sediments (Table 2.3), while PC1 correlates to elements enriched especially during leaching processes, such as K, Ti, Mn, and chemical weathering, such as Al, Fe, and Sc (Nesbitt; Wilson, 1992; Wei et al., 2003, 2004). The variations in Ti/Ca ratio and NGR signal corroborate the pattern reflected by PC1 during MIS 5, indicating a more significant contribution from clastic sediments. PC3 is strongly correlated to elements (Al, Mg, and Sc) predominantly more resistant to leaching and associated with more intense chemical weathering (Teng, 2017; Wei et al., 2003), which explains its similarity to Al/K ratios (Figure 2.3f). In contrast, PC2 is strongly correlated with Ca and Sr elements, reflecting biogenic sediments input. Since, at the northeast sub-basin of the SCS, the authigenic contribution of minerals usually associated with terrestrial materials is negligible (Wei et al., 2003; Zhang et al., 2015), our elemental

composition results changes are interpreted primarily as variations in the input of sediments derived from the adjacent continent and marine biogenic contribution.

### 5.1 Late Quaternary terrigenous input to the northeast SCS: controlling factors

Changes in the Quaternary terrigenous input for the SCS have been attributed to several factors, such as variations in the EAM intensity, sea-level fluctuations, and changes in the tectonic settings (Liu et al., 2016, 2017; Zhao et al., 2017; Chen et al., 2017; Hoang et al., 2010; Liu et al., 2009). At the northeast sub-basin, shelf sediments are more susceptible to sea-level changes driven processes, such as post-depositional reworking (Liu et al., 2016; 2017; Zhao et al., 2017), while deeper sediments better reflect the influence of the EAM intensity changes on the precipitation regime and consequently, fluvial sediment input (Hu et al., 2012; Chen et al., 2017; Clift et al., 2014; Hoang et al., 2010; Liu et al., 2009).

Additionally, the intense precipitation resulting from the EASM favors erosion, leaching, and weathering the adjacent to the SCS continental regions (Wei et al., 2003, 2004; Gurumurthy et al., 2014; Bastian et al., 2017). Wet and warm periods of strengthened EASM result in intensified leaching and weathering and, therefore, more significant fluvial input, while drier periods are associated with a decrease in these processes (Wei et al., 2006). In this context, NGR is an excellent proxy to assess both terrigenous contribution and EASM dynamics as intensified weathering promoted by strengthened EASM will result in higher clay contents and, thus, higher NGR (Li et al., 2016; Zhang et al., 2019). Previous works argue that higher concentrations of elements such as Al, K, Mg, Fe, Mn, Sc, V, Co, Cr, and Zn in the sediments deposited at the northern sub-basin of SCS were a result of increased precipitation triggered by a strengthened EASM in the interglacial periods of the last 200 kyr (Wei et al., 2004). Wei et al. (2006) verified, through elementary ratios sensitive to chemical weathering, changes in the EAM intensity in the last 2.5 Ma in a sedimentary record of the northern SCS. According to these authors, variations in the content of Ti, Al, Na, and K were sensitive to changes in the intensity of chemical weathering in the source regions of these sediments.

Here Ti/Ca and NGR were applied to assess changes in terrigenous supply. Increased Ti/Ca ratio and NGR revealed a higher terrigenous contribution during MIS 7 and 5. The relative dilution of marine biogenic sediment by enhanced clastic contribution

observed in Ti/Ca ratios is consistent with the decrease of planktonic foraminifera abundance observed in Hole U1432C (Figure 2.3d, Nagai; Gerotto, 2019). In contrast, an opposite behavior is observed when NGR and planktonic foraminifera abundance are compared, highlighting the significant terrestrial input during MIS 7 and 5.

An enhanced coarser influx in marine sediments during interglacials is expected once continental erosion is pronounced in response to the glacial-interglacial transition of monsoon climate systems (Zhang et al., 2001; Hoang et al., 2010; Liu et al., 2017). PC1 and PC3 positively correlate to terrigenous input and leaching and chemical weathering of source rocks, with PC3 reflecting a higher degree of chemical weathering, and the comparison of their along Hole U1432C variation provides clues to the EASM intensity history. The positive variations of PC3 in Hole U1432C during MIS 7, 6, and 5 are associated with moderate to extreme chemical weathering intensity, as it is predominantly composed of more resistant elements (Middelburg et al., 1988; Nesbitt; Wilson, 1992). In addition to this, the enriched conservative elements such as Al, Fe, and Ti indicate moderate to extensive chemical weathering (Nesbitt; Wilson, 1992). While during MIS 5, the positive variations of PC1 reflect a more significant contribution of leached and weathering products, indicating the influence of the strengthened EASM during this stage (Figure 3c,i). The enhanced chemical weathering during MIS 5, when compared to MIS 7, is corroborated by the Al/K ratio trends.

However, the increasing Al/K ratio values from MIS 5 to the present are not fully accompanied by PC3 values or other proxies, suggesting that since MIS 5, sediments reach the Hole U1432C site may have had a different source rock rather than be a result of increased chemical weathering.



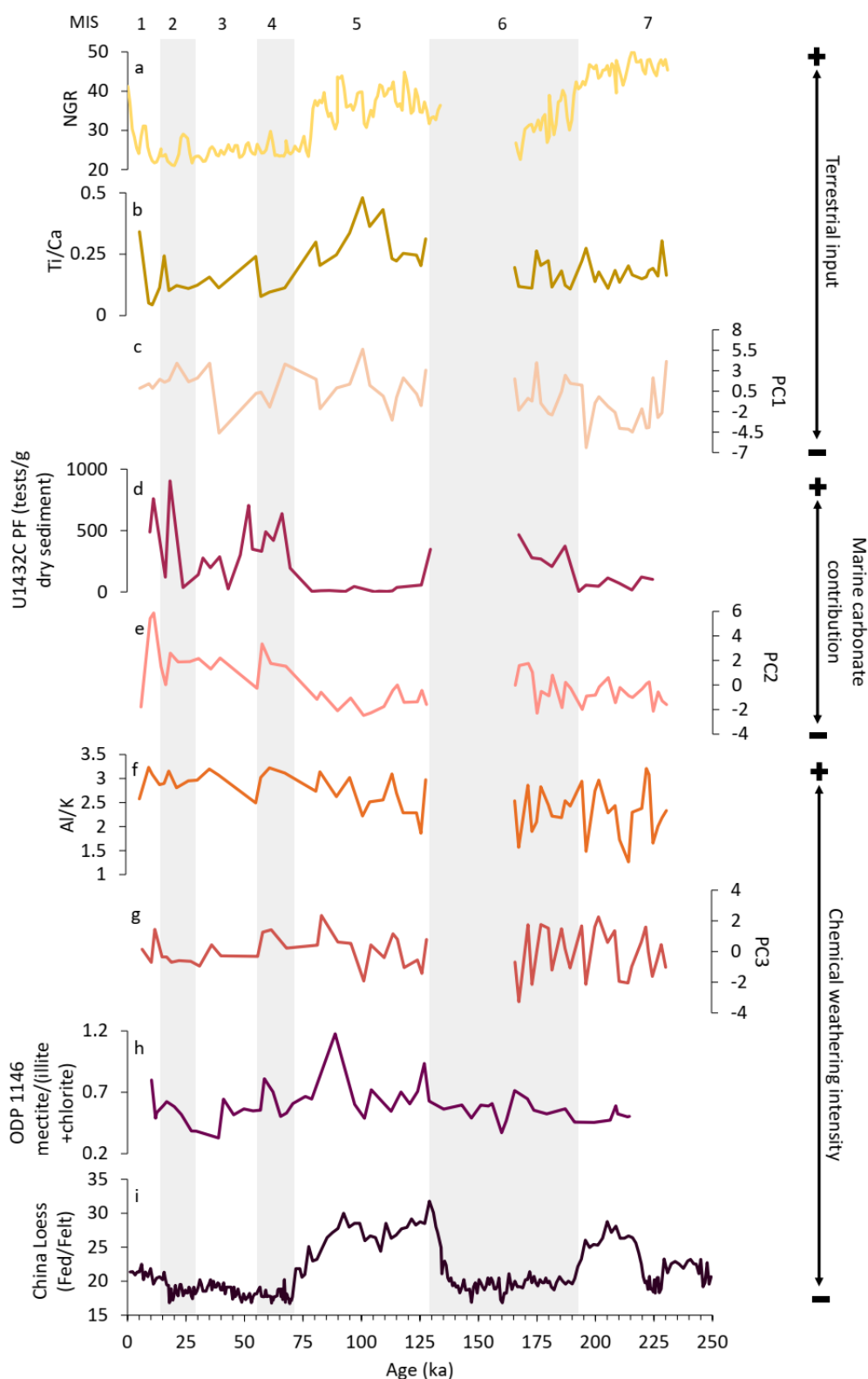


Figure 2.3. Proxies for terrestrial input (a, b, c), marine carbonate contribution (d, e), and chemical weathering intensity (f, g, h, i) were obtained from Hole U1432C and records from northeastern SCS sub-basin and China continental loess. (a) Natural gamma radiation values in counts  $\cdot$   $^{-1}$ , (b) Ti/Ca elemental ratio and (c) scores of principal component 1 (this study); (d) Planktonic foraminifera (PF) abundance from Hole U1432C

(Nagai; Gerotto, 2018) and (e) scores of principal component 2 (this study); (f) Al/K elemental ratio and (g) scores of principal component 3 (this study); (h) ODP 1146 smectite/(illite+chlorite) ratio (Liu et al., 2003) and (i) Chinese Fed/Fet loess record (Guo et al., 2008).

## 5.2 SCS NE sub-basin potential sediment sources

The SCS surface sediments distribution, geochemical and mineralogical characteristics are directly related to the drainage systems on the adjacent continent and with the hydrodynamics of this marginal basin (Liu et al., 2016).

Northeastern SCS sub-basin sediment sources are mainly related to the Pearl River, Luzon, and Taiwan drainage basins (Liu et al., 2016). The geological characteristics of each continental region and climate conditions provide different weathering levels (Liu et al., 2016; Chen et al., 2017). According to these authors, a long-term combination of a hot and humid tropical climate with a relatively stable tectonic configuration results in intense chemical weathering, with relatively weak physical erosion, at the Pearl River drainage basin. In contrast, at Luzon drainage basins, the predominance of volcanic rocks and subtropical climatic conditions favor rapid physical weathering rather than chemical weathering. The Taiwan and Indochina drainage basins present an intense reworking of sedimentary and metamorphic bedrocks because of isostatic changes, combined with a warm and humid subtropical climate resulting in moderate chemical weathering (Liu et al., 2016; Chen et al., 2017). In this context, terrigenous input in Hole U1432C sediments may reflect a mixture of different source rock areas that provide sediments with different geochemical weathering intensities.

High terrestrial contribution during MIS 7 and 5 reflected by NGR and Ti/Ca are consistent with enhanced weathering under strengthened EASM, while Al/K reflected different chemical weathering intensities between these interglacials. These results are consistent with intensified chemical weathering in northern SCS related to the EASM recorded by higher smectite/(illite+chlorite) ratio during MIS 5 (Figure 3h, Chen et al., 2017). The smectite content in the modern and Late Quaternary SCS is highly related to Luzon's contribution, while illite and chlorite are associated with sediments from Pearl, Red, and Mekong rivers, Taiwan, and Borneo drainage areas (Liu et al., 2007ab; Liu et al., 2008; Chen et al., 2017). Variations in the intensity of chemical weathering between MIS 7 and 5 may be linked to different processes by which the monsoon acts on the continent and the sediments' availability. Chen et al. (2017) observed a significant

influence of EASM on Luzon Island volcanic rocks' rapid chemical weathering in the SCS northeast sub-basin. At the same time, the supply of sediments by the Pearl River reflects the greater intensity of physical weathering, although both are associated with wetter and warmer periods (Chen et al., 2017).

Therefore, although the terrigenous input during MIS 7 and 5 in the Hole U1432C is related to enhanced EASM, the source of these sediments may reflect different predominant processes determining the intensity of the terrigenous contribution and its composition, which explains the decreased Al/K during MIS 7 in contrast to MIS 5, which may indicate different intensities or processes in the availability of terrigenous sediments. As the lithology from Luzon is mainly composed of basaltic rocks under the influence of an active tectonic and intense monsoon rainfall, it favors the occurrence of smectite over others (Figure 3h; Boulay et al., 2005; Liu et al., 2009; Chen et al. 2017). In this sense, higher terrigenous supply during MIS 5 in Hole U1432C reflected the increased detrital contribution from Luzon under the influence of strengthened EASM.

### 5.3 What controlled late Quaternary biogenic particle preservation at the northeast SCS deep-sea?

The contribution of biogenic particles to deep-sea sediments at the SCS is mainly controlled by the dilution of biogenic particles by terrigenous input, carbonate saturation thresholds (dissolution), or biogenic flux (Thunell et al., 1992; Chen et al., 1999; Li et al., 2001; Wei et al., 2003; Zhang et al., 2015). The modern northeast SCS sub-basin surface sediments present CaCO<sub>3</sub> values between 0 and 10%, configuring one of the SCS regions with the lowest carbonate concentration (Zhang et al., 2015). At Hole U1432C retrieval site and depth (3829 m), biogenic particles' contribution to modern sediments is primarily controlled by dilution and dissolution inherent to below lysocline and CCD depths (Zhang et al., 2015).

The low PC2 scores during MIS 7 and 6 suggest that biogenic particles composed a small part of the sediments. During MIS 5, PC2 scores decrease, reaching the lowest values in the record. This low biogenic contribution is followed by an increase in PC2 scores from MIS 4 towards the Present. Low PC2 scores observed during MIS 7 to 5 are also accompanied by relatively high terrigenous input, as shown by PC1 and PC3 scores, while since MIS4, our data suggest a decrease in terrigenous input. Therefore, PC2

changes seem to reflect the dilution effect driven by changes in terrigenous input to the northeast SCS sub-basin.

However, the role of dissolution influence over carbonate preservation of Hole U1432C sediments, mainly because of its' below the lysocline retrieval depth, cannot be overlooked. We focus on Ca and Sr concentrations and planktonic foraminifera density distribution along with our record to explore this. In marine sediments, Ca and Sr concentrations are related to biogenic particles, as these elements compose carbonates (i.e.,  $\text{CaCO}_3$  and  $\text{SrCO}_3$ ). As with Ca, Sr concentration in marine sediments is also determined by the lysocline threshold (Villiers, 1999; Liu et al., 2020), with the biogenic Sr made available mainly from aragonite dissolution, one of the three anhydrous crystalline polymorphs of  $\text{CaCO}_3$  (Liu et al., 2020; Ruiz-Hernandez et al., 2010).

Along the Quaternary, low  $\text{CaCO}_3$  contents and Ca and Sr concentrations observed in records retrieved above and below the lysocline have been attributed to dissolution (Wang et al., 2014; Wei et al., 2004; Liu et al., 2020). Hole U1432C Ca concentrations range between 6371.34  $\text{mg.kg}^{-1}$  and 45165.8  $\text{mg.kg}^{-1}$ , and Sr concentrations, between 50 and 140  $\text{mg.kg}^{-1}$ , over the last 230 kyr, Wei et al. (2004), however, reported Sr concentration values between 150 and 400  $\text{mg.kg}^{-1}$  from above the lysocline record (ODP 1144, 2037 m water depth) in the northeast SCS sub-basin. Our below the lysocline lower Sr concentrations compared to those of ODP 1144 corroborate a carbonate dissolution influence on carbonate preservation in deep-sea sediments of the northeast SCS sub-basin. It is worth to note the relatively low Ca and Sr concentrations observed at Hole U1432C sediments during MIS 5 (6371  $\text{mg.kg}^{-1}$  and 71  $\text{mg.kg}^{-1}$ ) (Supplementary Material 2.3), which is also characterized by samples with very low to baren in planktonic foraminifera abundances (Figure 3d). Therefore, our carbonate-related proxies suggest that the Hole U1432C site has been below the lysocline over the last 230 kyr. These proxies also suggest that, particularly during MIS 7 and 5, carbonate dilution influenced carbonate contribution at deep sediments from the northeastern SCS sub-basin.

## 6. Conclusion

Here we reported the NGR intensity, elemental ratios, concentration, and distribution of trace and major elements (Al, Ba, Ca, Cr, Cu, Fe, K, Mg, Mn, Ni, Sc, Sr, Ti, V, and Zn) from deep northern SCS sediments. Our data shows changes in terrigenous

input in the SCS northeast sub-basin over the last 230 kyr controlled by the EASM regime, intensifying rainfall, and the degree of weathering and erosion during MIS 7 and 5. Both interglacial periods were characterized by higher terrigenous input triggered by high rainfall promoted by a stronger summer monsoon. However, a more significant terrigenous contribution of sediments potentially Luzon sourced in response to intense chemical weathering was recorded during MIS 5, resulting in dilution of biogenic components during the same period. The difference in the contribution of terrigenous elements from chemical weathering during MIS 7 and MIS 5 may be associated with the source of these sediments, less or more susceptible, respectively, to the rapid erosion, chemical weathering, and leaching process caused by the strengthened EASM. Hole U1432C data highlights the deep sediments of the northeast sub-basin of the SCS as a potential tool to understand paleoclimatic variations in the intensity of the EASM acting over continental leaching and weathering in the last 230 kyr.

### **Acknowledgments**

This research used samples and data provided by the International Ocean Discovery Program (IODP). We thank you the science party members, crew, and technicians aboard the R/V JOIDES Resolution for their work during IODP Expedition 349. Funding was provided by IODP/CAPES-Brasil (Edital 38/2014), Fundação de Amparo à Pesquisa do Estado de São Paulo (FAPESP; Proc. n°.2015/11832-2) and Coordenação de Aperfeiçoamento de Pessoal de Nível Superior – Brasil (CAPES) - Finance Code 001.

### CHAPTER III

#### Dissolution effects on coccoliths morphology and its implications for paleoceanographic studies - a case study from the South China Sea

Manuscript in preparation for submission to the Journal of Geophysical Research: Biogeosciences. This manuscript is co-authored by Iván Hernandez-Almeida, Hongrui Zhang, Heather Stoll, Chuanlian Liu, Rubens César Lopes Figueira and Renata Hanae Nagai

#### Abstract

Marine calcifiers tests are widely used as past ocean carbonate chemistry proxies. However, the complexity of the carbonate system and organisms' ecological aspects limit proxy robustness. Here we present a new dissolution proxy based on the morphological attributes of coccolithophores from Noelaerhabdaceae family (*Emiliana huxleyi* and *Gephyrocapsa* spp, > 2  $\mu\text{m}$ ). Coccoliths morphological attributes changes were evaluated by a dissolution experiment using different amounts of Calgon solution. The degree of preservation was evaluated through mass, volume, length, thickness, and ks shape factor measurements under a circularly polarized light microscope. The mean ks reflected different degrees of dissolution and size-selective dissolution (small coccoliths are preferentially dissolved) that affect assemblage composition. These findings were compared to morphological attributes data from twenty-eight (N = 28) surface sediments retrieved from the SCS along a depth gradient (629 – 3809 m) during the R/V Sonne cruises (SO-95). Morphological attributes and surface samples site locations environmental data at 50 m depth (mean annual seawater temperature, salinity, nutrients, total alkalinity, total carbon dioxide, pH, and calcium carbonate saturation ( $\Omega_{\text{Ca}}$ ) at bottom depth) potential relationships were assessed with a redundancy analysis (RDA). RDA results presented samples mainly distributed along the first axis (RDA1) which explained 54.65% of the total variation. The RDA1 was highly correlated with the  $\Omega_{\text{Ca}}$  at depth ( $R = 0.62$ ). The mean ks was the morphological attribute better suited to explain our dataset, and highly correlated with the  $\Omega_{\text{Ca}}$  ( $R^2 = 0.47$ ). The surface sediment results showed that the mean ks from fossil coccolithophore assemblages were mainly controlled by changes in carbonate saturation affecting post-burial coccolith preservation, enabling

its use for the quantitative reconstruction of past carbonate dissolution changes. We applied the mean  $k_s$  from Noelaerhabdaceae coccoliths as a dissolution proxy at ODP 1146 from northern SCS. The mean  $k_s$  recorded glacial-interglacial changes in carbonate preservation over the last 210 kyr in line with changes in deep-water circulation between Pacific and SCS. The less ventilated and enhanced stratification of SCS waters resulted in a shallower lysocline and strengthened  $\text{CaCO}_3$  dissolution during the glacial stages and LGM. Our results demonstrate that the mean  $k_s$  can be potentially applied as a dissolution proxy to track changes in the carbonate saturation state. We showed that post-burial dissolution effects have an important influence on coccolithophore fossil assemblages from SCS.

**Keywords:** Coccolith morphology. Coccolith dissolution. Circularly polarized light. Carbonate saturation state.

## 1. Introduction

The large reservoir capacity of carbon dioxide ( $\text{CO}_2$ ) of the oceans plays an important role in the carbon cycle and, consequently, in controlling atmospheric  $\text{CO}_2$  (Ridgwell; Zeebe, 2005; Wang et al., 2016). When  $\text{CO}_2$  dissolves in water, pH and carbonate ion concentration decrease, making the ocean more acidic and lowering carbonate saturation ( $\Omega_{\text{Ca}}$ ). The carbonate compensation depth (CCD) is often defined as the depth at which ocean is undersaturated in calcite (Ridgwell; Zeebe, 2005). The near-surface seawaters appear to be supersaturated with calcite according to the depth of the lysocline, the limit at which calcite dissolution effects starts (Ridgwell; Zeebe, 2005). In contrast large parts of the world's ocean are currently undersaturated because of the increasing solubility of calcite with pressure (Sulpis et al., 2018). As the ocean absorbs larger amounts of  $\text{CO}_2$ , for example as the result of the anthropogenic fuel emissions, the carbonate compensation depth shoals (Sulpis et al 2018). Variations in the CCD on timescales of hundreds to Myrs are therefore an important process in determining the carbonate chemistry of the ocean and in the regulation of  $\text{CO}_2$  in the atmosphere (Emerson; Archer, 1990).

The net flux of  $\text{CO}_2$  at the ocean-atmosphere interface depends on  $\text{CO}_2$  solubility, wind intensity, and  $\text{CO}_2$  partial pressure ( $p\text{CO}_2$ ), given by the difference between  $p\text{CO}_2$  in the atmosphere and at the ocean surface, thus determining the behavior of the ocean as

a CO<sub>2</sub> sink or source for the atmosphere (Sarmiento; Gruber, 2006; Libes, 2009). The ocean pCO<sub>2</sub> is influenced by temperature, salinity, and biological activity, including primary production, respiration, calcification, and carbonate dissolution (Ridgwell; Zeebe, 2005; Sarmiento and Gruber, 2006; Libes, 2009; Wang et al., 2016). Faced with a scenario of increased anthropogenic CO<sub>2</sub> emissions, a halving of carbonate saturation level is expected because of the decreasing pH predicted for the next 100 years (Hönisch et al., 2012; USGCRP, 2017; IPCC, 2019). Understanding the variations in the physical and biogeochemical parameters that control the CO<sub>2</sub> flux within the Earth's natural variability is critical in elucidating the role of the oceans in balancing the global carbon cycle.

The role of marginal oceans in biogeochemical cycles has been widely explored, given their potential to record amplified signals of these changes (Liu et al., 2010; Dai et al., 2013). In the modern northern South China Sea (SCS) surface waters, for example, a 14% decrease of the calcite saturation level has already been observed in response to the influence of anthropogenic CO<sub>2</sub> (Chou et al., 2007). These conditions varied over time according to our planet's climate cycles and internal feedbacks (Resplandy et al., 2015). Within this context, the South China Sea (SCS) stands out as a region of great interest for paleoceanographic reconstructions given its location of fundamental importance in climate regulation, as it acts as an active channel of communication between high and low latitudes (Yu; Chen, 2013). In addition, the SCS is under the influence of the seasonal wind reversal of the East Asian Monsoon System (EAM), which, similarly to tropical oceans, allows through its circulation and connection with the global monsoon system, high and low latitudes atmospheric communication (McClymont et al., 2013; Yu; Chen, 2013). The EAM influence directing the SCS's climatic and oceanographic processes also highlights the region as an important place for unraveling ocean-atmosphere dynamics, such as the CO<sub>2</sub> flow.

The influence of ocean acidification and the effects of carbonate chemistry changes in the geological past have been investigated from isotopic tools such as variations of  $\delta^{13}\text{C}$  and B/Ca ratio from benthic and planktonic foraminifera, in addition to the CaCO<sub>3</sub> content in marine sediments (Hönisch et al., 2012; Wan et al., 2018; 2020). Although  $\delta^{13}\text{C}$  and B/Ca are reliable proxies for CO<sub>2</sub> reconstructions and quantifying pH in the past, both are driven by other carbonate chemistry parameters that impose some limits on the interpretation of both proxies (Hönisch et al., 2012; Rae et al., 2021).



Additionally, proxies based on the assessment of marine calcifiers, including the  $\text{CaCO}_3$  content and fragmentation indices, used to infer dissolution conditions in the oceans in the past, have limitations related to the biological mechanisms of each species that will determine the calcification and preservation responses (Hönisch et al., 2012; Rae et al., 2021). The physiological mechanisms of the species used in these reconstructions must be considered to distinguish whether the assemblages are reflecting changes in the calcification process during their life cycle or post-depositional changes (Hönisch et al., 2012; Rae et al., 2021). Thus, despite the reliability of the mentioned proxies, the calibration of the species used, and the environmental parameters evaluated are essential to refine and improve the interpretations of the past geological records. Furthermore, the reconstruction of other parameters of the carbonate system provides a broader view of this complex system. The saturation state of calcite is a good candidate to improve our understanding of CCD variations and plays an important role in ocean alkalinity variations promoted by precipitation and dissolution of  $\text{CaCO}_3$  (Rae et al., 2021). Coccolithophores, a group of marine calcareous phytoplankton, are especially sensitive to changes in carbonate chemistry (Iglesias-Rodriguez, 2008). The composition and thickness of coccoliths, can reflect changes in dissolved  $\text{CO}_2$  concentration in the ocean, pH, temperature (Rickaby et al., 2007; Beaufort et al., 2011; Bolton et al., 2016; Rigual-Hernández et al., 2020). This phytoplankton group is the main constituent of marine biogenic sediments, as they contribute up to 80% to deep-sea carbonate fluxes (Young; Ziveri, 2000). In addition to being abundant in sediments and offering high-resolution records, the investigation of changes in the calcification pattern in coccoliths from the Eastern Equatorial Pacific showed the role of the biological pump in the  $\text{CO}_2$  sequestration from the atmosphere from glacial to Holocene (Balestrieri et al., 2021). Dissolution and preservation indexes from *Gephyrocapsa* spp. from the East China Sea revealed its potential to trace changes in CCD position (Jin et al., 2019). Su et al. (2020) reported from geologic coccolith weight records in the SCS a significant role of ocean carbonate chemistry and nutrient concentration in the calcification, strongly correlated to regional oceanographic settings over the last 200 kyr. These studies highlight the complexity of the carbonate system, driven by several carbonate chemistry parameters, post-depositional changes, and regional hydrographic effects, for example.

In this study we present a new dissolution proxy based on morphological attributes from fossil coccolithophores in surface sediments in the SCS. In addition, we evaluated

the morphological variations of coccoliths under different dissolution degrees in a laboratory experiment. Using an automated algorithm to estimate coccolithophore calcification from images taken with a microscope under cross-polarization, we show that the elliptical-ks (describe) from coccolithophores located along a depth gradient in the SCS are highly correlated to the calcite saturation state of the deep-ocean, enabling the quantitative reconstruction of changes in the CCD in the past.

## **2. Oceanographic settings**

The SCS is a marginal basin located in the Western Pacific, connected to the open ocean by north and south shallow passages (Figure 3.1A). The Luzon Strait in the north is the deepest (~2000 m) and principal channel for water exchanges between the SCS and the Pacific through the Kuroshio Current (Qu et al., 2006; Liu et al., 2011; Wang; Jian, 2014). The modern surface circulation and hydrographic characteristics of the SCS are directly associated with the seasonal changes promoted by the EAM. These seasonal hydrodynamic patterns result in contrasting regional distribution of sea surface temperature (SST), salinity, and nutrients (Figure 3.1B-E, Wang; Li, 2009). The SST latitudinal gradient is up to 2°C with an annual temperature average of 28-29°C in the southern SCS and 26-27°C in the north (Tian et al., 2010). Salinity varies between 32.8-34.2, with smaller salinity variation in the north than in the south (Wang; Li, 2009). Northern SCS primary productivity reflects the seasonality of the EAM with more productive and well-mixed waters during the winter season, with higher chlorophyll-*a* concentration (0.65 mg Chl- $\alpha$  m<sup>-3</sup> and 600 mg C m<sup>-2</sup> d<sup>-1</sup>) (Chen, 2005; Chen et al., 2006; Jin et al., 2016).

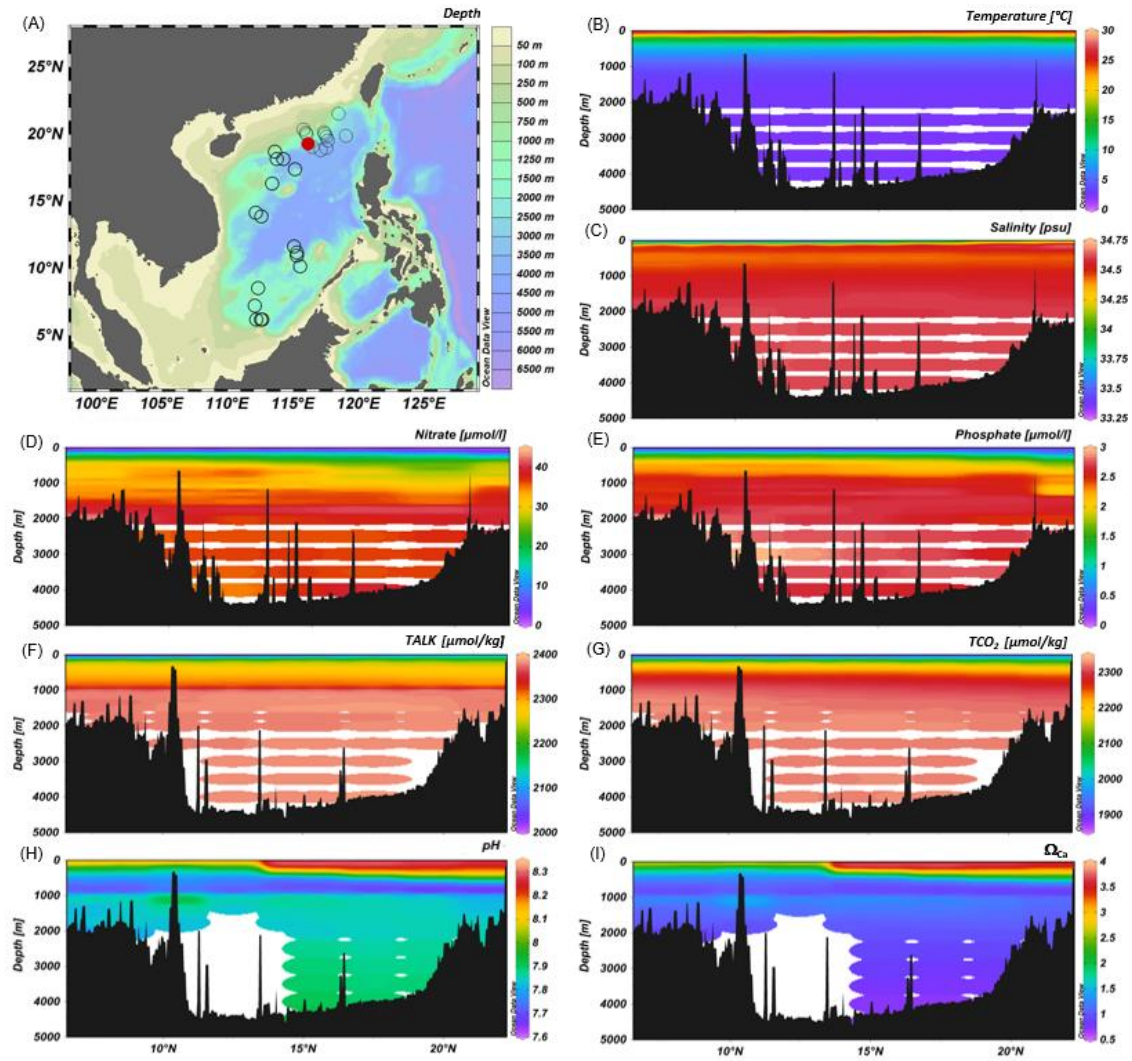


Figure 3.1. Map of the South China Sea and location of core-top samples (unfilled dots) and ODP1146 (red dot) used in the present study (A). Vertical profiles along N-S ( $5^\circ$  to  $22^\circ$  N) transect of (B) temperature, (C) salinity, (D) nitrate and (E) phosphate obtained from World Ocean Atlas 2001 (WOA01, Conkright et al., 2002), (F) total alkalinity (TALK) and (G) total dissolved inorganic  $\text{CO}_2$  from Goyet et al. (2000), (H) pH and (I)  $\Omega_{\text{Ca}}$  calculated at  $\text{CO}_2\text{SYS}$  (Pierrot et al., 2012) from previous extracted data (Goyet et al., 2000).

The modern SCS lysocline is located at approximately 3000 m and the CCD lies between 3500 and 3800 m (Thunell et al., 1992; Wang et al., 1995; Regenberget al., 2014). Carbonate chemistry parameters of northern SCS are characterized by relatively lower DIC and TALK (Figure 3.1F-G) and higher pH and  $\Omega_{\text{Ca}}$  in the first 300 m (Figure 3.1H-I) (Chou et al., 2007; Jin et al., 2016). Below 1000 m the SCS oceanographic chemical parameters are relatively low in the N-S transect with roughly constants DIC,  $\delta^{13}\text{C}$ , and  $[\text{CO}_3^{2-}]$  defined as well ventilated deep waters (Chen et al., 2006; Qu et al., 2006; Chou et al., 2007; Wan et al., 2020).

SCS deep waters originate from the North Pacific Deep Water (NPDW) that penetrate the marginal basin through the Luzon Strait (Qu et al., 2006; Liu et al., 2011; Wang; Jian, 2014; Wan et al., 2018). The route traced from the Luzon Strait to the Northwest suggests a predominantly cyclonic deep circulation (Qu et al. 2006; Wang; Li, 2009). The deep-water residence time of the SCS is estimated to be of approximately 30-50 years, similar to that of intermediate waters, 52 years (Chen et al., 2001). Due to this short residence time, the SCS present a homogeneous vertical profile, below 2000 m there is no evident chemical stratification or changes compared to the Pacific deep-water chemistry (>2000m) characteristics (Chen et al., 2001; 2006; Qu et al., 2009). The rapid residence time potentially implies that, when replaced, deep waters occupy intermediate water levels (between 300 m and 1300 m), contributing to the circulation of intermediate and shallow waters and ocean-atmosphere interactions exchanges (Qu et al., 2009; Tian et al., 2010).

### **3. Material and methods**

#### **3.1 Dissolution experiment**

For the dissolution experiment we used 240 mg of dry sediment obtained from the Western Equatorial Pacific (ODP 807A, 2H2W57-59 cm). The sample was suspended into 120 ml MilliQ water and then the suspension was evenly separated into 6 subsamples. Different amounts (0, 0.4, 0.8, 2, 4 and 6 ml) of Calgon solution made by adding 100 g ( $\text{NaPO}_3$ )<sub>6</sub> into 100 ml MilliQ water was added to the 6 subsamples. To analyze under the microscope an amount of 450  $\mu\text{L}$  of the subsamples were micropipetted into coverslips and dried. Morphological measurements were performed manually on all coccoliths present in each subsample (Supplementary Material 3.1 – Appendix F). The measurements were carried out under a standard polarized microscope (Zeiss AX10) with the gray level calibrated by calcite wedge based on a reference slide (González-Lemos et al., 2018).

To evaluate the effects of the coccolith dissolution under different amounts of Calgon solution we used the mean shape factor  $k_s$  ( $k_s = \text{volume}/\text{length}^3$ ) (Young; Ziveri, 2000) and the relationship between mean length and mean  $k_s$ . The standard deviation of mean  $k_s$  divided by mean  $k_s$  ( $\sigma/\text{mean } k_s$ ) was applied to test whether calcite preservation among coccoliths varied within each sample.

### 3.2 Surface samples analyses

For the core-top analyses, we used smear slides prepared without chemical pre-treatment from core-top samples (N = 28) retrieved from different depths at the SCS (Figure 3.1) during the R/V Sonne cruises (SO-95) (Table 3.1).

Table 3.1. Station, coordinate data and water depth of core-top samples used in this study.

Station	Longitude (E)	Latitude (N)	Water depth (m)
17925	119.047	19.853	2980
17930	115.782	20.333	629
17931	115.963	20.1	1005
17932	116.037	19.952	1365
17934	116.462	19.032	2665
17936	117.12	18.767	3809
17937	117.665	19.5	3428
17938	117.538	19.787	2835
17939	117.455	19.97	2473
17940	117.383	20.117	1728
17941	118.483	21.517	2201
17943	117.553	18.95	917
17944	113.637	18.658	1219
17945	113.777	18.127	2404
17946	114.25	18.125	3465
17949	115.167	17.348	2195
17951	113.41	16.288	2340
17955	112.177	14.122	2404
17956	112.588	13.848	3387
17957	115.31	10.9	2197
17958	115.082	11.622	2581
17959	115.287	11.138	1957
17960	115.558	10.12	1707
17961	112.332	8.507	1795
17962	112.082	7.182	1970
17963	112.667	6.167	1233
17964	112.213	6.158	1556
17965	112.552	6.157	889

Microscope image processing was performed for all core-top samples (N = 28) to obtain morphological attributes and estimate coccolithophore calcification. The images were obtained using a Polarized Microscope (Zeiss Axio Scope HAL100), configured with circularly polarized light and a Zeiss Plan-APOCHROMAT 100x/1.4 oil objective, with a coupled camera (Zeiss AxioCam 506 Color) and the Zeiss Software. The scale and gamma values of the Zeiss Software were configured at the beginning of each session, as

well as the calibration, using a reference slide according to González-Lemos et al. (2018). The microscope's light intensity and the software's color balance settings have been adjusted to obtain an image similar to the reference. The obtained image was inserted into the C-calcita software (Fuentes et al., 2014) for color calibration. After calibration, the samples were processed at the microscope. At least 40 fields of view of each sample were photographed. The images of each sample were saved and uploaded into the C-calcita software at each session. For each batch of samples, a filter to remove the color background values applied in C-Calcita to detect the limits between each lith and the dark background. Then the software selected and cropped each image of interest by the limit boundary established between the pixels and automatically generated a file for each one with the data of major and minor axis length, volume, area, and mass. After manually cleaning the segmented images, a minimum of 200 entire coccolithophores images belonging to the Noelaerhabdaceae family (*Emiliana huxleyi* and *Gephyrocapsa* spp., > 2  $\mu\text{m}$ ) were kept for each sample, for which the morphological attributes major and minor length and calcified area was measured using C-Calcita. Finally, we calculated for each coccolithophore image the thickness (Beaufort et al., 2014) and the mean ks (Young; Ziveri, 2000).

Annual means of different physical-chemical and biological variables for the location of the surface samples (Table 3.1) were extracted using different databases. Seawater temperature, salinity, phosphate, and nitrate data were obtained from WOA01. Chlorophyll concentration data were based on MODIS data (2003-2016) extracted from Oregon State University Ocean Productivity (<http://www.science.oregonstate.edu/ocean.productivity/>). Annual concentrations of total alkalinity (Total alkalinity – TALK) and total concentration of carbon dioxide (Total carbon dioxide –  $\text{TCO}_2$ ) were extracted from Goyet et al. (2000). The carbonate ion concentration, pH,  $\text{pCO}_2$ , and  $\Omega_{\text{Ca}}$  were calculated using previously extracted variables of the input  $\text{CO}_2$  system parameters, salinity, SST, pressure, total phosphate, total silicate, TALK and  $\text{TCO}_2$ , using  $\text{CO}_2\text{SYS}$  excel macro (Pierrot et al., 2012). The environmental parameters were extracted at 50 m depth according to the highest concentration of coccolithophorid cells belonging to the Noelaerhabdaceae group, *Emiliana huxleyi* and *Gephyrocapsa* spp., which are also the most abundant taxa living in then the SCS (Jin et al., 2016). In addition, we estimated the  $\Omega_{\text{Ca}}$  at the depth at which the samples were recovered. Data for the calculation of light intensity at 50 m water depth was estimated

using a photosynthetic active radiation (PAR) penetration model (Buiteveld, 1995; Murtugudde et al., 2002) and extracted from the MODIS Ocean database (<http://oceancolor.gsfc.nasa.gov/cgi/13>).

### 3.3 Statistical analysis

Morphological attributes (length, volume, thickness and ks) of the coccolithophore assemblages found in the surface sediment samples and environmental data were normalized using box-cox transformation and combined in a redundancy analysis (RDA) to assess the potential relationships between morphological measurements and environmental parameters. Statistical analyzes were performed using the PAST 4.06 software (paleontological statistics, Hammer et al., 2021).

## 4. Results

### 4.1 Effects on coccoliths morphology in the dissolution experiment

In the dissolution experiment mean ks decreased according to the amount of Calgon solution (Figure 3.2A). The mean ks varied between 0.12 (0 ml) and 0.04 (6 ml) (Figure 3.2B). The  $\sigma$ /mean ks showed variation in preservation among coccoliths within each sample. Higher differences in standard deviation were observed in samples containing 2 ml, 4 ml, 0.8 ml, 0.4 ml, 0 ml, and 6 ml respectively (Figure 3.3A). Increasing the amount of Calgon solution up to 2 ml reflected a decrease in mean ks and an increase in standard deviation. Samples with 4 and 6 ml Calgon solution recorded decreased mean ks and standard deviation among coccoliths (Figure 3.3A). The lowest mean ks (0.04) and the maximum of the mean length (3.95) was recorded under the greatest amount of Calgon solution (6 ml) (Figure 3.3B). Increased amounts of Calgon solution also resulted in a gradual increase in length (Figure 3.3B).

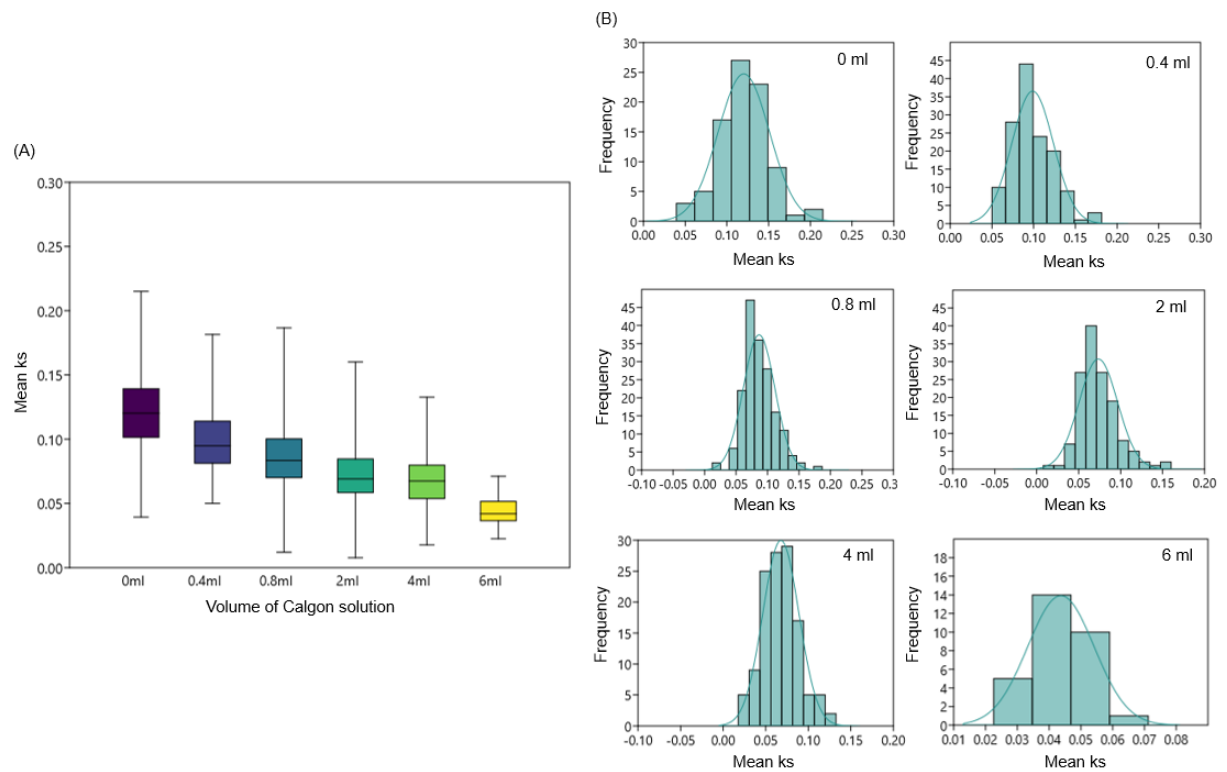


Figure 3.2. Coccolith mean  $ks$  variation in the dissolution experiment. (A) Box plots of coccoliths mean  $ks$  under different volume of Calgon solution added and (B) histograms showing mean  $ks$  frequency in each subsample.

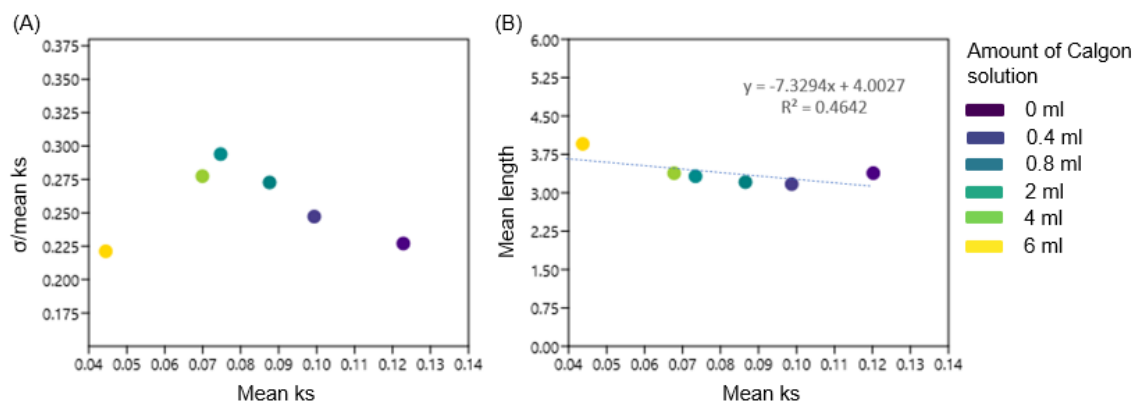


Figure 3.3. Coccolith preservation in subsamples treated with different volumes of Calgon solution. (A) Scatter plot of mean  $ks$  and  $\sigma/\text{mean } ks$  and (B) linear correlation between mean  $ks$  and mean length.

#### 4.2 Biological and environmental effects on surface samples calcite variation

The mean  $ks$  and mean thickness presented similar trends along the core-top sampling stations (Figure 3.4). The mean  $ks$  varied between 0.03 and 0.07, and the mean thickness between 0.25 and 0.44, both with maximum values recorded at station (17931) located in northern SCS at 1005 m water depth. The mean length varied between 3.23 and



3.78 with higher values recorded at 2195 m water depth in northern SCS. The mean volume and mass presented similar trends. The mean volume varied between 1.70 and 2.97, and mean mass between 4.61 and 8.03 with maximum values for both recorded in the shallowest station at 629 m water depth in northern SCS.

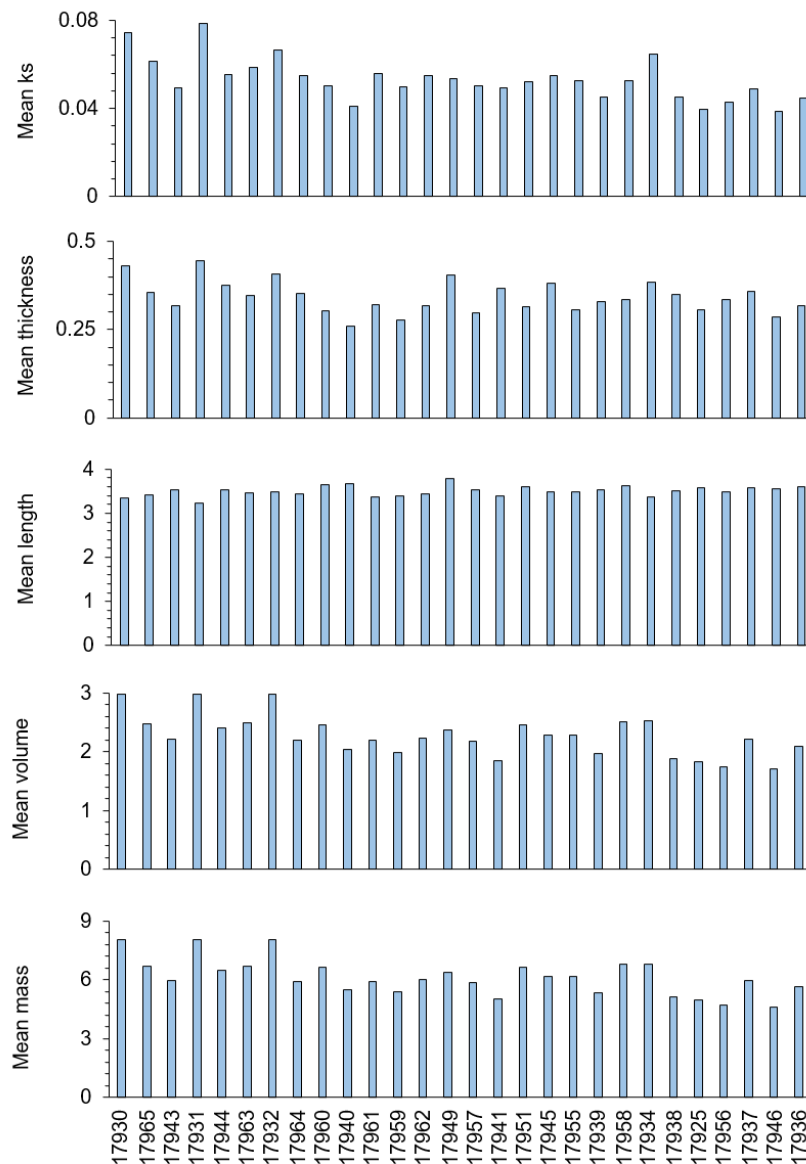


Figure 3.4. Arithmetic means of the biological variables evaluated on the surface samples. The sampling stations are distributed along the x-axis according to the depth from the shallowest (closest to origin) to the deeper.

Considering the results from the dissolution experiment, we evaluated whether the observed trends in the mean ks and  $\sigma$ /mean relationships and between mean ks and mean length were also reproducible in the surface sediment samples (Figure 3.5). The  $\sigma$ /mean ks from stations located above 2000 m showed a linear correlation with the

preservation of calcite (mean ks) (Figure 3.5A). In these samples, smaller mean ks reflects smaller standard deviation. While in the samples below 2000 m there is no clear pattern of variation related to the mean ks standard deviation. The mean ks vs mean length show a significant relationship ( $R^2 = 0.37$ ), in which larger coccoliths corresponded to lower mean ks (Figure 3.5B).

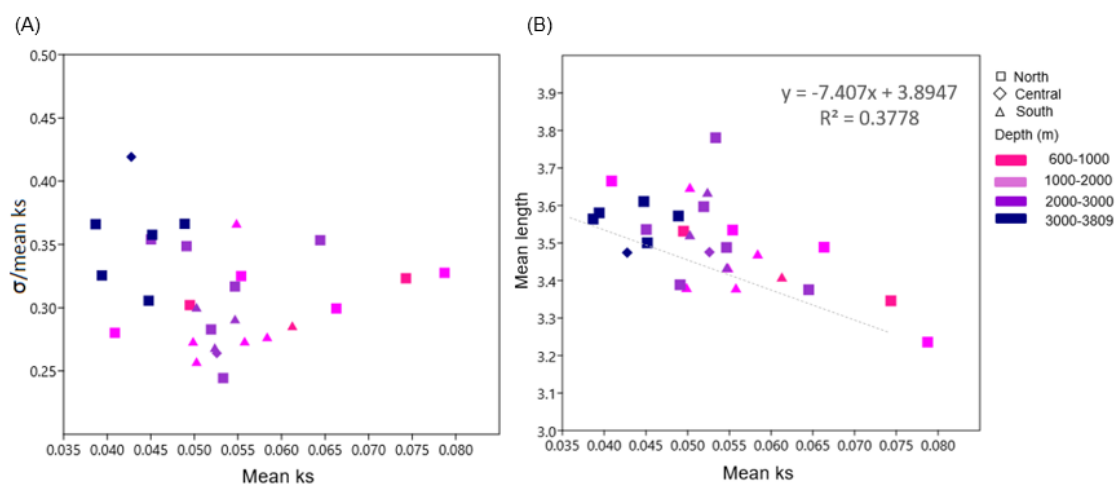


Figure 3.5. Coccolith preservation in surface sediments (A) Scatter plot between mean ks and  $\sigma/\text{mean ks}$  and (B) linear correlation between mean ks and mean length.

We analyzed the correlations between the biological and environmental datasets (Table 3.2). We observed highest correlation between mean ks, mean volume and mass with  $\Omega_{\text{Ca}}$  ( $r = 0.67$ ,  $r = 0.66$  and  $r = 0.66$ , respectively, all  $p < 0.05$ ). The mean thickness was correlated with nitrate, phosphate and  $\Omega_{\text{Ca}}$  ( $r = 0.44$ ,  $0.40$  and  $0.41$ , respectively). The mean length showed no significant correlation to any of the environmental variables. Albeit no significant, the mean length was better correlated with PAR ( $r = 0.35$ ). This null response to the environmental parameters is also seen in the RDA in which the mean length occupies a position near the center of the ordination space (Figure 3.6).

We evaluated the influence of the multiple environmental variables on the morphology of coccoliths in the surface samples using the RDA. The RDA1 and RDA2 explained together by the environmental dataset 58.34% of the total variation of the morphological data. The samples (color coded by different depth intervals) are mainly distributed along RDA1 which explained 54.65% of the variation (Figure 3.6), and is mainly correlated to  $\Omega_{\text{Ca}}$ , but also to chlorophyll, PAR, and nitrate. The RDA2 explained

3.69% of variance and it is mostly correlated to the salinity, temperature, pH, phosphate, TALK, and  $\text{PCO}_2$ .

Table 3.2. Correlation matrix (p value and Pearson correlation) between biological and environmental variables.

Environmental /Biological	p value					r				
	mean ks	mean thickness	mean length	mean volume	mean mass	mean ks	mean thickness	mean length	mean volume	mean mass
Salinity	0.7870	0.0715	0.8683	0.8657	0.8656	-0.0535	0.3458	0.0328	-0.0335	-0.0335
Temperature	0.9396	0.0398	0.9982	0.8968	0.8969	-0.0150	-0.3907	0.0004	-0.0257	-0.0257
Phosphate	0.8719	0.0303	0.6304	0.9569	0.9566	0.0319	<b>0.4100</b>	-0.0951	-0.0107	-0.0108
Nitrate	0.3623	0.0180	0.2945	0.7144	0.7141	0.1789	<b>0.4437</b>	-0.2054	0.0724	0.0724
TALK	0.5315	0.1345	0.7090	0.5917	0.5917	-0.1234	0.2899	0.0738	-0.1059	-0.1059
chlor_a	0.2564	0.1825	0.8798	0.1808	0.1808	0.2219	0.2594	-0.0299	0.2604	0.2604
PAR	0.2827	0.0459	0.0607	0.4991	0.5001	-0.2103	-0.3803	0.3589	-0.1332	-0.1329
pH	0.1772	0.3098	0.3831	0.2404	0.2406	-0.2625	0.1991	0.1714	-0.2294	-0.2293
pCO <sub>2</sub>	0.1614	0.3323	0.3768	0.2177	0.2180	0.2720	-0.1902	-0.1737	0.2405	0.2404
$\Omega_{\text{Ca}}$	0.0001	0.0287	0.0544	0.0001	0.0001	<b>0.6781</b>	<b>0.4135</b>	-0.3674	<b>0.6638</b>	<b>0.6637</b>

Bold values indicate significant correlations.

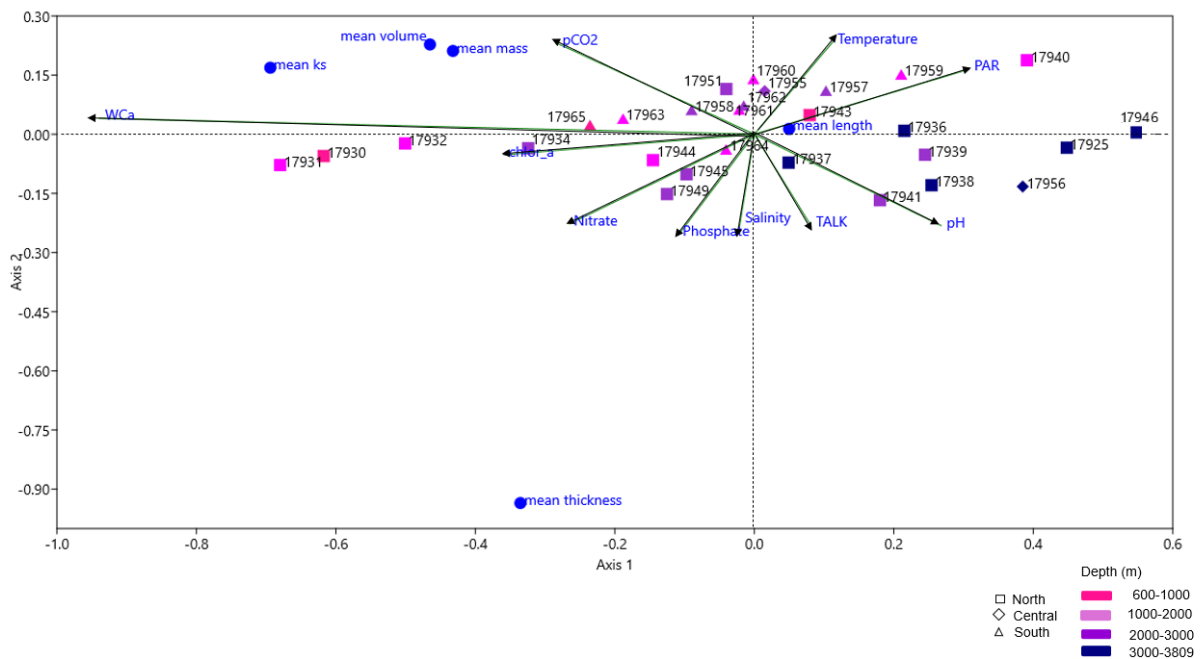


Figure 3.6. Redundancy analysis (RDA) ordinations for environmental variables and morphological measurements and calcite estimation of coccoliths. Sample depths are indicated by different colors. Squares correspond to samples from northern SCS, diamonds from central part, and triangles from southern SCS.

Given that  $\Omega_{Ca}$  is the most important environmental variable driving the morphological dataset, and shows high correlation with mean ks, we performed a linear regression between mean ks and  $\Omega_{Ca}$ , which showed that 47% of the variance in mean ks is explained by  $\Omega_{Ca}$  (Figure 3.7).

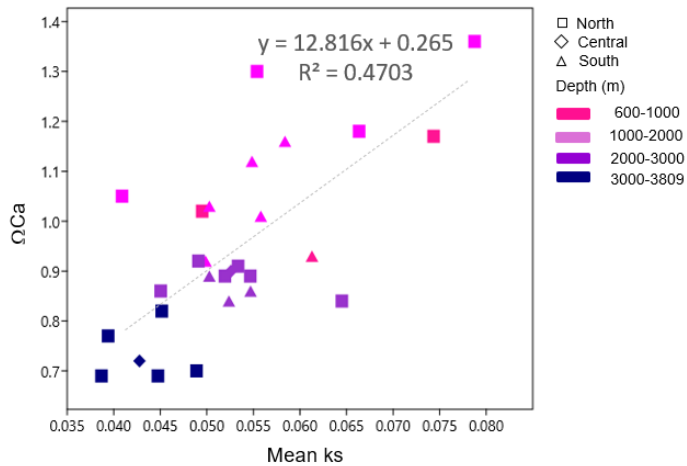


Figure 3.7. Linear correlation between  $\Omega_{Ca}$  at bottom depths and mean ks from surface samples.

## 5. Discussion

### 5.1 Coccolith morphology under controlled dissolution conditions

Under controlled laboratory conditions, the morphological attributes of mean ks and coccolith length showed different stages of preservation according to the dissolution conditions which helps to elucidate the coccolithophores' integrity. Subsamples exposed to lower amounts of the Calgon solution presented greater carbonate preservation reflected by higher mean ks values (Figure 3.2A). The samples with the best preservation presented higher mean ks and lower length (Figure 3.3B), with assemblages of heterogeneous sizes of *Gephyrocapsa* spp. (2  $\mu\text{m}$  – 5  $\mu\text{m}$ ) represented. The gradual decrease in mean length with the increase in Calgon concentration is due to the progressive dissolution of the smallest coccoliths (smallest area). This pattern of preservation increased the length of the coccoliths inversely related to calcite preservation, since under conditions of greater dissolution only the largest coccoliths resisted; however, with lower values of mean ks, reflecting the selective dissolution of coccoliths by size.

Changes in the standard deviation/mean ks ratio in the dissolution experiment reflect variations in the composition of the assemblages resulting from the difference

between the dissolved coccoliths and the more resistant ones. In the subsample with no Calgon solution, most of the coccoliths are well preserved and reflected high mean  $k_s$  and small standard deviation. The standard deviation reflects the different effect of dissolution on large and small coccoliths. As the amount of solution added to each subsample increases, small coccoliths dissolve preferentially, decreasing the mean  $k_s$  and increasing the standard deviation (Figure 3.3). With higher amounts of Calgon solution (4 and 6 ml), this pattern reverses and mostly small coccoliths are dissolved, resulting in an assemblage dominated by larger coccoliths (Figure 3.3B). Under these highest dissolution stages, the larger coccoliths are also partially dissolved then both mean  $k_s$  and standard deviation decrease (Figure 3.3).

The laboratory experiment showed that under controlled conditions (known changes in water chemistry and uniform species composition) the variations in coccolith morphology (mean length and mean  $k_s$ ) reflected different degrees of dissolution. We also observed a length-related dissolution pattern, where smaller coccoliths are gradually being dissolved with the increase in Calgon concentration, leading to higher average length but lower mean  $k_s$ . This selective size dissolution pattern has been also observed in a similar experiment carried out by Jin et al. (2019) using a surface sediment sample from the East China Sea with similar assemblage composition as in the sample used in our experiment, which was acidified with different concentrations of HCl. These authors found that *E. huxleyi* and small *Gephyrocapsa* spp. Individuals ( $< 3 \mu\text{m}$ ) presented lower preservation compared to larger ones ( $> 3 \mu\text{m}$ ), which was interpreted as a selective size dissolution pattern. On the other hand, Beaufort et al. (2007) found no differences related to the preferential dissolution in coccoliths' mass and size in an acidification experiment with HCl. Our results reflect the same phenomenon of selective preservation reported by Jin et al. (2019) with smaller coccoliths dissolving first, however, the decrease in mean  $k_s$  is observed continuously as the dissolution condition increases (Figure 3.3B). The recovery of the calcite by recrystallization was tested by Jin et al. (2019) and the increasing thickness and coccolith weight in the acidification experiment are possible due to the increased solvent resulted from carbonate dissolution. Here, the Calgon solution inhibits calcite precipitation (Brooks et al., 1951) and possible weight gain due to calcite overgrowth (Jin et al., 2019) resulting in a linear relationship between increasing amounts of solution and decreasing mean  $k_s$ .

## 5.2 Effects of dissolution on the morphology of coccoliths in surface sediments

Coccolith assemblages present in surface sediments from SCS in the depth range between 629-3809 m showed variations in their morphological attributes (mean  $k_s$ , thickness, length, volume, and mass). These variations were evaluated in relation to multiple environmental variables that potentially influence the calcification process during coccolithophorids life cycle and carbonate preservation following its death (Figure 3.6). Our results show that morphological attributes, such as mean thickness and length, present significant correlations to upper water column parameters (i.e., temperature, nutrients and PAR, Table 3.2). This is expected once changes in living coccolithophorids size from SCS evaluated by length and thickness are mainly associated with variations in nutrient availability and light at upper water column (Jin et al., 2016). While the strong correlation between mean  $k_s$  and  $\Omega_{Ca}$  indicates that the  $k_s$  shape factor is a good proxy for post burial dissolution in the SCS (Table 3.2, Figure 3.7). Although volume, mass, and thickness are also highly correlated with  $\Omega_{Ca}$ , these morphological attributes vary according to the morphology of each species, including variations in coccolith circularity and cell sizes (Young; Ziveri, 2000; Bolton et al., 2016). In addition, the thickness is a morphological pattern sensitive to post-depositional effects and upper water column parameters during its life cycle. Therefore, even though they were primarily influenced by the  $\Omega_{Ca}$  (Table 3.2, Figure 3.6), the mean  $k_s$  is more stable and better suited to evaluate the morphological changes in coccoliths in our dataset. Overall, the deepest samples present lower mean  $k_s$  (higher dissolution) because they are under the lowest  $\Omega_{Ca}$  conditions.

The standard deviation of  $k_s$ /mean  $k_s$  (Figure 3.5) obtained for the surface sediment samples shows a similar relationship as in the laboratory experiment for Calgon concentrations between 2-6 ml, at least for samples located between 600-2000 m. The increasing standard deviation of  $k_s$ /mean  $k_s$  ratio with higher mean  $k_s$  reflect differential dissolution among the coccolith sizes (Figure 3.5A). In this way, samples that are more (less) susceptible to dissolution result in more homogeneous (heterogeneous) assemblages regarding the carbonate preservation. However, in stations deeper than 2000 m these relationships are more scattering compared to the linear correlations of the dissolution experiment. These differences can be explained by the natural variability of the surface sediment samples in terms of geographically differences in multiple factors that affect living coccolithophores, and a not uniform coccolithophore assemblage

composition in contrast to the laboratory experiment, where we analyzed the same assemblage divided into subsamples conditioned to a single variable (carbonate dissolution).

The mean  $k_s$  and mean length relationships in the surface samples (Figure 3.5B) show at least a similar trend to laboratory observations (Figure 3.3B). Lower mean  $k_s$  corresponded to the assemblages with larger coccoliths (Figure 3.5B). In this way, the coccoliths at the deepest surface sediment samples show largest size and lower  $k_s$ , driven mainly by the dissolution of the smallest species due to the lower  $\Omega_{Ca}$  at bottom depth. As seen in the laboratory experiment and reported for surface sediments from the East China Sea (Jin; Liu, 2017; Jin et al., 2019). The coccolith dissolution observed in surface sediments from East China Sea was associated with organic matter degradation (Jin et al., 2019). Our study shows that the coccoliths mean  $k_s$  is highly sensitive to taphonomical processes, regardless of the driver (i.e.,  $\Omega_{Ca}$  or degradation of organic matter). Hence, our results demonstrate that the preservation of coccoliths at depths above the lysocline may respond to post burial carbonate dissolution, and that the mean  $k_s$  can be applied as a good proxy to assess past ocean carbonate changes.

According to our results, the morphological attribute that best explains the variation of coccolith assemblages in surface samples from the SCS is the  $k_s$  factor which primary reflect changes in  $\Omega_{Ca}$  at bottom depth. Variations in the  $k_s$  factor and its relationship with the size of the coccoliths showed high sensitivity of this morphological attribute to the post-depositional effects of carbonate dissolution and that the dissolution occurs selectively according to the coccoliths size. In this way, geological records that evaluate parameters such as length and weight may be observing the effects of partial dissolution. Additionally, our results demonstrate that the coccolith thickness also applied as a dissolution proxy is sensitive both to the effects of post burial carbonate dissolution and to a lesser extent, nutrient variations in the water column during the calcification.

### 5.3 Coccoliths morphological attributes as dissolution proxy: implications for the SCS paleoceanography

Changes in the size and calcification of Noelaerhabdaceae coccoliths, evaluated by mass and thickness, have been mainly associated with variations in nutrient availability and carbonate chemistry parameters in the water column, while dissolution effects have been reported to be less likely to drive changes in the morphology of

coccolithophores fossil assemblages (Beaufort et al., 2011; Su et al., 2020; Jin et al., 2022). However, according to our dissolution experiment and surface sediment data, the decrease in the saturation state of calcite is the driver of coccolith dissolution and, consequently, smaller mean  $k_s$  factor. Therefore, we applied the mean  $k_s$  as a dissolution proxy in the paleoceanographic reconstruction of a 210 kyr record from the northern SCS (ODP 1146, 19°27' N, 116°16' E, 2092 m of water depth). The chronological framework of the record is based on their original age models established with benthic oxygen isotopes (Clemens and Prell, 2003). The  $k_s$  factor was obtained for the Noelaerhabdaceae family (*Emiliana huxleyi* and *Gephyrocapsa* spp., > 2  $\mu\text{m}$ ). The mean  $k_s$  varied between 0.014 and 0.080, with higher values recorded during the interglacials MIS 5 and MIS 3, reflecting more calcite saturated waters (Figure 3.8A). A decrease in mean  $k_s$  was recorded from MIS 5 to MIS 4 followed by an abrupt increase during the MIS 4 and MIS 3 transition. The lower mean  $k_s$  values recorded during MIS 4 and 2, and the LGM, indicates undersaturated ( $\Omega_{\text{Ca}} < 1$ ) waters during these intervals. Hence, the mean  $k_s$  record of ODP 1146 suggests that over the last 210 kyr the SCS experienced lysocline depth changes, leading to undersaturated waters (shallower lysocline) during glacial periods and the LGM.

At core MD05-2904 (2066 m water depth), there is an increased in weight of the coccoliths belonging to the Noelaerhabdaceae family during glacial to interglacial transitions and the LGM (Figure 3.8B, Su et al., 2020). A similar trend is observed in the calcification index except during Termination II when they present opposite patterns (Figure 3.8B, Su et al., 2020). According to these authors, this difference was related to different environmental controls on coccolith calcification according to size class, being driven by nutrient availability (coccoliths > 3  $\mu\text{m}$ ) or by changes in carbonate chemistry parameters during the life cycle (coccoliths < 3  $\mu\text{m}$ ). The increased calcification index at MD05-2904 was also related to higher abundances of larger and heavier *G. oceanica* (Su et al., 2020). Greater calcification of *G. oceanica* and increased coccolith mass during the LGM were also related to changes in carbonate chemistry variations in the water column in the South Indian Ocean and North Atlantic Ocean (Beaufort et al., 2011). These authors reported higher intracellular calcite production driven by increased  $[\text{CO}_3^{2-}]$  (Beaufort et al., 2011). However, the ODP 1146 mean  $k_s$  record presented an opposite pattern, suggesting that variations in lysocline depth was an important mechanism for  $\text{CaCO}_3$  preservation.



In the SCS lower benthic foraminifera  $\delta^{13}\text{C}$  during glacial periods and the LGM show similar trends to the coccolithophore ODP 1146 mean ks record (Figure 3.8C) and suggest more stratified waters during these intervals (Wan; Jian, 2014; Wan et al., 2018). According to Wan et al. (2020) changes in the  $[\text{CO}_3^{2-}]$  and  $\delta^{13}\text{C}$  gradient between the Pacific and the SCS during extreme glacial conditions corresponded to a weakened deep-water ventilation and more sluggish Pacific deep-water circulation relative to interglacial conditions. The poorly ventilated and more stratified water column would then drive changes in glacial lysocline depth promoting greater  $\text{CaCO}_3$  dissolution and increased ALK and carbon storage (Wan et al., 2020). A stronger dissolution during glacial conditions recorded by the ODP 1146 mean ks record is also consistent with B/Ca records from northern and southern SCS (MD05-2904, 2066 m water depth and MD05-2896, 1657 m water depth, respectively) where these intervals correspond to the presence of more corrosive waters (Figure 3.8D, Wan et al., 2020). Additionally, the increased carbonate dissolution over interglacial/glacial transitions recorded in planktonic foraminifera fragmentation index above the lysocline depths of the southern SCS (core 17957-2, 2195 m water depth) is also associated with changes in the Pacific Ocean carbon chemistry and deep-water circulation (Figure 3.8E, Li et al., 2001). This carbonate preservation pattern is consistent with atmospheric  $\text{CO}_2$  variations recorded from ice cores that suggest greater  $\text{CO}_2$  transfer and storage during the glacials and LGM mainly related to temperature and changes in deep water circulation (Figure 3.8F, Sarmiento; Gruber, 2006; Goodwin et al., 2013; Zeebe, 2012; Yu et al., 2014; Wang et al., 2016). Hence, we suggest that changes in lysocline depth in response to less ventilated and more stratified waters promoted by changes in deep-water circulation at northern SCS were the main driver of changes in carbonate dissolution in the last 210 kyr. Additionally, the glacial-interglacial dissolution variations from morphological attributes of coccoliths at ODP 1146 can provide potential information about the role of deep-water circulation in carbon storage.

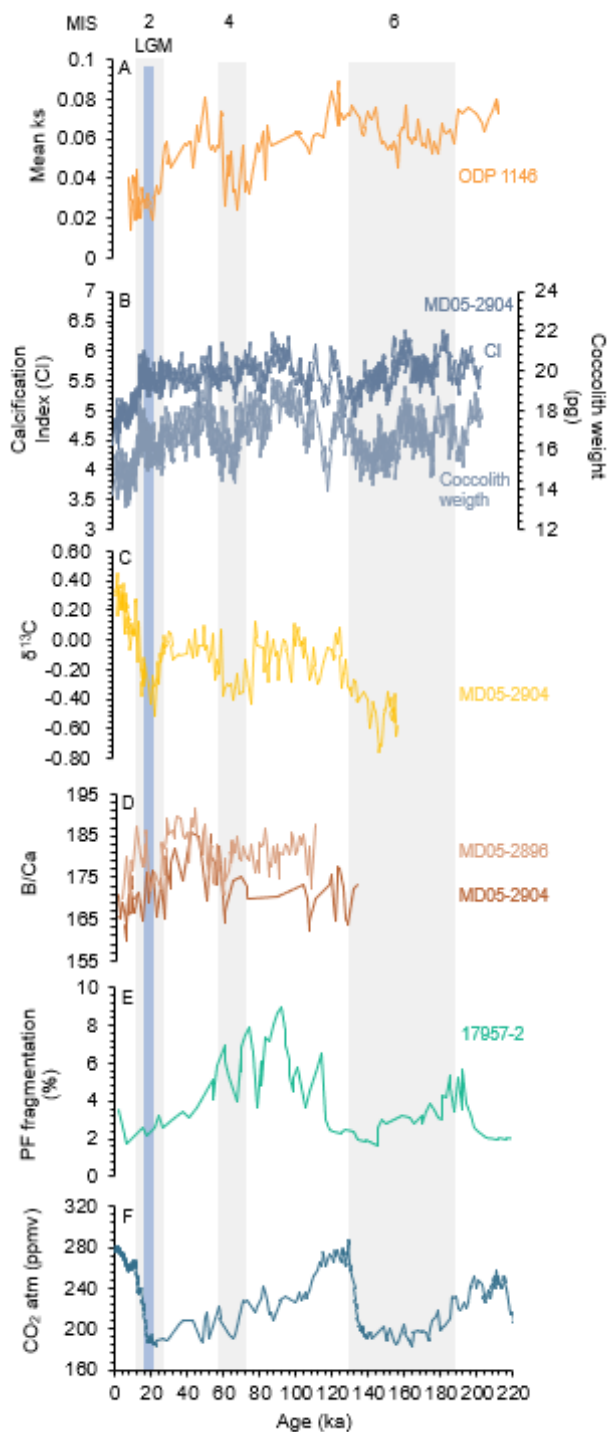


Figure 3.8. Downcore record of coccolith mean ks compared to carbonate system parameters and other proxies. (A) Coccolith mean ks obtained from ODP 1146 (2090 m water depth, this study); (B) Coccolith calcification index and weight from Noelaerhabdaceae ( $> 2 \mu\text{m}$ ) obtained from MD05-2904 (2066 m water depth, Su et al., 2020); (C)  $\delta^{13}\text{C}$  from benthic foraminifera recorded at MD05-2904 (Wan et al., 2020); (D) B/Ca record from northern (MD05-2904, 2066 m water depth) and southern SCS (MD05-2896, 1657 m water depth); (E) Planktonic foraminifera fragmentation (%) from northern SCS (17957-2, 2195 m water depth, Li et al., 2001); and (F) Atmospheric  $\text{CO}_2$  record (Lüthi et al., 2008).

## 6. Conclusions

In this study, we evaluated the effects of dissolution on morphological attributes changes of the Noelaerhabdaceae family ( $> 2 \mu\text{m}$ ) in a laboratory experiment. In our experiment, the changes in coccoliths mean  $k_s$  reflected different degrees of dissolution. A length-related dissolution pattern was observed in the laboratory, where small coccoliths are most prone to suffer dissolution, increasing larger coccolith specimens and affecting the assemblage composition. To test and extrapolate these findings to the field we evaluated the influence of environmental factors and carbonate chemistry parameters on the morphological attributes of coccoliths from surface sediments collected along with the SCS at different depths. The volume, mass, and  $k_s$  factor from fossil coccolithophore assemblages were mainly controlled by changes in carbonate saturation affecting post-burial coccolith preservation. When applied as a dissolution proxy in a sedimentary record from northern SCS, the mean  $k_s$  recorded glacial-interglacial changes in carbonate saturation and dissolution over the last 210 kyr, in line with changes in deep-water circulation between Pacific and SCS. We argue that less ventilated water and enhanced stratification in the glacial stages and LGM resulted in a shallower lysocline, strengthening the dissolution of  $\text{CaCO}_3$ . Our results demonstrate that although coccolithophore dissolution might not be evident using other proxies, it can be detected by analyzing the  $k_s$  factor which can be potentially applied as a dissolution proxy to track changes in carbonate saturation state and that post-burial dissolution effects might occur more often than previously thought.

## Acknowledgments

This research used samples and data provided by the International Ocean Discovery Program (IODP). Funding was provided by Coordenação de Aperfeiçoamento de Pessoal de Nível Superior – Brasil (CAPES) - Finance Code 001 and CAPES-PRINT – Programa Institucional de Internacionalização - Process: 88887.571907/2020-00.

### 3. CONCLUSIONS

A multiproxy approach in the down cores and marine surface sediments retrieved at different depths in the SCS allowed evaluation of the processes that primarily controlled the carbonate preservation in this marginal basin. The results allowed a better understanding of the influence of environmental factors, including EAM dynamics, and parameters of ocean carbonate chemistry on the composition of marine sediments from SCS. This study hypothesized that variations in carbonate saturation limits along the Quaternary reflected changes in composition and morphology of micro and nanofossil assemblages at different depths of the SCS in response to dissolution effects. This hypothesis was confirmed, since the records located below the depths of the lysocline and CCD were under strong conditions of carbonate dissolution inherent to the depth with secondary influences (i. e., primary productivity, turbidities occurrence, and greater terrigenous supply) affecting the carbonate presence in the sedimentary records. The dissolution experiment and surface sediment evaluation showed that changes in coccolith morphology were primarily controlled by changes in carbonate saturation. The calibration of the coccoliths shape factor ( $k_s$ ) provided a new proxy to assess changes in carbonate dissolution limits over the Quaternary. The main conclusions of this work were that the carbonate sediments of the SCS along the Quaternary recorded primarily the post-burial effects of dissolution, and that carbonate dissolution can be detected at different depths by analyzing the coccolith's  $k_s$  factor which can potentially be applied to track changes in carbonate saturation state.

## REFERENCES<sup>1</sup>

- Archer DE. An atlas of the distribution of calcium carbonate in sediments of the deep-sea. *Global Biogeochem Cycles*. 1996;10(1): 159–74.
- Balestrieri C Ziveri P, Grelaud M, Mortyn PG, Agnini C. Enhanced *E. huxleyi* carbonate counterpump as a positive feedback to increase deglacial pCO<sub>2sw</sub> in the Eastern Equatorial Pacific. *Quat Sci Rev*. 2021; 260:106921. doi.org/10.1016/j.quascirev.2021.106921.
- Barker S, Archer D, Booth L, Elderfield H, Henderiks J, Rickaby REM. Globally increased pelagic carbonate production during the Mid-Brunhes dissolution interval and the CO<sub>2</sub> paradox of MIS 11. *Quat Sci Rev*. 2006;25: 3278–3293.
- Bastian L., Revel M., Bayon G., Dufour A., Vigier N. Abrupt response of chemical weathering to Late Quaternary hydroclimate changes in northeast Africa. *Sci Rep*. 2017;1–8. doi.org/10.1038/srep44231.
- Baumann K-H, Freitag T. Pleistocene fluctuations in the northern Benguela current system as revealed by coccolith assemblages. *Mar Micropaleontol*. 2004;52: 195–215. doi.org/10.1016/j.marmicro.2004.04.011.
- Bé AWH. Foraminifera families: Globigerinidae and Globorotaliidae. In: Fraser, JH (Ed.), *Fiches d'Identification du Zooplancton*; 1967. p. 81–97.
- Beaufort L, Barbarin N, Gally Y. Optical measurements to determine the thickness of calcite crystals and the mass of thin carbonate particles such as coccoliths. *Nat Protoc*. 2014;9(3): 633–642. doi.org/10.1038/nprot.2014.028.
- Beaufort L, Probert I, Buchet N. Effects of acidification and primary production on coccolith weight: Implications for carbonate transfer from the surface to the deep ocean. *Geochemistry, Geophys Geosystems*. 2007;8(8):1–18. doi.org/10.1029/2006GC001493.
- Beaufort L, Probert I, De Garidel-Thoron T, Bendif EM., Ruiz-Pino D, Metzl N, et al. Sensitivity of coccolithophores to carbonate chemistry and ocean acidification. *Nature*. 2011;476(7358): 80–83. doi.org/10.1038/nature10295.
- Berger WH. Biogenous deep-sea sediments: fractionation by deep-sea circulation. *Geol Soc Am Bull* 1970;81(5): 1385–1402. doi.org/10.1130/0016-7606(1970)81[1385:BDSFBD]2.0.CO;2.
- Berger WH. Deep-sea carbonates: Dissolution profiles from foraminiferal preservation. In: Be, A W H, Berger, W H (Eds.), *Dissolution of Deep-Sea Carbonates*, 13. Special Publication Cushman Found. Foraminifer Res. 1975. pp. 82–86.
- Berger WH. Planktonic foraminifera: selective solution and paleoclimatic interpretation. *Deep-Sea Res*. 1968;15(1): 31–43. doi.org/10.1016/0011-7471(68)90027-2.

<sup>1</sup>According to Vancouver Style

- Betzler C, Eberli GP, Zarikian CAA. Expedition 359 Scientific Prospectus Sea Level , Currents , and Monsoon Evolution. International Ocean Discovery Program Scientific Prospectus, 2014. 359. doi.org/10.14379/iodp.sp.359.2014.
- Bolton CT, Hernández-Sánchez MT, Fuertes MÁ, González-Lemos S, Abrevaya L, Mendez-Vicente A, et al. Decrease in coccolithophore calcification and CO<sub>2</sub> since the middle Miocene. *Nat Commun.* 2016;7: 10284. doi.org/10.1038/ncomms10284.
- Bordiga M, Beaufort L, Cobianchi M, Lupi C, Mancin N, Luciani V, Pelosi N, Sprovieri M. Calcareous plankton and geochemistry from the ODP site 1209B in the NW Pacific Ocean (Shatsky Rise): New data to interpret calcite dissolution and paleoproductivity changes of the last 450 ka. *Palaeogeogr Palaeoclimatol Palaeoecol.* 2013;371(1): 93–108. doi.org/10.1016/j.palaeo.2012.12.021.
- Broecker WS. A need to improve reconstructions of the fluctuations in the calcite compensation depth over the course of the Cenozoic Wallace. *Paleoceanography.* 2008;23(1): PA1204. doi.org/10.1029/2007PA001456.
- Brooks R, Clark LM., Thurston EF. Calcium Carbonate and Its Hydrates. *Philosophical Transactions of the Royal Society of London. Series A, Mathematical and Physical Sciences.* 1950;243(861): 145–167. <http://www.jstor.org/stable/91442>.
- Buiteveld H. A model for calculation of diffuse light attenuation (PAR) and Secchi depth. 1995;29(1): 55-65. doi.org/10.1007/BF02061789.
- Chen C, Jan S, Kuo T, Li S. Nutrient flux and transport by the Kuroshio east of Taiwan. *J Mar Syst.* 2017;167: 43–54. doi.org/10.1016/j.jmarsys.2016.11.004.
- Chen CTA, Wang S-L, Chou WC, Sheu DD. Carbonate chemistry and projected future changes in pH and CaCO<sub>3</sub> saturation state of the South China Sea. *Mar Chem.* 2006;101(3–4): 277–305. doi.org/10.1016/j.marchem.2006.01.007.
- Chen CTA, Wang S-L, Wang B-J, Pai S-C. Nutrients budgets for the South China Sea basin. *Mar Chem.* 2001;75(4): 281–300. doi.org/10.1016/S0304-4203(01)00041-X.
- Chen M-T, Shiau L-J, Yu P-S, Chiu T-C, Chen Y-G, Wei K-Y. 500 000-year records of carbonate, organic carbon, and foraminiferal sea-surface temperature from the southeastern South China Sea (near Palawan Island). *Palaeogeogr Palaeoclimatol Palaeoecol.* 2003;197(1-2): 113–131. doi.org/10.1016/S0031-0182(03)00389-4.
- Chen M-T, Wang CH, Huang CY, Wang P, Wang L, Sarnthein M. A late Quaternary planktonic foraminifer faunal record of rapid climatic changes from the South China Sea. *Mar Geol.* 1999;156(1–4): 85–108. doi.org/10.1016/S0025-3227(98)00174-1.
- Chen Q, Kissel C, Liu Z. Late Quaternary climatic forcing on the terrigenous supply in the northern South China Sea: Input from magnetic studies. *Earth Planet Sci Lett.* 2017;471: 160-171. doi.org/10.1016/j.epsl.2017.04.047.
- Chen Y-LL, Chen H-Y, Chung C-W. Seasonal variability of coccolithophore abundance and

- assemblage in the northern South China Sea. *Deep-Sea Res II Top Stud Oceanogr.* 2007;54(14-15): 1617–1633. doi.org/10.1016/j.dsr2.2007.05.005.
- Chen Y-LL. Spatial and seasonal variations of nitrate-based new production and primary production in the South China Sea. *Deep-Sea Res I Oceanogr Res Pap.* 2005;52(2): 319–340. doi.org/10.1016/j.dsr.2004.11.001.
- Cheng H, Edwards RL, Broecker WS, Denton GH, Kong X, Wang Y, Zhang R, Wang X. Ice Age Terminations. *Science.* 2009;326(5950): 248–252. doi.org/10.1126/science.1177840
- Cheng H, Sinha A, Wang X, Cruz FW, Edwards RL. The Global Paleomonsoon as seen through speleothem records from Asia and the Americas. *Clim Dyn.* 2012;39(5), 1045–1062. doi.org/10.1007/s00382-012-1363-7.
- Chou WC, Sheu DD, Lee BS, Tseng CM, Chen CTA, Wang SL, et al. Depth distributions of alkalinity, TCO<sub>2</sub> and  $\delta^{13}\text{CTCO}_2$  at SEATS time-series site in the northern South China Sea. *Deep Res Part II Top Stud Oceanogr.* 2007;54(14–15):1469–85. doi.org/10.1016/j.dsr2.2007.05.002.
- Clemens SC, Prell WL. Data report: Oxygen and carbon isotopes from Site 1146, northern South China Sea. In Prell, W.L., Wang, P., Blum, P., Rea, D.K., and Clemens, S.C. (Eds.), *Proc. ODP, Sci Results.* 2003;184: 1–8.
- Clift PD, Wan S, Blusztajn J. Reconstructing chemical weathering, physical erosion and monsoon intensity since 25Ma in the northern South China Sea: A review of competing proxies. *Earth-Sci Rev.* 2014;130: 86–102. doi.org/10.1016/j.earscirev.2014.01.002.
- Conkright ME, Locarnini RA, Garcia HE, O'Brien TD, Boyer TP, Stephens C, Antonov JI. *World Ocean Atlas 2001: Objective Analyses, Data Statistics, and Figures, CD-ROM Documentation.* National Oceanographic Data Center, Silver Spring, MD. 2002; 17 p.
- Dai M, Cao Z, Guo X, Zhai W, Liu Z, Yin Z, et al. Why are some marginal seas sources of atmospheric CO<sub>2</sub>? *Geophys Res Lett.* 2013;40(10):2154–8. doi.org/10.1002/grl.50390.
- Ding X, Bassinot F, Guichard F, Li QY, Fang NQ, Labeyrie L, Xin RC, Adisaputra MK, Hardjawidjaksana K. Distribution and ecology of planktonic foraminifera from the seas around the Indonesian Archipelago. *Mar Micropaleontol.* 2006;58(2): 114–134. doi.org/10.1016/j.marmicro.2005.10.003.
- Emerson SR, Archer D. Calcium carbonate preservation in the ocean. *Philos Trans R Soc London Ser A, Math Phys Sci.* 1990;331(1616):29–40. doi.org/10.1098/rsta.1990.0054.
- Falkowski P, Scholes RJ, Boyle E, Canadell J, Canfield D, Elser J, et al. The global carbon cycle: a test of our knowledge of earth as a system. *Science.* 2000;290: 291–296. doi.org/10.1126/science.290.5490.29.
- Farrell JW, Prell WL. Climatic change and CaCO<sub>3</sub> preservation: an 800,000 year bathymetric reconstruction from the central equatorial Pacific Ocean. *Paleoceanography* 1989;4: 447–466. doi.org/10.1029/PA004i004p00447.

- Fernando AGS, Peleo-Alampay AM, Lucero ES, Wiesner MG. Surface sediment distribution of *Florisphaera profunda* in the South China Sea: an effect of dissolution? *J. Nannoplankton Res.* 2007;29: 102–107.
- Ferreira PAL, Costa KB, Toledo FAL, Figueira RCL. Sedimentation rates and age modeling of late Quaternary marine sediments with unsupported  $^{230}\text{Th}$ . *J. Radioanal Nucl Chem.* 2015;304: 829–836. doi.org/10.1007/s10967-014-3622-z.
- Fuertes MÁ, Flores JA, Sierro FJ. The use of circularly polarized light for biometry, identification and estimation of mass of coccoliths. *Mar Micropaleontol.* 2014;113: 44–55. doi.org/10.1016/j.marmicro.2014.08.007.
- González-Lemos S, Guitián J, Fuertes MÁ, Flores JA, Stoll HM. Technical note: An empirical method for absolute calibration of coccolith thickness. *Biogeosciences.* 2018;15(4):1079–91. doi.org/10.5194/bg-15-1079-2018
- Goodwin P, Lauderdale JM. Carbonate ion concentrations, ocean carbon storage, and atmospheric  $\text{CO}_2$ . *Global Biogeochem Cycles.* 2013;27(3):882–93. doi.org/10.1002/gbc.20078
- Goyet, C, Healy, R, Ryan, J, and Kozyr, A. Global Distribution of Total Inorganic Carbon and Total Alkalinity below the Deepest Winter Mixed Layer Depths. United States: N. p., 2000. doi.org/10.2172/760546.
- Guo X, Zhu X, Wu Q, Huang, D. The Kuroshio nutrient stream and its temporal variation in the East China Sea. *J Geophys Res.* 2012;117(C1): 1–17. doi.org/10.1029/2011JC007292.
- Guo ZT, Berger A, Yin QZ, Qin L. Strong asymmetry of hemispheric climates during MIS-13 inferred from correlating China loess and Antarctica ice records. *Clim Past.* 2008;5(1): 21–31. doi.org/10.5194/cp-5-21-2009.
- Gurumurthy GP, Balakrishna K, Tripti M, Audry S, Riotte J, Braun JJ, Udaya HNS. Geochemical behaviour of dissolved trace elements in a monsoon-dominated tropical river basin, Southwestern India. *Environ Sci Pollut Res Int.* 2014;21(7): 5098–5120. doi.org/10.1007/s11356-013-2462-7
- Hammer, Ø., Harper, D.A.T., Ryan, P.D., PAST: Paleontological Statistics Software Package for Education and Data Analysis. *Palaeontologia Electronica,* 2001;4(1): 1–9. doi.org/10.1016/j.bcp.2008.05.025.
- He J, Zhao M, Wang P, Li L, Li Q. Changes in phytoplankton productivity and community structure in the northern South China Sea during the past 260 ka. *Palaeogeogr Palaeoclimatol Palaeoecol.* 2013;392: 312–323. doi.org/10.1016/j.palaeo.2013.09.010.
- He Z, Wu R. Coupled seasonal variability in the South China Sea. *J Oceanogr.* 2013;69: 57–69. doi.org/10.1007/s10872-012-0157-1.
- Hemleben C, Spindler M, Anderson OR, 1989. *Modern Planktonic Foraminifera.* Springer-Verlag, New York, 1989; p. 8–32.



- Hernández ASR, Trull TW, Nodder SD, Flores JA, Bostock H, Abrantes F, et al. Coccolithophore biodiversity controls carbonate export in the Southern Ocean. *Biogeosciences*. 2020;17(1):245–63. doi.org/10.5194/bg-17-245-2020.
- Hess S, Kuhnt W. Neogene and Quaternary paleoceanographic changes in the southern South China Sea (Site 1143): the Benthic Foraminiferal Record. *Mar Micropaleontol*. 2005;54(1-2): 63–87. doi.org/10.1016/j.marmicro.2004.09.004.
- Hoang LV, Clift PD, Schwab AM, Huuse M, Nguyen DA, Zhen S. Large-scale erosional response of SE Asia to monsoon evolution reconstructed from sedimentary records of the Song Hong-Yinggehai and Qiongdongnan Basins, South China Sea. *Geol Soc Spec Publ*. 2010;342: 219–244. doi.org/10.1144/SP342.13.
- Hönisch B, Ridgwell A, Schmidt DN, Thomas E, Gibbs SJ, Sluijs A, et al. The geological record of ocean acidification. *Science*. 2012;335(6072):1058–1063. doi.org/10.1126/science.1208277.
- Hu D, Böning P, Köhler CM, Hillier S, Pressling N, Wan S, et al. Deep-sea records of the continental weathering and erosion response to East Asian monsoon intensification since 14ka in the South China Sea. *Chem Geol*. 2012;326–327: 1–18. doi.org/10.1016/j.chemgeo.2012.07.024
- Hu Z, Huang BQ, Liu LJ, Wang N., 2021. Spatiotemporal patterns of sediment deposition on the northern slope of the South China Sea in the last 150,000 years. *J Palaeogeogr*. 2021;10(1). doi.org/10.1186/s42501-021-00102-3.
- Huang E, Tian J, Qiao P, Wan S, Xie X, Yang W. Early interglacial carbonate-dilution events in the South China Sea: Implications for strengthened typhoon activities over subtropical East Asia. *Quat Sci Rev* 2015;125: 61–77. doi.org/10.1016/j.quascirev.2015.08.007.
- Iglesias-Rodriguez MD, Halloran PR, Rickaby REM, Hall IR, Colmenero-Hidalgo E, Gittins JR, et al. Phytoplankton calcification in a high-CO<sub>2</sub> world. *Science*. 2008;320(5874):336–40. doi.org/10.1126/science.1154122.
- IPCC, 2019: *Climate Change and Land: an IPCC special report on climate change, desertification, land degradation, sustainable land management, food security, and greenhouse gas fluxes in terrestrial ecosystems* [PR Shukla, J Skea, E Calvo Buendia, V Masson-Delmotte, H-O Pörtner, DC Roberts, et al., (eds.)]. In press.
- Jin H, Jian Z, Wan S. Recent deep water ventilation in the South China Sea and its paleoceanographic implications. *Deep Res Part I Oceanogr Res Pap*. 2018;139: 88–94. doi.org/10.1016/j.dsr.2018.07.016.
- Jin X, Liu C, Poulton AJ, Dai M, Guo X. Coccolithophore responses to environmental variability in the South China Sea: Species composition and calcite content. *Biogeosciences*. 2016;13(16):4843–61. doi.org/10.5194/bg-13-4843-2016.

- Jin X, Liu C, Xu J, Guo X. Coccolithophore Abundance, Degree of Calcification, and Their Contribution to Particulate Inorganic Carbon in the South China Sea. *J Geophys Res Biogeosciences*. 2022;127(4). doi.org/10.1029/2021JG006657.
- Jin X, Liu C, Zhang H. Coccolith morphological and assemblage responses to dissolution in the recent sediments of the East China Sea. *Mar Micropaleontol*. 2019;152(January 2018): 101709. doi.org/10.1016/j.marmicro.2018.09.001.
- Jin X, Liu C. Ecological and taphonomical influences on coccoliths in surface sediments in the shelf of the Yellow and East China Seas. *Cont Shelf Res*. 2017;140(April): 27–36. doi.org/10.1016/j.csr.2017.04.008.
- Jiwarungrueangkul T, Liu Z, Zhao Y. Terrigenous sediment input responding to sea level change and East Asian monsoon evolution since the last deglaciation in the southern South China Sea. *Glob Planet Change*. 2019;174: 127–137. doi.org/10.1016/j.gloplacha.2019.01.011.
- Jonkers L, Kucera M. Global analysis of seasonality in the shell flux of extant planktonic Foraminifera. *Biogeosciences*. 2015;12(7): 2207–2226. doi.org/10.5194/bg-12-2207-2015.
- Kawahata H, Fujita K, Iguchi A, Inoue M, Iwasaki S, Kuroyanagi A, et al. Perspective on the response of marine calcifiers to global warming and ocean acidification—Behavior of corals and foraminifera in a high CO<sub>2</sub> world “hot house”. *Prog Earth Planet Sci*. 2019;6(5): 1–37. doi.org/10.1186/s40645-018-0239-9.
- Kerr J, Rickaby R, Yu J, Elderfield H, Sadekovi AY. The effect of ocean alkalinity and carbon transfer on deep-sea carbonate ion concentration during the past five glacial cycles. *Earth Planet Sci Lett*. 2017;471: 42–53. doi.org/10.1016/j.epsl.2017.04.042.
- Kienast M. Synchronous Tropical South China Sea SST Change and Greenland Warming During Deglaciation. *Science*. 2001; 291(5511): 2132–2134. doi.org/10.1126/science.1057131.
- Kucera M, 2007. Chapter six planktonic foraminifera as tracers of past oceanic environments. In: Hillaire-Marcel, C, De Vernal, A (Eds.), *Proxies in late Cenozoic paleoceanography*. Elsevier, Amsterdam. 2007; 1: 213–262. doi.org/10.1016/S1572-5480(07)01011-1.
- Lagoe BM. Foraminifers from the Nankai Trough and the Japan Trench, Leg 87. Initial reports of the Deep Sea Drilling Project. 87. Government Printing Office, Washington, D.C., U.S. 1986; p. 587–604.
- Le J, Shackleton NJ. Carbonate dissolution fluctuations in the western equatorial Pacific during the late Quaternary. *Paleoceanography*. 1992;7: 21–42. doi.org/10.1029/91PA02854.
- Li B, Zhao Q, Chen MP, Jian Z, Wang P. Carbonate dissolution and deep-water paleoceanography of the South China Sea since the Middle Pleistocene. *Chinese Sci Bull*. 2001;46(22):1908–1911. doi.org/10.1007/BF02901170.
- Li C-F, Li J, Ding W, Franke D, Yao Y, Shi H, et al. Site U1431. In: Li C-F, Lin J, Kulhanek, DK (Eds.), *Expedition 349 Scientists. Proceedings of the International Ocean Discovery*

- Program, 349: South China Sea Tectonics: College Station, TX (International Ocean Discovery Program). 2015a;349. 10.14379/iodp.proc.349.103.2015.
- Li C-F, Li J, Ding W, Franke D, Yao Y, Shi H, et al. Seismic stratigraphy of the central South China Sea basin and implications for neotectonics. *J Geophys Res.* 2015b;120(3): 1377–1399. doi.org/10.1002/2014JB011686.
- Li C-F, Lin J, Kulhanek DK, Williams T, Bao R, Briais A, et al. Site U1432. Proceedings of the International Ocean Discovery Program. In: Li C-F, Lin, J Kulhanek DK (Eds.), Expedition 349 Scientists. Proceedings of the International Ocean Discovery Program, 349: South China Sea Tectonics: College Station, TX (International Ocean Discovery Program). 2015c; 349. doi.org/10.14379/iodp.proc.349.104.2015.
- Li D, Chiang T-L, Kao S-J, Hsin Y-C, Zheng L-W, Yang J-Y-T, et al. Circulation and oxygenation of the glacial South China Sea. *J Asian Earth Sci.* 2017a;138: 387–393. doi.org/10.1016/j.jseas.2017.02.017.
- Li L, Li Q, He J, Wang H, Ruan Y, Li J. Biomarker-derived phytoplankton community for summer monsoon reconstruction in the western South China Sea over the past 450 ka. *Deep-Sea Res II Top Stud Oceanogr.* 2015;122: 118–130. doi.org/10.1016/j.dsr2.2015.11.006.
- Li L, Li QY, Tian J, Wang H, Wang PX. Low latitude hydro-climatic changes during the Plio-Pleistocene: evidence from high resolution alkane records in the South China Sea. *Quat Sci Rev.* 2013;78: 209–224. doi.org/10.1016/j.quascirev.2013.08.007.
- Li N, Feng D, Chen L, Wang H, Chen D. Compositions of foraminifera-rich turbidite sediments from the Shenhu area on the northern slope of the South China Sea: Implication for the presence of deep water bottom currents. *J. Asian Earth Sci.* 2017b;138: 148–160. doi.org/10.1016/j.jseas.2017.02.010.
- Li T, Zhao J, Sun R, Chang F, Sun H. The variation of upper ocean structure and paleoproductivity in the Kuroshio source region during the last 200 kyr. *Mar Micropaleontol.* 2010;75(1–4): 50–61. doi.org/10.1016/j.marmicro.2010.02.005.
- Li Z, Shi X, Chen M Te, Wang H, Liu S, Xu J, et al. Late Quaternary fingerprints of precession and sea level variation over the past 35 kyr as revealed by sea surface temperature and upwelling records from the Indian Ocean near southernmost Sumatra. *Quat Int.* 2016;425: 282–91. doi.org/10.1016/j.quaint.2016.07.013.
- Li Z, Shi X, Chen M-T, Wang H, Liu S, Xu J, et al. Late Quaternary fingerprints of precession and sea level variation over the past 35 kyr as revealed by sea surface temperature and upwelling records from the Indian Ocean near southernmost Sumatra. *Quat Int.* 2016;425: 282–291. doi.org/10.1016/j.quaint.2016.07.013.
- Libes SM. *An Introduction to Marine Biogeochemistry*, 2nd ed. Burlington, MA: Academic Press Noone, K., Sumaila, R.; Diaz R.J. (eds). Valuing the Oceans, Stockholm Environmental Institute. 2009; p.928.

- Lisiecki, LE, Raymo, ME. A Pliocene-Pleistocene stack of 57 globally distributed benthic  $\delta^{18}\text{O}$  records. *Paleoceanography*. 2005;20: PA1003. doi.org/10.1029/2004PA001071.
- Liu C, Wang P, Tian J, Cheng X. Coccolith evidence for Quaternary nutricline variations in the southern South China Sea. *Mar Micropaleontol*. 2008;69: 42–51. doi.org/10.1016/j.marmicro.2007.11.008.
- Liu G, Chai F. Seasonal and interannual variability of primary and export production in the South China Sea: a three-dimensional physical – biogeochemical model study. *ICES J Mar Sci*. 2009;66(2): 420–431. doi.org/10.1093/icesjms/fsn219.
- Liu J, Li T, Xiang R, Chen M, Yan W, Chen Z, Liu F. Influence of the Kuroshio Current intrusion on Holocene environmental transformation in the South China Sea. *The Holocene*. 2013;23(6): 850–859. doi.org/10.1177/0959683612474481.
- Liu J, Steinke S, Vogt C, Mohtadi M, De Pol-Holz R, Hebbeln D. Temporal and spatial patterns of sediment deposition in the northern South China Sea over the last 50,000 years. *Palaeogeogr Palaeoclimatol Palaeoecol*. 2017;465: 212–224. doi.org/10.1016/j.palaeo.2016.10.033.
- Liu J, Xiang R, Chen M, Chen Z, Yan W, Liu F. Influence of the Kuroshio current intrusion on depositional environment in the Northern South China Sea: Evidence from surface sediment records. *Mar Geol*. 2011;285(1–4):59–68. doi.org/10.1016/j.margeo.2011.05.010.
- Liu J, Xiang R, Chen Z, Chen M, Yan W, Zhang L, Chen H. Sources, transport and deposition of surface sediments from the South China Sea. *Deep-Sea Research Part I: Oceanographic Research Papers*. 2013;71: 92–102. doi.org/10.1016/j.dsr.2012.09.006.
- Liu J, Xiang R, Kao S, Fu S, Zhou L. Sedimentary responses to sea-level rise and Kuroshio Current intrusion since the Last Glacial Maximum: Grain size and clay mineral evidence from the northern South China Sea slope. *Palaeogeogr Palaeoclimatol Palaeoecol*. 2016;450: 111–121. doi.org/10.1016/j.palaeo.2016.03.002.
- Liu KK, Chao SY, Shaw PT, Gong GC, Chen CC, Tang TY. Monsoon-forced chlorophyll distribution and primary production in the South China Sea: observations and a numerical study. *Deep-Sea Res*. 2002;49: 1387–1412. doi.org/10.1016/S0967-0637(02)00035-3.
- Liu Q, Kaneko A, Jilan S. Recent Progress in Studies of the South China Sea Circulation. *J Oceanogr*. 2008;64: 753–762. doi.org/10.1007/s10872-008-0063-8.
- Liu S, Feng X, Feng Z, Xiao X, Feng L. Geochemical evidence of methane seepage in the sediments of the Qiongdongnan Basin, South China Sea. *Chem Geol*. 2020;543(March): 119588. doi.org/10.1016/j.chemgeo.2020.119588.
- Liu Z, Colin C, Huang W, Phon Le K, Tong S, Chen Z, Trentesaux A. Climatic and tectonic controls on weathering in south China and Indochina Peninsula: Clay mineralogical and geochemical investigations from the Pearl, Red, and Mekong drainage basins. *Geochem Geophys Geosystems*. 2007;8(5). doi.org/10.1029/2006GC001490.

- Liu Z, Colin C, Li X, Zhao Y, Tuo S, Chen Z, et al. Clay mineral distribution in surface sediments of the northeastern South China Sea and surrounding fluvial drainage basins: Source and transport. *Mar Geol.* 2010;277(1–4): 48–60. doi.org/10.1016/j.margeo.2010.08.010.
- Liu Z, Trentesaux A, Clemens SC, Colin C, Wang P, Huang B, Boulay S. Clay mineral assemblages in the northern South China Sea: implications for East Asian monsoon evolution over the past 2 million years. *Mar Geol.* 2003;201(1-3): 133-146. doi.org/10.1016/S0025-3227(03)00213-5.
- Liu Z, Tuo S, Colin C, Liu JT, Huang CY, Selvaraj K, et al. Detrital fine-grained sediment contribution from Taiwan to the northern South China Sea and its relation to regional ocean circulation. *Mar Geol.* 2008;255(3–4): 149–155. doi.org/10.1016/j.margeo.2008.08.003.
- Liu Z, Zhao Y, Colin C, Siringan FP, Wu Q. Applied Geochemistry Chemical weathering in Luzon, Philippines from clay mineralogy and major-element geochemistry of river sediments. *Appl Geochem.* 2009;24(11): 2195–2205. doi.org/10.1016/j.apgeochem.2009.09.025.
- Liu Z, Zhao Y, Colin C, Statterger K, Martin G, Huh C, et al. Source-to-Sink transport processes of fluvial sediments in the South China Sea. *Earth-Sci Rev.* 2016;153: 238-273. doi.org/10.1016/j.earscirev.2015.08.005.
- Liu Z, Zhao Y, Li JR, Colin C. Late Quaternary clay minerals off Middle Vietnam in the western South China Sea: Implications for source analysis and East Asian monsoon evolution. *Sci China, Series D: Earth Sci.* 2007;50(11): 1674–1684. doi.org/10.1007/s11430-007-0115-8.
- Luo Y, Kienast M, Boudreau BP. Invariance of the carbonate chemistry of the South China Sea from the glacial period to the Holocene and its implications to the Pacific Ocean carbonate system. *Earth Planet Sci Lett.* 2018;492: 112–120. doi.org/10.1016/j.epsl.2018.04.005.
- Lüthi D, Le Floch M, Bereiter B, Blunier T, Barnola JM, Siegenthaler U, et al. High-resolution carbon dioxide concentration record 650,000-800,000 years before present. *Nature.* 2008;453(7193): 379–82. doi.org/10.1038/nature06949.
- Ma X, Tian J, Ma W, Li K, Yu J. Changes of deep Pacific overturning circulation and carbonate chemistry during middle Miocene East Antarctic ice sheet expansion. *Earth Planet Sci Lett.* 2018;484: 253–263. doi.org/10.1016/j.epsl.2017.12.002.
- Malmgren BA. Ranking of dissolution susceptibility of planktonic foraminifera at high latitudes of the South Atlantic Ocean. *Mar Micropaleontol.* 1983;8: 183–191. doi.org/10.1016/0377-8398(83)90023-3.
- Martínez JJ. Late Pleistocene carbonate dissolution patterns in the Tasman Sea. In: Van der Lingen, G J, Swanson, K M, Muir, R J (Eds.), *Evolution of the Tasman Sea*. A.A. Balkema, Rotterdam, Netherlands. 1994; p. 215–228.

- McClymont EL, Sosdian SM, Rosell-Melé A, Rosenthal Y. Pleistocene sea-surface temperature evolution: Early cooling, delayed glacial intensification, and implications for the mid-Pleistocene climate transition. *Earth-Science Rev.* 2013;123: 173–193. doi.org/10.1016/j.earscirev.2013.04.006.
- Miao Q, Thunell RC, Anderson DM. Glacial–Holocene carbonate dissolution and seasurface temperatures in the South China and Sulu Seas. *Paleoceanography.* 1994;9(2): 269–290. doi.org/10.1029/93PA02830.
- Middelburg JJ, van der Weijden CH, Woittiez JRW. Chemical processes affecting the mobility of major, minor and trace elements during weathering of granitic rocks. *Chem Geol.* 1988;68(3–4): 253–273. doi.org/10.1016/0009-2541(88)90025-3.
- Morey AE, Mix AC, Pisias NG. Planktonic foraminiferal assemblages preserved in surface sediments correspond to multiple environment variables. *Quat Sci Rev.* 2005;24: 925–950. doi.org/10.1016/j.quascirev.2003.09.011.
- Murtugudde R, Beauchamp J, McClain CR, Lewis M, Busalacchi, A. Effects of penetrative radiation on the upper tropical ocean circulation, *J. Clim.* 2002;15(5): 470-486. doi.org/10.1175/1520-0442(2002)015<0470:EOPROT>2.0.CO;2.
- Nagai RH, Gerotto A. Data report : middle to late Pleistocene planktonic foraminifer abundances from IODP Holes U1431D, U1432C, and U1433A. 2018;349:1432–4. doi.org/10.14379/iodp.proc.349.204.2018.
- Nesbit HW, Wilson RE. Recent chemical weathering of basalts. *Am J Sci.* 1992;292(10): 740-777. doi.org/10.2475/ajs.292.10.740.
- Nesbitt HW, Markovics G. Weathering of granodioritic crust, long-term storage of elements in weathering profiles, and petrogenesis of siliciclastic sediments. *Geochim Cosmochim Acta.* 1997;61(8): 1653–1670. doi.org/10.1016/s0016-7037(97)00031-8.
- Oppo DW, Sun Y. Amplitude and timing of sea-surface temperature change in the northern South China Sea: Dynamic link to the East Asian monsoon. *Geology.* 2005;33(10): 785–788. doi.org/10.1130/G21867.1.
- Parker FL. Planktonic foraminiferal species in Pacific sediments. *Micropaleontology.* 1962;8(2): 219–254. doi.org/10.2307/1484745.
- Pflaumann U, Jian Z. Modern distribution patterns of planktonic foraminifera in the South China Sea and Western Pacific: a new transfer technique to estimate regional sea-surface temperatures. *Mar Geol.* 1999;156(1-4): 41–83. doi.org/10.1016/S0025-3227(98)00173-X.
- Pierrot D, Lewis E, Wallace DWR. MS Excel Program Developed for CO<sub>2</sub> System Calculations - version 2.1 (2012). ORNL/CDIAC-105a. Carbon Dioxide Information Analysis Center, Oak Ridge National Laboratory, U.S. Department of Energy, Oak Ridge, Tennessee. 2006. doi: 10.3334/CDIAC/otg.CO2SYS\_XLS\_CDIAC105a.

- Pinxian W, Qiubao M, Yunhua B, Wenke F. Planktonic Foraminifera in the Continental Slope of the Northern South China Sea during the Last 130,000 Years and Their Paleo-Oceanographic Implications. *Acta Geol Sin.* 1986;60(3): 1–11. doi.org/10.1111/j.1755-6724.1986.mp60003001.x.
- Pinxian W, Qiubao M, Yunhua B, Wenke F. Planktonic Foraminifera in the Continental Slope of the Northern South China Sea during the Last 130,000 Years and Their Paleo-Oceanographic Implications. *Acta Geol Sin-Engl.* 1986;60(3): 1–11. doi.org/10.1111/j.1755-6724.1986.mp60003001.x.
- Qiu B. Kuroshio and Oyashio currents. In: *Encyclopedia of Ocean Sciences*, edited by: Steele, J. H., Academic Press, 329 New York. 2001;358–369.
- Qu T, Girton JB, Whitehead JA. Deepwater overflow through Luzon Strait. *J Geophys Res.* 2006;111(C1): C01002. doi.wiley.com/10.1029/2005JC003139.
- Qu T, Song YT, Yamagata T. An introduction to the South China Sea throughflow: Its dynamics, variability, and application for climate. *Dyn Atmos Ocean.* 2009;47(1–3): 3–14. doi.org/10.1016/j.dynatmoce.2008.05.001.
- Rae JWB, Zhang YG, Liu X, Foster GL, Stoll HM, Whiteford RDM. Atmospheric CO<sub>2</sub> over the past 66 million years from marine archives. *Annu Rev Earth Planet Sci.* 2021;49: 609–41. doi.org/10.1146/annurev-earth-082420-063026.
- Regenberg M, Regenberg A, Garbe-Schonberg D, Lea DW. Global dissolution effects on planktonic foraminiferal Mg/calc ratios controlled by the calcite-saturation state of bottom waters. *Paleoceanography.* 2014;29: 127–142. doi.org/10.1002/2013PA002492.
- Resplandy L, Séférian R, Bopp L. Natural variability of CO<sub>2</sub> and O<sub>2</sub> fluxes: What can we learn from centuries-long climate models simulations? *J Geophys Res: Ocean.* 2015;120(1): 3909–3925. doi.org/10.1002/2014JC010463.
- Rickaby REM, Bard E, Sonzogni C, Rostek F, Beaufort L, Barker S, et al. Coccolith chemistry reveals secular variations in the global ocean carbon cycle? *Earth Planet Sci Lett.* 2007;253(1–2): 83–95. doi.org/10.1016/j.epsl.2006.10.016.
- Ridgwell A, Zeebe RE. The role of the global carbonate cycle in the regulation and evolution of the Earth system. *Earth Planet Sci Lett.* 2005;234(3–4):299–315. doi.org/10.1016/j.epsl.2005.03.006.
- Rosén P, Vogel H, Cunningham L, Reuss N, Conley DJ, Persson P. Fourier transform infrared spectroscopy, a new method for rapid determination of total organic and inorganic carbon and biogenic silica concentration in lake sediments. *J Paleolimnol.* 2010;43: 247–259. doi.org/10.1007/s10933-009-9329-4.
- Rost B, Riebesell U. Coccolithophores and the biological pump: responses to environmental changes. In: *Coccolithophores: from molecular processes to global impact* / Hans RT, Jeremy RY (Eds.). Berlin:Springer. 2004;99–125.

- Ruiz-Hernandez SE, Grau-Crespo R, Ruiz-Salvador AR, De Leeuw NH. Thermochemistry of strontium incorporation in aragonite from atomistic simulations. *Geochim Cosmochim Acta*. 2010;74(4): 1320–1328. doi.org/10.1016/j.gca.2009.10.049.
- Saavedra-Pellitero M, Baumann K-H, Gallagher SJ, Sagawa T, Tada R. Paleooceanographic evolution of the Japan Sea over the last 460 kyr – a coccolithophore perspective. *Mar Micropaleontol*. 2019;152: 101720. doi.org/10.1016/j.marmicro.2019.01.001.
- Salmon KH, Anand P, Sexton PF, Conte M. Upper Ocean mixing controls the seasonality of planktonic foraminifer fluxes and associated strength of the carbonate pump in the oligotrophic North Atlantic. *Biogeosciences*. 2015;12: 223–235. doi.org/10.5194/bg-12-223-2015.
- Sarmiento JL, Gruber N. *Ocean Biogeochemical dynamics*. Princeton, NJ, Woodstock: Princeton University Press. 2006; 528 p.
- Schiebel, R, 2002. Planktic foraminiferal sedimentation and the marine calcite budget. *Glob Biogeochem Cycles*. 2002;16(4): 13–21. doi:10.1029/2001GB001459.
- Schlitzer R. *Ocean data View*. 2019. Available at:<http://odv.awi.de>.
- Sexton PF, Barker S. Onset of ‘Pacific-style’ deep-sea sedimentary carbonate cycles at the mid-Pleistocene transition. *Earth Planet Sci Lett*. 2012;321-322: 81–94. doi.org/10.1016/j.epsl.2011.12.043.
- Shi X, Wu Y, Zou J, Liu Y, Ge S, Zhao M, et al. Multiproxy reconstruction for Kuroshio responses to northern hemispheric oceanic climate and the Asian Monsoon since Marine Isotope Stage 5.1 (~ 88ka). *Clim Past*. 2014;10(5): 1735–1750. doi.org/10.5194/cp-10-1735-2014.
- Shiau L-J, Yu P-S, Wei K-Y, Yamamoto M, Lee T-Q, Yu E-F, et al. Sea surface temperature, productivity, and terrestrial flux variations of the southeastern South China Sea over the past 800,000 years (IMAGES MD972142). *Terr Atmos Ocean Sci*. 2008;19: 363–376. doi.org/10.3319/TAO.2008.19.4.363(IMAGES).
- Su X, Liu C, Beaufort L, Barbarin N, Jian Z. Differences in late Quaternary primary productivity between the western tropical Pacific and the South China Sea: evidence from coccoliths. *Deep-Sea Res. Part II*. 2015;122: 131–141. doi.org/10.1016/j.dsr2.2015.07.008.
- Su X, Liu C, Beaufort L. Late Quaternary coccolith weight variations in the northern South China Sea and their environmental controls. *Mar Micropaleontol*. 2020;154: 101798. doi.org/10.1016/j.marmicro.2019.101798.
- Su X, Liu, C, Beaufort, L, Tian, J, Huang, E. Late Quaternary coccolith records in the South China Sea and East Asian monsoon dynamics. *Glob Planet Chang*. 2013;111: 88–96.
- Suess E. FS Sonne Fahrtbericht / Cruise Report SO177, SiGer 2004, Sino-German Cooperative Project, South China Sea Continental Margin: Geological Methane Budget and Environmental Effects of Methane Emissions and Gashydrates. In: IFM-GEOMAR



Report, 4. 2005;154 p.

- Sulpis O, Boudreau BP, Mucci A, Jenkins C, Trossman DS, Arbic BK, et al. Current CaCO<sub>3</sub> dissolution at the seafloor caused by anthropogenic CO<sub>2</sub>. *Proc Natl Acad Sci U S A*. 2018;115(46):11700–5. doi.org/10.1073/pnas.1804250115.
- Sun H, Li T, Chang F, Wan S, Xiong Z, An B, Sun R. Deep-sea carbonate preservation in the western Philippine Sea over the past 1Ma. *Quat Int*. 2017;45: 101–115. doi.org/10.1016/j.quaint.2017.08.041.
- Takahashi T, Sutherland SC, Sweeney C, Poisson A, Metzl N, Tilbrook B, et al. Global sea-air CO<sub>2</sub> flux based on climatological surface ocean pCO<sub>2</sub>, and seasonal biological and temperature effects. *Deep Res Part II Top Stud Oceanogr*. 2002;49(9–10):1601–22. doi.org/10.1016/S0967-0645(02)00003-6.
- Teng FZ. Magnesium isotope geochemistry. *Rev Mineral Geochem*. 2017;82: 219–288. doi.org/10.2138/rmg.2017.82.7.
- Thunell RC, Qingmin, M, Calvert SM, Pedersen TF. Glacial-Holocene biogenic sedimentation patterns in the South China Sea: Productivity variations and surface water pCO<sub>2</sub>. *Paleoceanography*. 1992;7(2): 143–162. doi.org/10.1029/92PA00278.
- Tian J, Huang E, Pak DK. East Asian winter monsoon variability over the last glacial cycle: Insights from a latitudinal sea-surface temperature gradient across the South China Sea. *Palaeogeogr Palaeoclimatol Palaeoecol*. 2010;292(1–2): 319–24. doi.org/10.1016/j.palaeo.2010.04.005.
- Tian J, Wang PX, Chen RH, Cheng XR. Quaternary upper ocean thermal gradient variations in the South China Sea: Implications for East Asian Monsoon climate. *Paleoceanography*. 2005;20(4): 1–8. doi.org/10.1029/2004PA001115.
- Tian J, Yang Q, Liang X, Xie L, Hu D, Wang F, Qu T. Observation of Luzon Strait transport. *Geophys Res Lett*. 2006;33 (19): L19607. doi.org/10.1029/2006gl026272.
- UNITED STATES ENVIRONMENTAL PROTECTION AGENCY – USEPA, 1996. Microwave assisted acid digestion of siliceous and organically based matrices. Method 3052. Revision.
- UNITED STATES ENVIRONMENTAL PROTECTION AGENCY – USEPA, 2007. Microwave assisted acid digestion of Sediments, Sludges, Soils and Oils – Method 3050 – SW – 846.
- USGCRP: Climate Science Special Report: Fourth National Climate Assessment, Volume I [Wuebbles DJ, DW Fahey, KA Hibbard, DJ Dokken, BC Stewart, TK Maycock (eds.)]. U.S. Global Change Research Program, Washington, DC, USA. 2017; 470 p.
- Villiers SDe. Seawater strontium and Sr = Ca variability in the Atlantic and Pacific oceans. *Earth Planet Sci Lett*. 1999;171(4): 623–634. doi.org/10.1016/S0012-821X(99)00174-0.

- Wan S, Jian Z, Dang H. Deep Hydrography of the South China Sea and Deep Water Circulation in the Pacific Since the Last Glacial Maximum. *Geochemistry Geophys Geosystems*. 2018;19(5): 1447–63. doi.org/10.1029/2017GC007377.
- Wan S, Jian Z, Gong X, Dang H, Wu J, Qiao P. Deep water [CO<sub>2</sub>] and circulation in the south China sea over the last glacial cycle. *Quat Sci Rev*. 2020;243: 106499. doi.org/10.1016/j.quascirev.2020.106499.
- Wan S, Jian Z. Deep water exchanges between the South China Sea and the Pacific since the last glacial period. *Paleoceanography*. 2014;29(12): 1162–78. doi.org/10.1002/2013PA002578.
- Wang L, Wang P. Late Quaternary paleoceanography of the South China Sea: glacial-interglacial contrasts in an enclosed basin. *Paleoceanography*. 1990;5(1): 77–90. doi.org/10.1029/PA005i001p00077.
- Wang N, Huang B-Q, Li H. Deep-water carbonate dissolution in the northern South China Sea during Marine Isotope Stage 3. *J Palaeogeogr*. 2016;5(1): 100–7. doi.org/10.1016/j.jop.2015.11.004.
- Wang P, 1994. Paleoceanography in China: Progress and Problems. In: Di, Z, Yuan-Bo, L, Cheng-Kui, Z (Eds.), *Oceanology of China Seas*. Springer, Dordrecht. 1994;p. 419–429. doi.org/10.1007/978-94-011-0862-1\_40.
- Wang P, Li Q, Tian J. Pleistocene paleoceanography of the South China Sea: Progress over the past 20years. *Mar Geol*. 2014;352: 381–396. doi.org/10.1016/j.margeo.2014.03.003.
- Wang P, Li Q. *The South China Sea: Paleoceanography and Sedimentology*. Springer, Berlin, Heidelberg, New York. 2009;p. 506.
- Wang P, Min Q, Bian Y, Feng W. Planktonic foraminifera in the continental slope of the northern South China Sea during the last 130,000 years and their paleo-oceanographic implications. *Acta Geol. Sin*. 1968;60(3): 1–11. doi.org/10.1111/j.1755-6724.1986.mp60003001.x.
- Wang P, Tian J, Cheng X, Liu C, Xu J. Carbon reservoir changes preceded major ice-sheet expansion at the mid-Brunhes event. *Geology*. 2003;31(3): 239–242. doi.org/10.1130/0091-7613(2003)031<0239:CRCPMI>2.0.CO;2.
- Wang P, Wang B, Cheng H, Fasullo J, Guo ZT, Kiefer T, Liu ZY. The global monsoon across timescales: coherent variability of regional monsoons. *Clim Past*. 2014;10(6): 2007–2052. doi.org/10.5194/cp-10-2007-2014.
- Wang P, Wang L, Bian Y, Jian Z. Late Quaternary paleoceanography of the South China Sea: surface circulation and carbonate cycles. *Mar Geol*. 1995;127(1–4): 145–65. doi.org/10.1016/0025-3227(95)00008-M.
- Wang P. Response of Western Pacific marginal seas to glacial cycles: paleoceanographic and sedimentological features. *Mar Geol*. 1999;156: 5–39. doi.org/10.1016/S0025-

3227(98)00172-8.

- Weedon GP, Hall I. Data report: inorganic geochemistry of Miocene to recent samples from Chatham Rise, southwest Pacific, Site 1123. In Richter, C. (Ed.), Proc. ODP, Sci. Results. 2002;181: 1–10.
- Wei G, Li XH, Liu Y, Shao L, Liang X. Geochemical record of chemical weathering and monsoon climate change since the early Miocene in the South China Sea. *Paleoceanography*. 2006;21(4): 1–11. doi.org/10.1029/2006PA001300.
- Wei G, Liu Y, Li X, Shao L, Fang D. Major and trace element variations of the sediments at ODP Site 1144, South China Sea, during the last 230 ka and their paleoclimate implications. *Palaeogeogr Palaeoclimatol Palaeocol*. 2004;212(3-4): 331–342. doi.org/10.1016/j.palaeo.2004.06.011.
- Wei G, Liu Y, Li X, Shao L, Liang X. Climatic impact on Al, K, Sc and Ti in marine sediments: Evidence from ODP site 1144, South China Sea. *Geochemical Journal*. 2003;37(5): 593–602. doi.org/10.2343/geochemj.37.593.
- Wei K-Y, Lee M-Y, Duan W, Chen C, Wang C-H. Palaeoceanographic change in the northeastern South China Sea during the last 15000 years. *J Quat Sci*. 1998;13: 55–64. doi.org/10.1002/(SICI)1099-1417(199801/02)13:1<55::AID-JQS332>3.0.CO;2-S.
- Wu D, Sun T, Xie R, Pan M, Chen X, Ye Y, Liu L, Wu N. Characteristics of Authigenic Minerals around the Sulfate-methane transition Zone in the Methane-Rich Sediments of the Northern South China Sea: Inorganic Geochemical evidence. *Int J Environ Res Public Health*. 2019;16: 2299. doi.org/10.3390/ijerph16132299.
- Xu F, Hu B, Zhao J, Liu X, Xu K, Xiong Z, Wang F, Ding X, Li Q, Guo J. Provenance and weathering of sediments in the deep basin of the northern South China Sea during the last 38 kyr, *Mar Geol*. 2021;440: 106602. doi.org/10.1016/j.margeo.2021.106602.
- Xu J, Wang P, Huang B, Li Q, Jian Z. Response of planktonic foraminifera to glacial cycles: Mid-Pleistocene change in the southern South China Sea. *Mar Micropaleontol*. 2005;54: 89–105. doi.org/10.1016/j.marmicro.2004.09.005.
- Xue HJ, Chai F, Pettigrew N, Xu DY, Shi M, Xu JP. Kuroshio intrusion and the circulation in the South China Sea. *J Geophys Res Oceans*. 2004;109(C2): C02017. doi.org/10.1029/2002JC001724.
- Young JR, Ziveri P. Calculation of coccolith volume and its use in calibration of carbonate flux estimates. *Deep Res Part II Top Stud Oceanogr*. 2000;47(9–11): 1679–700. doi.org/10.1016/S0967-0645(00)00003-5.
- Yu J, Anderson RF, Rohling EJ. Deep ocean carbonate chemistry and glacial-interglacial atmospheric  $\text{CO}_2$  changes. *Oceanography*. 2014;27(1): 16–25. doi.org/10.5670/oceanog.2014.04.

- Yu P, Chen M. Millennial-to-orbital scale changes in the planktic foraminiferal assemblages and sea surface temperature in the South China Sea during the past 135 kya. 2013;15: 9190.
- Zeebe RE, Westbroek P. A simple model for the CaCO<sub>3</sub> saturation state of the ocean: The “Strangelove,” the “Neritan,” and the “Cretan” Ocean. *Geochem Geophys Geosystems*. 2003;4(12). doi:10.1029/2003GC000538.
- Zeebe RE. History of seawater carbonate chemistry, atmospheric CO<sub>2</sub>, and ocean acidification. *Annu Rev Earth Planet Sci*. 2012;40: 141–165. doi.org/10.1146/annurev-earth-042711-105521.
- Zhang H, Liu C, Jin X, Shi J, Zhao S, Jian Z. Dynamic of primary productivity in the northern South China Sea over the past 24,000 years. *Geochem Geophys Geosystems*. 2016;17: 4878–4891. doi.org/10.1002/2016GC006602.
- Zhang L, Wang R, Chen M, Liu J, Zeng L, Xiang R, Zhang Q. Biogenic silica in surface sediments of the South China Sea: Controlling factors and paleoenvironmental implication. *Deep-Sea Res II Top Stud Oceanogr*. 2015;122: 142–152. doi.org/10.1016/j.dsr2.2015.11.008.
- Zhang P, Molnar P, Downs, WR. Increased sedimentation rates and grain sizes 2–4 Myr ago due to the influence of climate change on erosion rates. *Nature*. 2001;410(6831): 891–897. doi.org/10.1038/35073504.
- Zhang Y, Yi L, Ogg JG. Pliocene-Pleistocene magneto-cyclostratigraphy of IODP Site U1499 and implications for climate-driven sedimentation in the northern South China Sea. *Palaeogeogr Palaeoclimatol Palaeoecol*. 2019;527: 118–132. doi.org/10.1016/j.palaeo.2019.04.029.
- Zhao S, Liu Z, Quan C, Xingxing W, Jiangnan S, Haiyan J, et al., 2017. Spatiotemporal variations of deep-sea sediment components and their fluxes since the last glaciation in the northern South China Sea. *Sci China Earth Sci*. 2017;60(7): 1368–1381. doi.org/10.1007/s11430-016-9058-6.
- Zhao Y, Liu Z, Colin C, Xie X, Wu Q. Turbidite deposition in the southern South China Sea during the last glacial: evidence from grain-size and major elements records. *Chin Sci Bull*. 2011;56: 3558–3565. doi: 10.1007/s11434-011-4685-7.
- Zhou C, Zhao W, Tian J, Zhao X, Zhu Y, Yang Q. Deep Western Boundary Current in the South China Sea. *Sci Rep*. 2017;7: 9303. doi.org/10.1038/s41598-017-09436-2.
- Zhou X, Lyu X, Liu C, Liu Z, Li Q, Jin X, Zhang H, Dadd K. Depositional mechanisms for upper Miocene sediments in the South China Sea central basin: Evidence from calcareous nannofossils. *Mar Micropaleontol*. 2019;151: 101768. doi.org/10.1016/j.marmicro.2019.101768.

## APPENDICES

Appendix A - Supplementary Material 1.1. Activities of  $^{230}\text{Th}_{\text{xs}}$ , values of  $\ln ^{230}\text{Th}_{\text{xs}}$  calculated with Equation 1 and the sedimentation rate of Hole U1431D.

Depth (cm)	$^{230}\text{Th}_{\text{xs}}$ (mBq g <sup>-1</sup> )		$\ln ^{230}\text{Th}_{\text{xs}}$		Sedimentation rate (cm ka <sup>-1</sup> )	
	Value	Error	Value	Error	Value	Error
149	160,73	9,62	5,08	0,30	2,86	0,21
248	97,99	6,01	4,58	0,28		
470	89,91	5,43	4,50	0,27		
620	65,58	4,23	4,18	0,27		
770	17,36	1,31	2,85	0,22		
869	20,35	1,72	3,01	0,25		
920	19,40	1,59	2,97	0,24		
1020	7,19	0,58	1,97	0,16		
1368	54,44	3,82	4,00	0,28	11,13	0,82
1428	40,35	2,86	3,70	0,26		
1582	49,36	3,38	3,90	0,27		
1616	27,09	2,11	3,30	0,26		
1736	49,33	3,51	3,90	0,28		
1816	38,03	2,79	3,64	0,27		
1913	46,33	3,26	3,84	0,27		
2120	19,56	1,53	2,97	0,23		

Appendix B - Supplementary Material 1.2. Chronology derived from the excess  $^{230}\text{Th}_{\text{xs}}$  method and magnetostratigraphic data from Hole U1431D. Deviations between the results.

Depth	Age (kyr BP)		
	$^{230}\text{Th}_{\text{xs}}$	BioMagnetostigraphic data	Deviation
0.00	0	0.00	0%
1.49	52.12	83.69	6%
2.48	86.74	134.28	9%
4.70	164.39	234.04	13%
6.20	216.86	291.47	14%
7.70	269.32	341.47	13%
8.69	303.95	370.68	12%
9.20	321.79	384.61	11%
10.20	356.77	409.82	10%
13.68	457.70	478.00	4%
14.28	463.09	487.02	4%
15.82	476.93	506.99	5%
16.16	479.99	510.82	6%
17.36	490.77	522.85	6%
18.16	497.96	529.67	6%
19.13	506.68	536.80	5%
21.20	525.28	548.44	4%

Appendix C - Supplementary Material 2.1. Certified value, confidence interval and values obtained from SS-2 Certified Reference Material.

Element	Certified Value (ppm)	Confidence interval (95%)	Obtained Value (mg/kg)
[Al] mg/kg	44.85	37.791 - 51.915	36726.70
[Ba] mg/kg	650	594-706	417.58
[Ca] mg/kg	118.74	106.80-130.68	83714.03
[Cd] mg/kg	(2)	-	1.74
[Cr] mg/kg	58	51-65	37.31
[Cu] mg/kg	198	189-207	151.49
[Fe] mg/kg	29.07	27.26-30.88	23165.47
[K] mg/kg	18.12	16.35-19.89	13420.47
[Mg] mg/kg	14.23	12.99-15.45	7247.47
[Mn] mg/kg	577	545-609	490.10
[Ni] mg/kg	59	55-63	36.73
[Sc] mg/kg	-	-	5.96
[Sr] mg/kg	382	351-413	267.77
[Ti] mg/kg	2893	2664-3122	2036.88
[V] mg/kg	59	54-64	42.22
[Zn] mg/kg	509	479-539	317.15

Appendix D - Supplementary Material 2.2. Activities of  $^{230}\text{Th}_{\text{xs}}$ , values of  $\ln ^{230}\text{Th}_{\text{xs}}$  calculated with Equation 1 and the sedimentation rate of Hole U1432C.

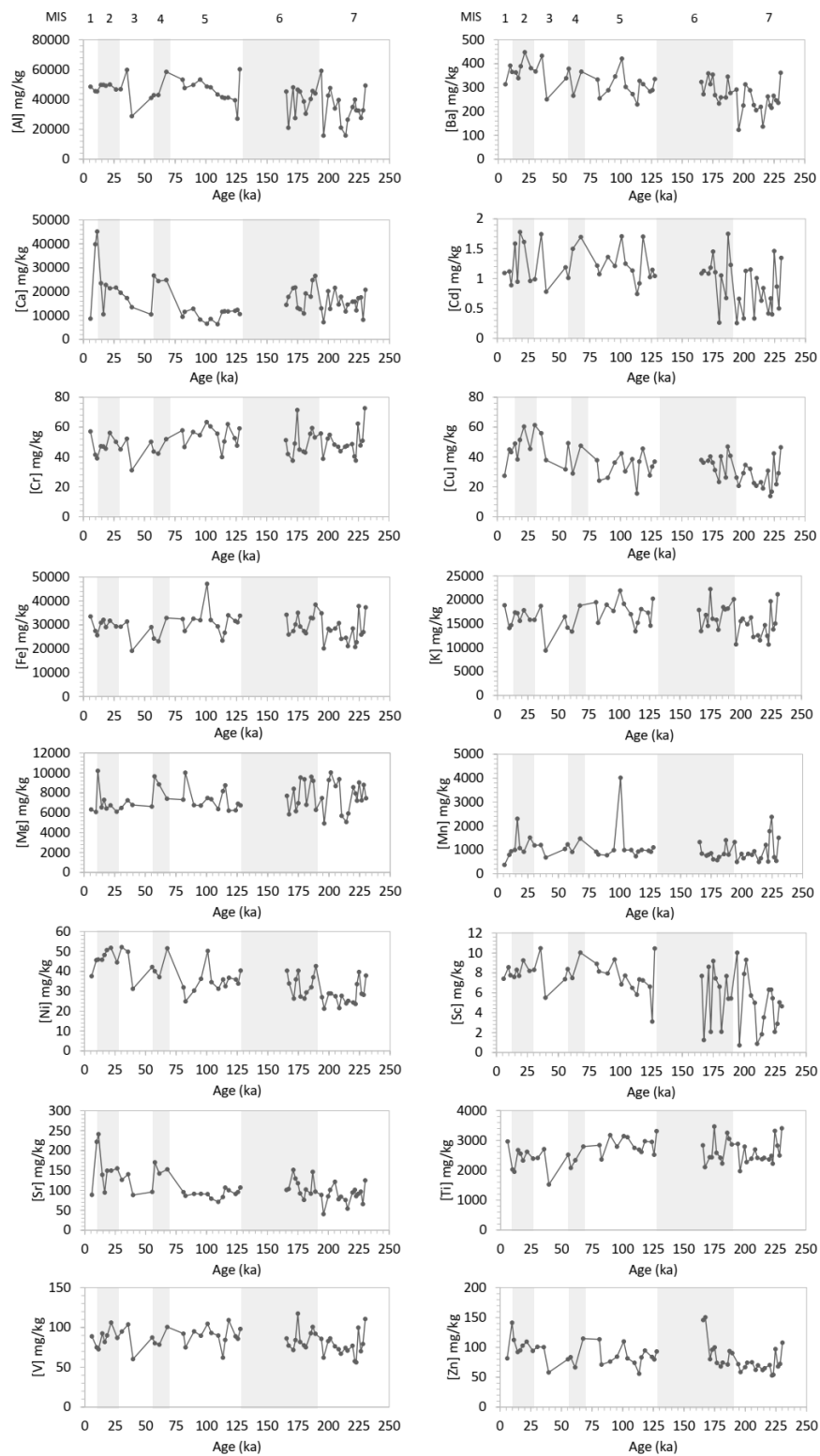
Depth (cm)	$^{230}\text{Th}_{\text{xs}}$ (mBq g <sup>-1</sup> )		$\ln (^{230}\text{Th}_{\text{xs}})$			Sedimentation rate (cm ka <sup>-1</sup> )	
	Value	Error	Value	Error	Adjustment	Value	Error
61	76.47	2.51	4.34	0.14		10.52	0.34
149	143.81	4.70	4.97	0.16	4.97		
226	195.14	6.37	5.27	0.17	5.27		
298	12.85	0.42	2.55	0.08			
360	139.14	4.57	4.94	0.16	4.94		
431	11.29	0.38	2.42	0.08			
492	35.20	1.16	3.56	0.12			
580	97.34	3.19	4.58	0.15	4.58		
642	197.61	6.44	5.29	0.17			
711	198.33	6.43	5.29	0.17			
771	250.83	8.42	5.52	0.19			
850	152.70	5.00	5.03	0.16			
942	44.57	1.48	3.80	0.13			
1001	20.84	0.59	3.04	0.09			
1091	70.93	2.32	4.26	0.14	4.26		
1151	83.19	2.66	4.42	0.14	4.42		
1241	70.08	2.29	4.25	0.14	4.25		
1301	81.34	2.67	4.40	0.14	4.40		
1342	76.89	2.47	4.34	0.14	4.34		
1732	34.41	1.12	3.54	0.12	3.54		

---

1801					
1840	267.72	8.61	5.59	0.18	
1892	116.30	3.77	4.76	0.15	
1951					
2042	29.19	0.95	3.37	0.11	3.37
2101	188.69	6.15	5.24	0.17	
2191	44.25	1.47	3.79	0.13	
2251	11.74	0.39	2.46	0.08	
2343					

---

## Appendix E - Supplementary Material 2.3. Major and trace elements distribution along Hole U1432C.





## Appendix F - Supplementary Material 3.1. Measurement of coccoliths per sample.

Amount of Calgon solution	Number of coccoliths measured
0 ml	87
0.4 ml	139
0.8 ml	175
2 ml	140
4 ml	125
6 ml	30